Exploration of High Voltage NASICON Cathodes for Sodium-ion Batteries

A Thesis Submitted for the Degree of

Doctor of Philosophy

By

Subham Ghosh

New Chemistry Unit

Jawaharlal Nehru Centre for Advanced Scientific Research

(A Deemed University)

Bangalore-560064 (INDIA)

September 2021

Dedicated to my family

Declaration

I hereby declare that the thesis entitled "***Exploration of High Voltage NASICON Cathodes for Sodium-ion Batteries***" is the result of investigations carried out by me at the New Chemistry Unit, Jawaharlal Nehru Centre for Advanced Scientific Research, Bengaluru, India under the supervision of **Dr. Premkumar Senguttuvan** and that it has not been submitted elsewhere for the award of any degree or diploma.

In keeping with the general practice in reporting scientific investigations, due acknowledgement has been made wherever the work described is based on findings of other investigators. Any omission that might have occurred by oversight or error of judgement is regretted.

Subham Ghosh

Date: 13.09.2021
Bengaluru, India

Subham Ghosh

CERTIFICATE

I hereby certify that the work described in this thesis titled "***Exploration of High Voltage NASICON Cathodes for Sodium-ion Batteries***" has been carried out by Subham Ghosh at New Chemistry Unit, Jawaharlal Nehru Centre for Advanced Scientific Research, Bangalore, India under my supervision and that it has not been submitted elsewhere for the award of any degree or diploma.

S. Premkumar

Bangalore, India
September 13, 2021

Dr. Premkumar Senguttuvan
(Research Supervisor)

Acknowledgements

The successful submission of my PhD thesis includes contribution from various people through their constant help, support and enthusiasm which motivated me to move ahead. This thesis would be incomplete without expressing my gratitude towards them.

Firstly I would like to express my sincere thanks and gratitude to my teacher, mentor, and supervisor, ***Dr. Premkumar Senguttvan*** for his guidance in forming the base of my research career. His persistent support, advice, criticism and wisdom inspired me to do better work each day as well as helped me to grow as an individual. Thank you, sir, for being so kind and for everything that helped me to improve myself each day.

I would like to express my sincere thanks to **Prof. C. N. R. Rao, FRS, the Chairman, New Chemistry Unit, Jawaharlal Nehru Centre for Advanced Scientific Research** for being the constant source of inspiration, support and encouragement throughout my Ph.D life in JNC.

I would like to thank all my course instructors Prof. Tapas K. Maji, Prof. Sebastian C. Peter, Prof. Chandrabhas Narayana, Prof. A. Sundaresan and Dr. Sarit Agasti for their excellent courses.

I thank my collaborators: Prof. G. Rousse, Prof. S. K. Pati, Prof. R. J. Clement, Dr. Nabadyuti Barman, Dr. Senthilkumar, Madhulika Majumder, Eliovardo Gonzalez-Correa, Aryan Zaveri, Alexis Manche, Dr. Penphitcha Amonpattaratkit for their scientific contributions and fruitful discussion.

My sincere thanks to all the technical staff of JNCASR: Mr. Anil, Ms. Selvi, Mr. Vasu, Mr. Shivakumar, Mr. Rahul and Ms. Meenakshi for their help in characterization techniques.

I would like to thank Melissa, Naveen, JNC administration and academic, complab, students residence, library, Dhanvantari and security.

I thank JNCASR for research fellowship and DST, DESY-Germany for various fundings.

I would like to express my gratitude to my Lab Family to whom I will always remain indebted: **Present members**: Dr. Radha, Vinita, Arindam, Biplab, Bhaskar, Prabhat and Arif; **Past members:** Dr. Nabadyuti, Dr. Senthilkumar, Aditi, Amit, Utsav, Nirmal, Rishikesh, Shubham.

I am grateful to my Alma Mater Khamarpara Jatiya Krira and Shakti Sangha, Bansberia High School, Chandernagore College and IIT Bombay.

Most importantly, I am grateful to my parents, family and friends for their unconditional love, support and constant encouragement throughout my life.

Subham Ghosh

Preface

Chapter 1 describes about the present global energy demand and the need for electrochemical energy storage devices for grid application. It also provides historical review on evolution of battery technologies, from Voltaic pile to modern Li-ion batteries, along with their design principles. It enlists the advantages of SIBs over LIBs and briefly present the state-of-art on Na-ion battery cathodes. Since all of the work carried out in this thesis revolves around NASICON-type phosphate cathodes, a detailed description about its crystal chemistry and research development is provided. Finally, it explains the motivation of the thesis with strategy to enhance the charge storage capacity of the NASICON cathodes.

Chapter 2 provides details about the synthesis routes to prepare NASICON cathodes and physicochemical techniques to characterize them. Brief description about Rietveld refinements on powder X-ray diffraction patterns and extended X-ray absorption fine structure spectra are provided. Further, the methods for the preparation of electrodes for galvanostatic, *in-operando* XRD and *ex-situ* X-ray absorption measurements are described. The chapter ends with a brief discussion on theoretical methods used for studying phase stability, Na-ion diffusion and electronic structures of NASICON materials.

Chapter 3 discuss about the structural-electrochemical investigations of the Mn^{2+}-substituted NASICON-$Na_{3+y}V_{2-y}Mn_y(PO_4)_3$ system. It was reported that $Na_3V_2(PO_4)_3$ and $Na_4VMn(PO_4)_3$ endmembers show reversible exchange of two moles of sodium ions *pfu*, which corresponds to storage capacities of 100-120 mA h g^{-1}. The XRD results showed phase segregation at $y = 0.5$, resulting two solid-solution domains with low and high Mn content. When cycled in 3.8-2.75 V *vs.* Na^+/Na^0 region, these NASICON cathodes reversibly exchanged sodium-ions with high structural integrity. Galvanostatic studies revealed high capacity and rate performances for the $Na_{3.75}V_{1.25}Mn_{0.75}(PO_4)_3$ cathode (100 and 89 mA h g^{-1} at 1C and 5C rate, respectively), which was ascribed to its modulated electronic V- and Mn-redox centers and optimum bottleneck sizes, as deduced from DFT calculations and Rietveld refinements. Further, we have attempted to increase the sodium (de)intercalation capacities of NASICON-$Na_{3+y}V_{2-y}Mn_y(PO_4)_3$ cathodes by extending their cycling window to 4.2-2.75 V *vs.* Na^+/Na^0. Unfortunately, Mn-rich cathodes undergo irreversible structural transformation at higher voltages, resulting in rapid capacity decay.

Chapter 4 elucidates the impact of Mg^{2+} substitution into NASCION-$Na_{3+y}V_{2-y}Mg_y(PO_4)_3$ series, which are analogous to the previous chapter. In the previous study, it was shown that Mn-rich NASICON cathodes undergo irreversible structural transformation at high voltage, which involve competing process of sodium ion removal from Na(1) and Na(2) sites and multielectron V- and Mn-redox, and local structural changes. Therefore to better understand about it, we have tailored NASCION-$Na_{3+y}V_{2-y}Mg_y(PO_4)_3$ cathode series, in which vanadium is the sole redox center. Although our XRD studies showed a complete solid-solution formation between the end members, a complex evolution of local structural changes was observed using X-ray absorption and solid-state nuclear magnetic spectroscopy studies. Upon cycling in the window of 3.8-2.75 V *vs.* Na^+/Na^0, the voltage profiles of Mg-substituted cathodes progressively changed from plateau to S-shape along with the increase of average intercalation voltage and polarization between charge and discharge processes. *In-operando* XRD studies revealed that the change of sodium (de)intercalation mechanism from two-phase for $y = 0.5$ to solid-solution $y = 1$. Galvanostatic intermittent titration technique measurements revealed lowest polarization for $y = 0.5$ member, which was ascribed to the reduced volume mismatch between its Na-rich and Na-poor phases. During the higher voltage window cycling (4.2-2.75 V *vs.* Na^+/Na^0), both $y = 0.5$ and 1 cathodes suffered from irreversible structural changes due to removal of sodium ions from Na(1) site and displayed rapid capacity degradation.

Chapter 5 illustrates asymmetric sodium (de)intercalation pathways in NASICON-$Na_3VIn(PO_4)_3$ cathode. Initially, we attempted to partially substitute In^{3+} in the place of V^{3+} to trigger high voltage operation of V^{5+}/V^{4+} redox couple, similar to other iso-valent cationic substituted $Na_3V^{3+}M^{3+(}PO_4)_3$ cathodes. However, the $Na_3VIn(PO_4)_3$ cathode also displayed irreversible structural changes at higher voltage. Interestingly, this degraded structure became rejuvenated upon extending the lower cut-off voltage to 1.2 V *vs.* Na^+/Na^0. The detailed *in-operando* XRD studies showed asymmetric sodium (de)intercalation pathways in NASICON-$Na_3VIn(PO_4)_3$ which involves multi-redox ($V^{5+}/V^{4+}/V^{3+}/V^{2+}$) operation.

Chapter 6 demonstrates a chemical tunning strategy to improve the cycling stability and rate capability of $Na_4VMn(PO_4)_3$ cathode. Previously, it was shown that $Na_4VMn(PO_4)_3$ suffer from rapid capacity decay, presumably due to Jahn-Teller effect of Mn^{3+} during cycling. In this work, we partially substituted Mn^{2+} in the $Na_4VMn(PO_4)_3$ with Mg^{2+} or Al^{3+}. The substituted cathodes, $Na_4VMn_{0.75}Mg_{0.25}(PO_4)_3$ and $Na_{3.75}VMn_{0.75}Al_{0.25}(PO_4)_3$, exhibited smoother voltages profiles, enhanced capacity (89 mA h g^{-1}) and cycling stability (96 % retention after 100 cycles). Their enhanced performances were ascribed to their increased covalent character, sodium ion vacancies and suppressed Jahn-Teller effect.

Chapter 7 provides a brief summary of this thesis along with few strategies to improve the performance of NASICON cathodes in future.

TABLE OF CONTENTS

Declaration	II
Certificate	IV
Acknowledgement	VI
Preface	VII
Chapter 1. Introduction	1
1.1. Background and Motivation	1
1.2. Design consideration of batteries	2
1.3. Status on Na-ion cathodes	4
1.3.1. Layered Transition Metal Oxides	5
1.3.2. Polyanionic cathodes	7
1.3.2.1. Phosphate cathodes	8
1.3.2.2. NASICON	9
1.4. Scope of the thesis	13
References	14
Chapter 2. Experimental Techniques	19
2.1. Synthesis	19
2.2. Material Characterization	20
2.3. Electrochemical characterization	23

2.4. Theoretical Calculations 25

References 25

Chapter 3. High Capacity and High Rate NASICON-$Na_{3.75}V_{1.25}Mn_{0.75}(PO_4)_3$ Cathode for Na-ion Batteries via Modulating Electronic and Crystal Structures 29

3.1. Introduction 31

3.2. Experimental 33

3.3. Results and Discussion 33

3.3.1. Formation of solid solution 33

3.3.2. Electrochemical (de)intercalation properties of $Na_{3+y}V_{2-y}Mn_y(PO_4)_3$ cathodes 44

3.3.3. Ex-situ XRD and XAS studies on $Na_{3+y}V_{2-y}Mn_y(PO_4)_3$ cathodes 46

3.3.4. Theoretical approach 52

3.3.5. Cycling performances of $Na_{3+y}V_{2-y}Mn_y(PO_4)_3$ cathodes 55

3.4. Conclusion 61

References 62

Chapter 4. Elucidating the Impact of Mg Substitution on the Properties of NASICON-$Na_{3+y}V_{2-y}Mg_y(PO_4)_3$ Cathodes 67

4.1. Introduction 69

4.2. Experimental 72

4.3 Results and Discussion 72

4.4. Conclusions 96

References 97

Chapter 5. Multi-redox ($V^{5+}/V^{4+}/V^{3+}/V^{2+}$) Driven Asymmetric Sodium (De)intercalation Reactions in NASICON-$Na_3VIn(PO_4)_3$ Cathode 101

5.1. Introduction 103

5.2. Experimental 105

5.3. Results and Discussion 105

5.4. Conclusions 121

References 121

Chapter 6. Impact of Mg^{2+} and Al^{3+} Substitutions on the Structural and Electrochemical Properties of NASICON-$Na_xVMn_{0.75}M_{0.25}(PO_4)_3$ (M=Mg and Al) Cathodes for Sodium-ion Batteries 125

6.1. Introduction 127

6.2. Experimental 129

6.3. Results and Discussion 130

6.4. Conclusions 146

References 146

Chapter 7. Summary & Outlook 149

References 152

Chapter 1

1. Introduction

1.1.Background and Motivation

The development of clean and sustainable energy technologies based on solar, wind and hydroelectric sources has become vital to address the growing concerns of depleting fossil fuels and climate changes. However, their intermittent nature of energy production requires integrating large-scale energy storage systems in the grid to smoothen the energy production/distribution fluctuations.[1] Among the available energy storage technologies, rechargeable batteries present numerous benefits such as high round trip efficiency, low cost and maintenance.[2]

Since its commercialization in 1991, lithium-ion batteries (LIBs) have received tremendous success in portable electronics and electric vehicle markets.[3] Further, few efforts are made to install LIBs as a large-scale energy storage system in electric grids. However, the fluctuating cost, limited availability, and geopolitical accessibility of lithium and cobalt sources have impeded the extensive implementation of LIBs in electric mobility and grid storage sectors. To address these issues, alternate battery chemistries have been explored based on inexpensive and Earth-abundant raw materials.[4] Along this line, sodium-ion batteries (SIBs) have gained significant traction due to the low cost and widespread availability of sodium raw materials.[5,6] In fact, studies on LIBs and SIBs had begun parallelly in the 1980s, however, the development of the former was accelerated owing to its high energy density. Both technologies share a common working principle (i.e., rocking chair mechanism) which involves reversible shuttling of alkali-ions between two host electrodes through an ion-conducting electrolyte (Figure 1.1). Recent research efforts have produced various Na-ion cathodes, anodes, and electrolytes by importing the design knowledge gained from Li-ion materials. Moreover, inexpensive and lightweight aluminum replaces copper as the negative electrode current collector, which further reduces the cost and increases the energy density of SIBs. It is worth noting that SIBs have lower energy densities than LIBs due to higher mass and lower reduction potential of sodium. Yet, SIBs are in prospect of large-scale grid storage where the energy density is not a critical factor.

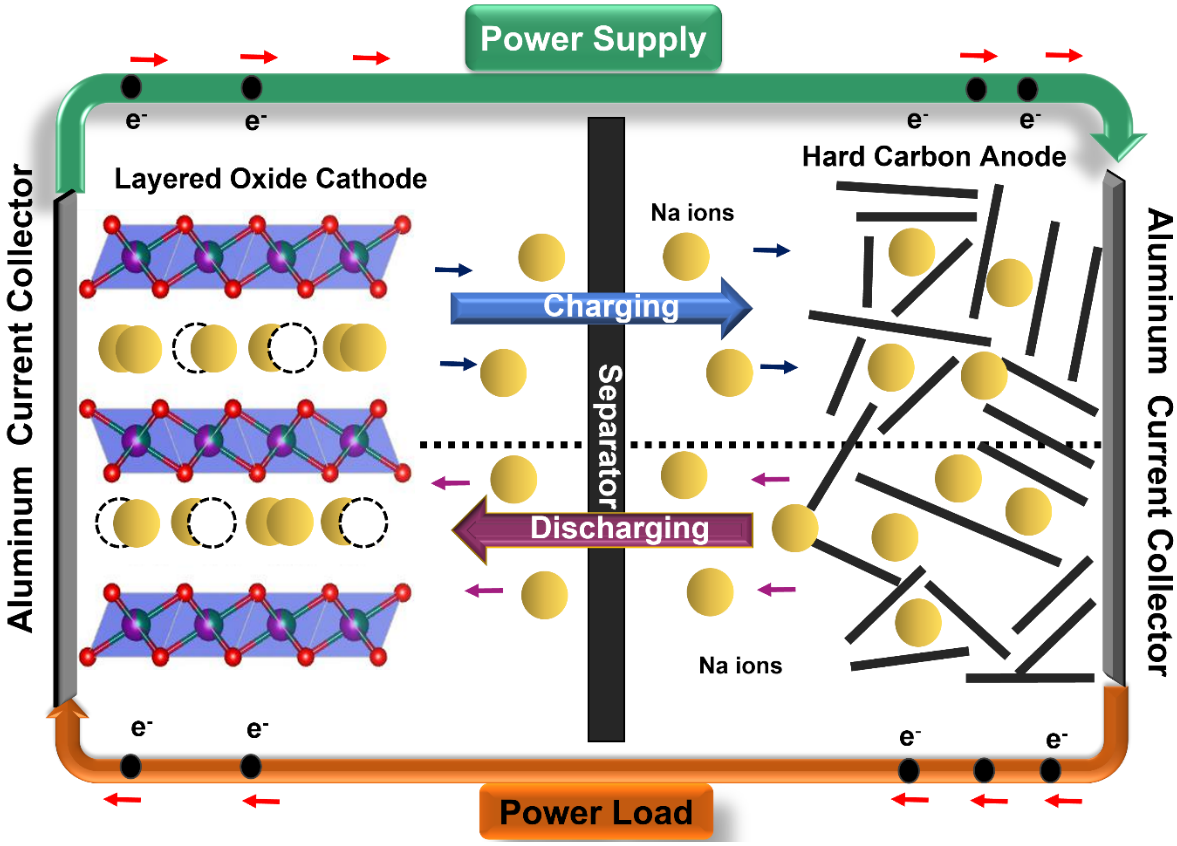

Figure 1.1. Schematic diagram of Na-ion battery.

1.2. Design consideration of batteries

A battery is an electrochemical device that converts chemical energy stored in its active materials into electrical energy through a redox reaction. It consists of one or more electrochemical cells connected in series or parallel to achieve the desired output voltage and capacity. Each electrochemical cell consists of three major components: cathode, anode and electrolyte. The cathode is the electrode which accepts electrons from external circuit and gets reduced during electrochemical reaction. The anode is the electrode that provides electrons to the external circuit and is oxidized during electrochemical reaction. The electrolyte is an ionic conductor that provides a medium for charge transfer in the form of ions between cathode and anode.

Figure 1.2 shows the relative electron energies of cathode, anode and electrolyte in a thermodynamically stable battery.[7,8] μ_A and μ_C refers to the electrochemical potential of anode and cathode, respectively. The potential window of the electrolyte (Eg) is determined by the difference in energies between highest occupied molecular orbital (HOMO) and lowest unoccupied molecular orbital (LUMO). Thermodynamic stability requires the placement of μ_A and μ_C within the electrolyte window E_g and the open-circuit voltage (V_{OC}) of an electrochemical cell is determined by:

$$V_{OC} = \left(\frac{\mu_A - \mu_C}{e}\right) \leq E_g$$

e is the magnitude of the electron charge. While the anode with m_A above LUMO will reduce the electrolyte, the cathode with m_C below HOMO will oxidize electrolyte unless a passivation layer (commonly known as solid electrolyte interface (SEI)) blocks the electron transfer at the electrodes. A passivating SEI layer at electrode/electrolyte boundary can give kinetic stability to a larger V_{OC} provided that eV_{OC}-E_g is not too large.

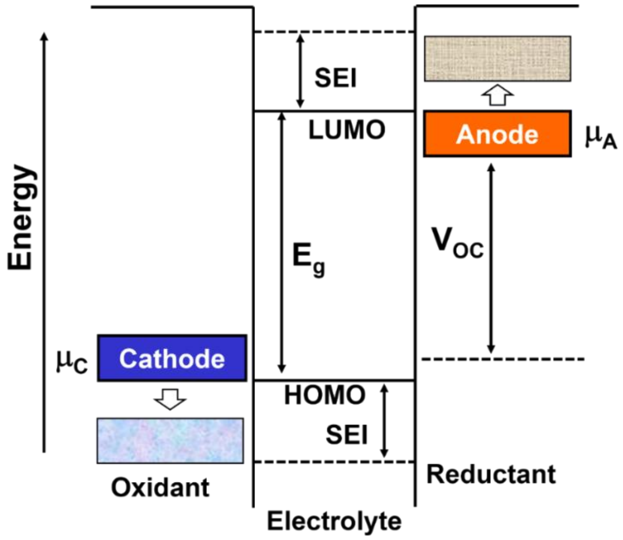

Figure 1.2. Schematic of open-circuit energy diagram of thermodynamically stable battery.[8]

In general, the gravimetry energy density of a battery is given by the product of the voltage (V) and the specific capacity (Ah/g) of the electrode. The specific capacity is calculated from Faraday's first law of electrolysis: (n · F / M) × 1000 / 3600 mA h g^{-1}, where n is the number of electrons exchanged in the electrochemical reaction, F is the Faraday's constant, and M is the molar weight of the electrode material. To achieve high energy density battery, it is necessary to find suitable anode and cathode which have a larger voltage difference and/or lighter mass.

1.3. Status on Na-ion cathodes

Since cathode materials play a crucial role in the cost, safety, cycle life, and overall energy density of the battery, significant attention has been devoted to exploring suitable candidates.[9,10] Good cathode material requires (i) high structural and chemical stability, (ii) high voltage and storage capacity, (iii) high electronic and sodium-ion conductivities, and (iv) low cost and safety. Although a wide range of compounds has been explored as plausible Na-ion cathodes (Figure 1.3), two classes of materials have received an incredible amount of attention, namely, layered oxides and polyanionic frameworks.

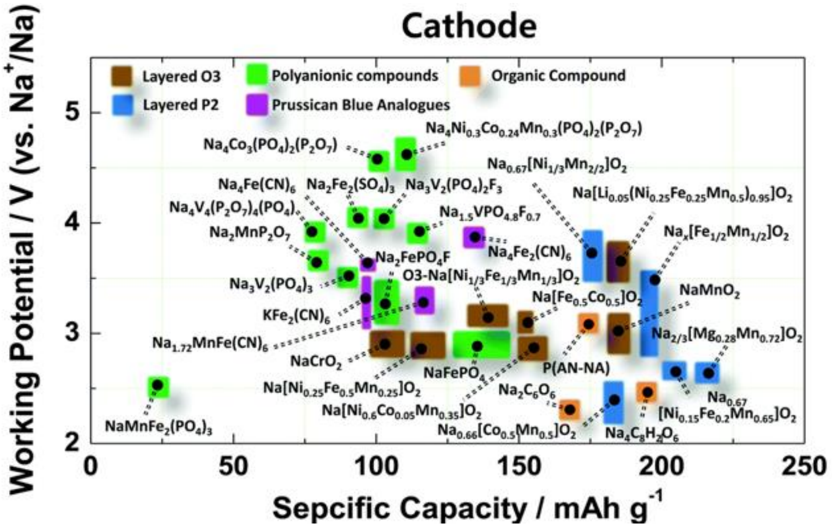

Figure 1.3. Voltage *vs*. capacity plot of Na-ion cathodes.[6]

1.3.1. Layered Transition Metal Oxides

Sodium-based layered transition metal oxides (Na_xMO_2; M = transition metal) have been extensively explored, inspired by the success story of their Li-ion analogues in LIBs. Its crystal structure is built by alternating layers of edge shared MO_6 octahedra and Na-ions. According to Delmas *et al.*,[11] Na-ion layered oxides can be categorized into two main groups, O3 and P2 type. The first letter "O" and "P" denotes the types of sodium ion environment (i.e., octahedral and prismatic) and the "2" and "3" implies the number of transition metal layers in a single unit cell. Due to the larger ionic radii difference between sodium and transition metal cations, the cation mixing is avoided in $NaMO_2$ compounds compared to their Li-ion counterparts.[12] This fact enables the preparation of multi-transition metal-based oxides by high-temperature synthesis, which provides optimized SIBs.

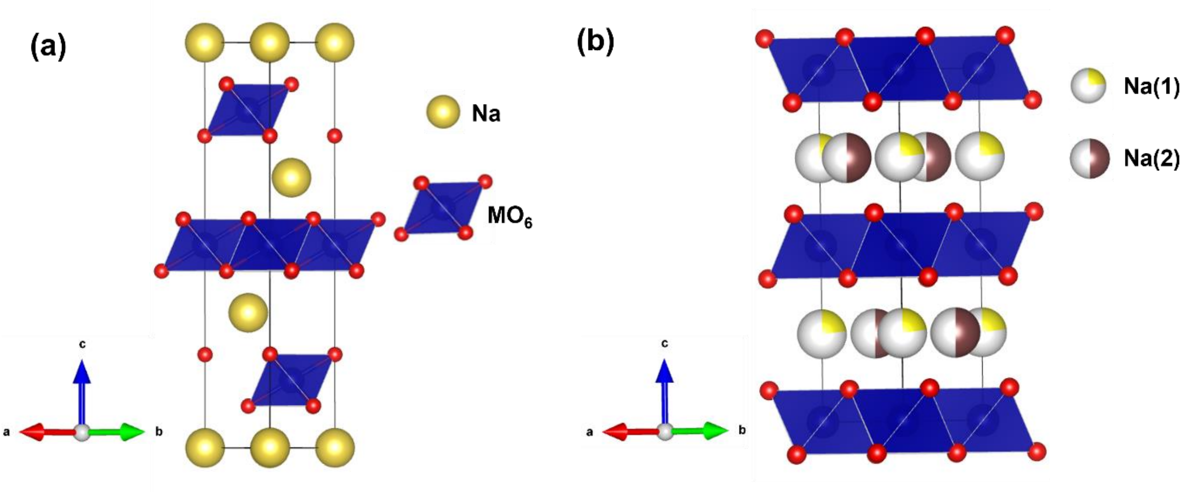

Fig 1.4. Crystal structure of (a) O3-and (b) P2- type Na-ion layered oxides.

From the viewpoint of application, O3 type oxides deliver higher storage capacities due to the presence of a large amount of sodium ions, whereas the P2 type framework provides faster sodium ion diffusion and higher rate performance. During their sodium (de)intercalation, O3 cathodes undergo a series of phase transformations (O3 ↔ O′3 ↔ P3 ↔ P′3), whereas P2

↔ O2/OP4 type phase transitions occur in P2 structure. However, the transformation between O3 and P2 type phases is not possible due to high energy demanding transition metal-oxygen bond breaking. All the single transition metal-based Na_xMO_2 (M = Ti to Ni) cathodes exhibit reversible sodium (de)intercalation, in contrast to their Li-ion counterparts.[12] The electrochemical performances of Na-ion layered oxide cathodes have been extensively reported in recent reviews[13,14,15] and herein, we will highlight some of the single- and multi-transition metal-based oxides. The O3 and P2 type Na_xCoO_2 cathodes were initially investigated by Delmas *et al.*,[16,17] which showed multi-step voltage profiles due to successive phase transformations during cycling. Recent *in-operando* XRD studies related these complex voltage signatures to various single and bi-phasic domains arising from Na^+/vacancy ordering at different sodium concentrations.[18,19] Layered $NaFeO_2$ and $NaMnO_2$ cathodes have received significant consideration due to their low cost and toxicity.[20,21] Unlike the electrochemically inactive $LiFeO_2$, the $NaFeO_2$ cathode shows reversible sodium (de)intercalation capacity of 120 mA h g^{-1} at 3.3 V *vs*. Na^+/Na^0 due to the redox activity of Fe^{3+}/Fe^{2+}. The $NaMnO_2$ cathode crystallizes in a monoclinic structure (O'3) due to Jahn-Teller distortion of Mn^{3+}. It reversible exchanges ~0.8 moles of sodium ions per formula unit (pfu), which is equivalent to 185 mA h g^{-1}.

Solid-solution layered oxides based on multi-transition metal cations have been extensively investigated to obtain higher intercalation voltages and capacities, and enhanced structural stability. Among them, Ni/Mn based oxides are attractive due to the high voltage operation of $Ni^{4+}/Ni^{3+}/Ni^{2+}$ couples and the presence of Jahn-Teller inactive Mn^{4+}, which enhances structural stability during cycling. P2-$Na_{2/3}Ni_{1/3}Mn_{2/3}O_2$ cathode displays high insertion voltage (3.7 V *vs*. Na^+/Na^0), theoretical capacity (173 mA h g^{-1}), and air-stability.[22,23] However, it suffers from poor capacity retention due to repeated P2 ↔ O2 phase transformation, which occurs *via* the gliding of oxygen layers. To alleviate this issue, divalent cations including Mg^{2+}, Cu^{2+} and Zn^{2+} were substituted in the P2-$Na_{2/3}Ni_{1/3-x}M'_xMn_{2/3}O_2$, which produced smoothed voltage profiles and better cycling performances.[24-28] Although, extensive research efforts have been escorted to develop layered oxide cathodes, their practical application still faces several challenges such as limited cycling stability, lower energy density, and air/moisture instability.

1.3.2. Polyanionic cathodes

Polyanionic cathodes containing transition metal redox centres and $(XO_4)^{n-}$ (X = B, Si, P, S) subunits show numerous advantages over their oxide counterparts.[29] First, versatile atomic arrangements and crystal structures can be obtained *via* tunning cationic and anionic sublattices. Second, these compounds exhibit extraordinary structural and cycling stabilities. Third and most importantly, they display higher intercalation voltages for a given $M^{(n+1)+}/M^{n+}$ redox couple compared to oxides owing to the inductive effect. It can be explained based on molecular orbital theory in which bonding and antibonding orbitals have O 2p and M 3d characters, respectively (Figure 1.5). The stronger M-O covalent bond generates a larger energy separation between the bonding and antibonding orbitals. Accordingly, the energy difference between the antibonding orbital and vacuum level decrease, which lowers the intercalation voltage. Upon introducing X atom in the polyanionic framework, which has higher electronegativity than M, the ionicity of M-O bond will be increased and thus, the intercalation voltage raises. Using this concept, the increasing intercalation voltage trend of $W < Mo < V < P < S$ based polyanions can be explained.

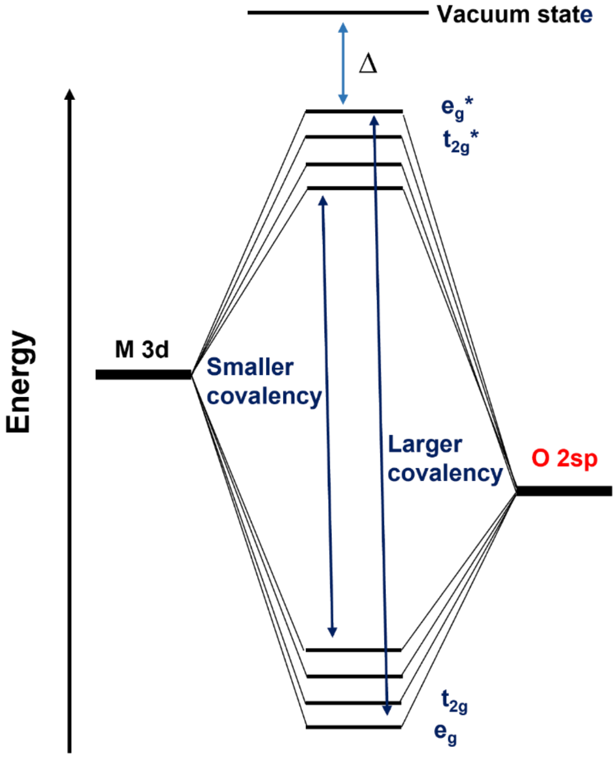

Figure 1.5. The molecular orbital covalency on the orbital energy level.[30]

1.3.2.1. Phosphate cathodes

Among the polyanionic cathodes, phosphate frameworks exhibit (i) robust thermal, structural and chemical stabilities, (ii) diversity in structural framework based on PO_4^{3-}, PO_3^- and $P_2O_7^{4-}$, and their combination and (iii) higher intercalation voltages. Although $LiFePO_4$ has attained huge commercial success, its sodium analogue, maricite-$NaFePO_4$, does not show any electrochemical activity due to the lack of sodium-ion conducting channels.[31] Alternatively, the delithiated olivine-$FePO_4$ cathode reversibly (de)intercalates one mole of sodium ions pfu, which is equivalent to 150 mA h g^{-1}.[32] The metastable olivine-$NaFePO_4$ exhibited poor sodium (de)intercalation kinetics due to slower Na-ion diffusion.[33]

The incorporation of fluorine into phosphate framework provides higher intercalation voltages, thus raising energy density of batteries. Along this line, Nazar *et al.*,[34] first demonstrated high voltage Na_2FePO_4F cathode for LIB application. Later the same materials was tested for SIB application by Tarascon and co-workers.[35] It showed two voltage plateaus at 3.1 and 2.9 V *vs.* Na^+/Na^0 with reversible capacities of 110 mA h g^{-1}.[36-38] Komaba *et al.*, reported Na_2CoPO_4F which is a high voltage electrode material for Na-ion batteries with capacity of 100 mA h g^{-1} for Co^{3+}/Co^{2+} redox at 4.3 V vs. Na^+/Na^0 when cycled in the voltage region of 2-5 V *vs.* Na^+/Na^0.[39]

Another fluorophosphate cathode $Na_3V_2(PO_4)_2F_3$ (space group: $P4_2/mnm$) has recently received significant attention because of its high voltage activity (~3.95 V *vs.* Na^+/Na^0). Its framework is made of bi-octahedral $V_2O_8F_3$ and tetrahedral PO_4 units. These bi-octahedra $V_2O_8F_3$ units are linked by one of the fluorine atoms. Tetrahedral PO_4 units are connected through oxygen atoms. This arrangement forms the channels along *a*- and *b*-axes where sodium is located in the tunnel sites. The channels present in the structure provide pathways for the diffusion of sodium ions. Na^+ ions occupy triangular prismatic site which is surrounded by two F^- and four O^{2-} ions or an augmented triangular prismatic site attached to the F apex-square pyramid. These sites alternate to form a circle-like geometry repeated in the *ab*-plane. $Na_3V_2(PO_4)_2F_3$ cathode showed two plateaus at ~3.7 V and 4.2 V *vs.* Na^+/Na^0 during charge/discharge processes with reversible capacities of ~120 mA h g^{-1}.

1.3.2.2. NASICON

Sodium superionic conductor (NASICON) framework materials were initially explored as a solid-state Na-ion conductor by Hong and Goodenough in 1976.[40] In their pioneering work, a series of $Na_{1+x}Zr_2Si_xP_{3-x}O_{12}$ materials were investigated and the compound with x = 2 showed the highest sodium ion conductivity, the value comparable to β-alumina above 443 K. Thereafter, NASICON compounds bearing electrochemically active transition metal cations were explored for reversible alkali-ion insertion in 1980’s.[41,42] The NASICON electrode with a chemical formula $Na_xM_2(YO_4)_3$ (x = 0 - 4; Y = P, S, Si; M = early first and second row transition metals) generally crystalizes in $R\overline{3}c$ and *C2/c* space group. Its crystal structure is built by lantern units, containing two MO_6 units corner shared by three YO_4 units, and these lantern units are stacked along (001) direction. In this three-dimensional framework, sodium ions occupy two independent crystallographic sites, namely, Na(1) and Na(2), with coordination numbers of 6 and 8, respectively(Figure 1.6). Plashnitsa *et al.*,[43] first explored the sodium (de)intercalation properties of $Na_3V_2(PO_4)_3$ cathode using ionic liquid-based electrolyte and built a symmetric Na-ion cell, comprising the same active material as the anode and cathode. However, the symmetric cell exhibited unsatisfactory cycling performance. The sodium (de)intercalation in the $Na_3V_2(PO_4)_3$ cathode proceed *via* two-phase mechanism at 3.4 and 1.6 V *vs*. Na^+/Na^0, corresponding to the redox activity of V^{4+}/V^{3+} and V^{3+}/V^{2+}, respectively. Several strategies were reported to tailor $Na_3V_2(PO_4)_3$/carbon composite cathodes to improve the cycling performances.[44,45] For instance, Saravanan *et al.*,[46] synthesized porous $Na_3V_2(PO_4)_3$/C cathode, which showed stellar cycling performance (86.7 % capacity retention after 1000 cycles at 1C rate).

Alternatively, the electrochemical sodium (de)intercalation properties of $Na_3V_2(PO_4)_3$ cathode can also be tunned *via* alio- and iso-valent cationic substitutions in the place of vanadium. Along this line, Goodenough *et al.*,[47] partially substituted vanadium in $Na_3V_2(PO_4)_3$ structure with Mn^{2+} and Fe^{3+} to synthesize $Na_4VMn(PO_4)_3$ and $Na_3VFe(PO_4)_3$. Upon cycling in the voltage window of 3.8-2.5 V *vs*. Na^+/Na^0, the $Na_4VMn(PO_4)_3$ cathode showed two voltage plateaus at 3.3 (V^{4+}/V^{3+}) and 3.6 V (Mn^{3+}/Mn^{2+}) *vs*. Na^+/Na^0 with a capacity of 101 mA h g^{-1} at 1C current rate. In the same voltage window, the $Na_3VFe(PO_4)_3$ cathode displayed two voltage plateaus at 3.3 and 2.5 V *vs*. Na^+/Na^0 for V^{4+}/V^{3+} and Fe^{3+}/Fe^{2+} couples, respectively. Subsequently, $Na_4VMn(PO_4)_3$ was subjected to high voltage window cycling (4.2-2.5 V *vs*. Na^+/Na^0) to extract more sodium ions through activation of V^{5+}/V^{4+} and Mn^{4+}/Mn^{3+} redox couples at higher voltages.[48-50] As expected, it delivered a higher first charge capacity of ~150 mA h g^{-1} (equivalent to 3 Na extraction) due to cumulative redox activities of $V^{5+}/V^{4+}/V^{3+}$ and $Mn^{4+}/Mn^{3+}/Mn^{2+}$ couples. However, the subsequent discharge was irreversible due to bulk structural rearrangement of the cathode at higher voltages. Similarly, the $Na_3V_2(PO_4)_3$ cathode substituted with electrochemically inactive cations such as Cr^{3+}, $Al^{3+,}$ and Mg^{2+} produced similar structural degradation and capacity decay during high voltage cycling.[51-55] Electrochemically sodiated NASICON-$Na_4VFe(PO_4)_3$ showed specific capacity of 153 mA h g^{-1}, corresponding to the redox activities of Fe^{3+}/Fe^{2+}, V^{4+}/V^{3+} and V^{5+}/V^{4+} redox when cycled in the voltage range of 4.3-1.3 V *vs.* Na^+/Na^0 at C/20 rate.[56] $Na_3VCr_{1-x}Al_x(PO_4)_3$ (x = 0-1) pure samples were synthesized by Tirado *et al.*, which show redox activity of V^{4+}/V^{3+} and V^{5+}/V^{4+}couples in the voltage range of 2-4.3 V *vs.* Na^+/Na^0.[57] As the amount of Al^{3+} substitution increases, a downward potential shift was observed. Replacement of Cr^{3+} by Al^{3+} enhanced the electrochemical performance of the NASICON-$Na_3VCr_{1-x}Al_x(PO_4)_3$ cathodes (69.8 mA h g-1 after 25 cycles at 5C rate). Another series of NASICON-$Na_{4-x}VFe_xMn_{1-x}(PO_4)_3$ (x=0-1) series were synthesized *via* sol-gel assisted route which show combined redox activities of V^{4+}/V^{3+}, Mn^{3+}/Mn^{2+} and Fe^{3+}/Fe^{2+} couples.[58]

Although $Na_3V_2(PO_4)_3$-type cathodes show stellar electrochemical performances, they utilize expensive and toxic vanadium, limiting its practical application. To address this issue, Goodenough *et al.*,[59] developed a low-cost $Na_3TiMn(PO_4)_3$ cathode, which delivered reversible capacities of 80 mA h g^{-1} *via* the operations of Mn^{3+}/Mn^{2+} and Mn^{4+}/Mn^{3+} couples at 3.6 V and 4.1 V *vs*. Na^+/Na^0, respectively. However, it exhibited severe capacity decay upon long-term cycling due to the Jahn-Teller effect of Mn^{3+}. Later, the same group synthesized

$Na_3MnZr(PO_4)_3$, which showed improved cycling stability (91% of initial capacity retention after 500 cycles at 0.5C rate) due to suppressed Jahn-Teller distortion of Mn^{3+}.[60]

Recently, another NASICON-$Na_3Cr_2(PO_4)_3$ cathode was reported for its high voltage operation (4.5 V *vs*. Na^+/Na^0) with a limited initial capacity of 80 mA h g^{-1}.[61] However, its capacity was quickly faded to 5 mA h g^{-1} within first 20 cycles, presumably due to electrolyte oxidation and structural degradation due to the disproportionation reaction of Cr^{4+} to Cr^{3+} and Cr^{6+}. To stabilize the structure and improve the cycling performance, Xiu Song Zhao *et al.*, synthesized $Na_2TiCr(PO4)_3$ cathode in which electrochemically inactive Ti^{4+} cation enhance structural stability.[53] Although it showed a lower initial reversible capacity of ~50 mA h g^{-1}, it was sustained for 300 cycles with a capacity retention of 90%. Similar to the strategy of replacing vanadium with manganese in the NASICON framework, $Na_4CrMn(PO_4)_3$ cathode was independently developed by Prof. Ceder's and Prof. Chen's groups. It showed a high specific capacity of 160 mA h g^{-1}, involving Mn^{2+}/Mn^{3+}, Mn^{3+}/Mn^{4+}, and Cr^{3+}/Cr^{4+} redox couples.[62,63]

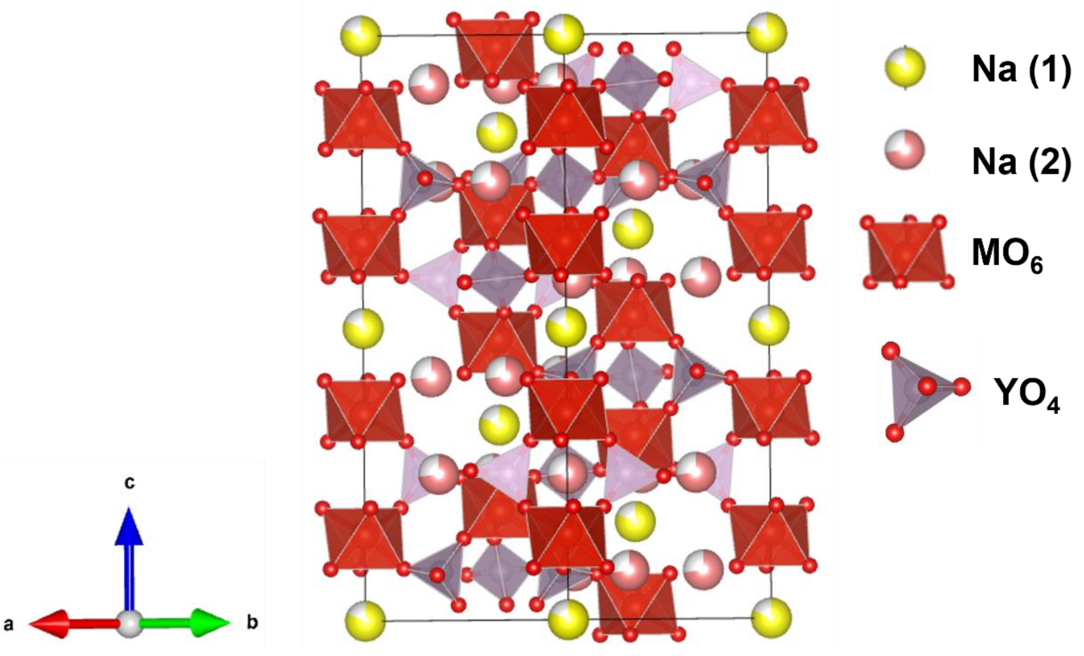

Figure 1.6. Crystal structure of NASICON framework ($Na_xM_2(YO_4)_3$).

1.4. Scope of the thesis

During the past decade, the battery community has produced numerous Na-ion materials, thanks to the materials design knowledge gained from Li-ion chemistry. Although layered oxides are in serious pursuit for their practical application, they still suffer from several issues like voltage and capacity fade, structural degradation, limited cycle life and air instability. On the other hand, polyanionic materials offer high voltages, structural and cycling stabilities. However, they deliver moderate capacities (~ 100-120 mA h g^{-1}) due to the electrochemically inactive polyanionic units. This thesis revolves around exploring high voltage and high capacity NASICON phosphate cathodes for Na-ion battery application. NASICON framework is appealing since it displays high sodium ion mobility, structural, chemical, and cycling stabilities. More importantly, it can exchange up to four moles of sodium ions *pfu* in theory, corresponding to the capacities of 200-220 mA h g^{-1}. However, the present NASICON cathodes deliver practical capacities in the range of 80-100 mA g^{-1}, which is equivalent to the exchange of ~1.5 to 2 moles of Na ions *pfu*.

We have chosen NASICON-$Na_3V_2(PO_4)_3$ cathode as the starting precursor since it shows reversible capacities of ~110 mA h g^{-1} (equivalent to 2 Na exchange *pfu*) at high voltage 3.45 V *vs*. Na^+/Na^0 with stellar cycling and rate performances. Systematic *alio*- and *iso*-valent cationic (Mn^{2+}, Mg^{2+}, Al^{3+} and In^{3+}) substitutions are attempted into the NASICON-$Na_3V_2(PO_4)_3$ cathode to activate multi-redox centres and thereby increase the storage capacities. Such substitutions are expected to facilitate tunning insertion voltages, sodium (de)intercalation mechanism, sodium diffusion, and structural stability. A myriad of experimental and computational techniques has been used to understand the structure-electrochemical sodium (de)intercalation property relationship of these NASICON cathodes and optimize their performances. This thesis work highlights how important it is to tune

NASICON framework *via* chemical substitution to accomplish high performance NASICON cathodes for Na-ion battery application.

References

[1] Z. Yang, J. Zhang, M. C. W. Kintner-Meyer, X. Lu, D. Choi, J. P. Lemmon, J. Liu, *Chem. Rev.* **2011**, *111*, 3577.

[2] B. Dunn, H. Kamath, J-M. Tarascon, *Science,* **2011**, *334*, 928.

[3] J. M. Tarascon, *Electrochem. Soc. Interface*, **2016**, *25*, 79.

[4] Y. Tian , G. Zeng, A. Rutt, T. Shi, H. Kim, J. Wang, J. Koettgen, Y. Sun, B. Ouyang, T. Chen, Z. Lun, Z. Rong , Kristin Persson , G. Ceder, *Chem. Rev.* **2021**, *121*, 1623.

[5] N. Yabuuchi, K. Kubota, M. Dahbi, S. Komaba, *Chem. Rev.* **2014**, *114*, 11636.

[6] J. Y. Hwang, S. T. Myung, Y. K. Sun, *Chem. Soc. Rev.* **2017**, *46*, 3529.

[7] J. B. Goodenough, *Solid State Ionics*, **1994**, *69*, 184.

[8] J. B. Goodenough, Y. Kim, *Chem. Mater.* **2010**, *22*, 587.

[9] J. Xiao, X. Li, K. Tang, D. Wang, M. Long, H. Gao, W. Chen, C. Liu, H. Liu, G. Wang, *Mater. Chem. Front.* **2021**, *5*, 3735.

[10] X. Xiang, K. Zhang, J. Chen, *Adv. Mater.* **2015**, *27*, 5343.

[11] C. Delmas, C. Fouassier, P. Hagenmuller, *Physica B+C*, **1980**, *99*, 81.

[12] K. Kubota, S. Kumakura, Y. Yoda, K. Kuroki, S. Komaba, *Adv. Energy Mater.* **2018**, *8*, 1703415.

[13] Y. Xiao, N. M. Abbasi, Y-F. Zhu, S. Li, S.-J. Tan, W. Ling, L. Peng, T. Yang, L. Wang, X-D. Guo, Y-X. Yin, H. Zhang, Y-G. Guo, *Adv. Funct. Mater*. **2020**, *30*, 2001334.

[14] M. H. Han, E. Gonzalo, G. Singh, T. Rojo, *Energy Environ. Sci*. **2015**, *8*, 81.

[15] P-F. Wang, Y. You, Y-X. Yin, Y-G. Guo, *Adv. Energy Mater*. **2018**, *8*, 1701912.

[16] C. Delmas, J.-J. Braconnier, C. Fouassier, P. Hagenmuller, *Solid State Ionics*, **1981**, *3-4*, 165.

[17] J-J. Braconnier, C. Delmas, C. Fouassier, P. Hagenmuller, *Mat. Res. Bull*. **1980**, *15*, 1797.

[18] R. Berthelot, D. Carlier, C. Delmas, *Nature Materials*, **2011**, *10*, 74.

[19] Y. Lei, X. Li, L. Liu, G. Ceder, *Chem. Mater.* **2014**, *26*, 5288.

[20] H. Wang, R. Gao, Z. Li, L. Sun, Z. Hu, X. Liu**,** *Inorg. Chem.* **2018**, *57*, 5249.

[21] Y. Takeda, K. Nakahara, M. Nishijima, N. Imanishi, O. Yamamoto, M. Takano, R. Kanno, *Mat. Res. Bull.* **1994**, *29*, 659.

[22] Z. Lu, J. R. Dahn, *J. Electrochem. Soc.* **2001**, *148*, A1225.

[23] Z. Lu, J. R. Dahn, *Chem. Mater.* **2001**, *13*, 1252.

[24] N. Tapia-Ruiz, W. M. Dose, N. Sharma, H. Chen, J. Heath, J. W. Somerville, U. Maitra, M. S. Islam, Peter G. Bruce, *Energy Environ. Sci.* **2018**, *11*, 1470.

[25] X. Wu , G.-L. Xu , G. Zhong , Z. Gong , J. McDonald , S. Zheng , R. Fu , Z. Chen , K. Amine, Y. Yang, *ACS Appl. Mater. Interfaces*, **2016**, *8*, 22227.

[26] H. Yoshida , N. Yabuuchi , K. Kubota , I. Ikeuchi , A. Garsuch , M. Schulz-Dobrickb, S. Komaba, *Chem. Commun.* **2014**, *50* , 3677.

[27] X. Wu , J. Guo , D. Wang , G. Zhong , M. J. McDonald, Y. Yang, *J. Power Sources*, **2015**, *281*, 18.

[28] L. Wang , Y.-G. Sun , L.-L. Hu , J.-Y. Piao , J. Guo , A. Manthiram , J. Ma and A.-M. Cao, *J. Mater. Chem. A*, **2017**, *5* , 8752.

[29] C. Masquelier, L. Croguennec, *Chemical Reviews*, **2013**, *113*, 6552.

[30] P. Barpanda, D. Dwibedi, S. Ghosh, Y. Kee, S. Okada, *Ionics*, **2015**, *21*, 1801.

[31] K. Zaghib, J. Trottier, P. Hovington, F. Brochu, A. Guerfi, A. Mauger, C. M. Julien, *Journal of Power Sources*, **2011**, *196*, 9612.

[32] P. Moreau, D. Guyomard, J. Gaubicher, F. Boucher, *Chem. Mater.* **2010**, *22*, 4126.

[33] Y. Zhu, Y. Xu, Y. Liu, C. Luo, C. Wang, *Nanoscale*, **2013**, *5*, 780.

[34] B. L. Ellis, W. R. M. Nakahnouk, Y. Makimura, K. Toghill, L. F. Nazar, *Nat. Mater.* **2007**, *6*, 749.

[35] N. Recham, J.-N. Chotard, L. Dupont, K. Djellab, M. Armand, J. M. Tarascon, *J. Electrochem. Soc.* **2009**, *156*, A993.

[36] M. Bianchini, N. Brisset, F. Fauth, F. Weill, E. Elkaim, E. Suard, C. Masquelier, L. Croguennec, *Chem. Mater.* **2014**, *26*, 4238.

[37] P. Serras, V. Palomares, J. Alonso, N. Sharma, J. M. López del Amo, P. Kubiak, M. L. Fdez-Gubieda, T. Rojo, *Chem. Mater.* **2013**, *25*, 4917.

[38] N. Sharma, P. Serras, V. Palomares, H. E. A. Brand, J. Alonso, P. Kubiak, M. L. Fdez-Gubieda, T. Rojo, *Chem. Mater.* **2014**, *26,* 3391.

[39] K. Kubota, K. Yokoh, N. Yabuuchi, S. Komaba, *Electrochemistry*, **2014**, *82*, 909.

[40] J. B. Goodenough, H. Y-P. Hong, J. A. Kafalas, *Mat. Res. Bull*. **1976**, *11*, 203.

[41] C. Delmas, F. Cherkaoui, A. Nadiri, P. Hagenmuller, *Mat. Res. Bull.* **1987**, *22*, 631.

[42] A. Manthiram, J. B. Goodenough, *Journal of Power Sources*, 1989, 26, 403.

[43] L. S. Plashnitsa, E. Kobayashi, Y. Noguchi, S. Okada, J-i. Yamaki, *J. Electrochem. Soc.* **2010,** *157*, A536.

[44] Z. Jian , W. Han , X. Lu , H. Yang, Y-S. Hu, J. Zhou, Z. Zhou, J. Li, W. Chen, D. Chen, L. Chen, *Adv. Energy Mater*. **2013**, *3*, 156.

[45] Z. Jian, L. Zhao, H. Pan, Y-S. Hu, H. Li, W. Chen, L. Chen, *Electrochemistry Communications*, **2012**, *14*, 86.

[46] K. Saravanan, C. W. Mason, A. Rudola, K. H. Wong, P. Balaya, *Adv. Energy Mater*. **2013**, *3*, 444.

[47] W. Zhou, L. Xue, X. Lü, H. Gao, Y. Li, S. Xin, G. Fu, Z. Cui, Y. Zhu, J. B. Goodenough, *Nano Lett*. **2016**, *16*, 7836.

[48] F. Chen, V. M. Kovrugin, R. David, O. Mentré, F. Fauth, J. N. Chotard, C. Masquelier, *Small Methods*, **2019**, *3*, 1800218.

[49] M. V. Zakharkin, O. A. Drozhzhin, I. V. Tereshchenko, D. Chernyshov, A. M. Abakumov, E. V. Antipov, K. J. Stevenson, *ACS Appl. Energy Mater*. **2018**, *1*, 5842.

[50] S. Ghosh, N. Barman, M. Mazumder, S. K. Pati, G. Rousse, P. Senguttuvan, *Adv. Energy Mater*. **2020**, *10*, 1902918.

[51] R. Liu, G. Xu, Q. Li, S. Zheng, G. Zheng, Z. Gong, Y. Li, E. Kruskop, R. Fu, Z. Chen, K. Amine, Y. Yang; *ACS Appl. Mater. Interfaces*, **2017**, *9*, 43632.

[52] J. Zhang, Y. Liu, X. Zhao, L. He, H. Liu, Y. Song, S. Sun, Q. Li, X. Xing, J. Chen, *Adv. Mater*. **2020**, *32*, 1906348.

[53] J. Zhang, G. Liang, C. Wang, C. Lin, J. Chen, Z. Zhang, X. S. Zhao, *ACS Appl. Mater. Interfaces*, **2020**, *12*, 28313.

[54] F. Lalere, V. Seznec, M. Courty, R. David, J. N. Chotard, C. Masquelier, *J. Mater. Chem. A*, **2015**, *3*, 16198.

[55] H. Li, H. Tang, C. Ma, Y. Bai, J. Alvarado, B. Radhakrishnan, S. P. Ong, F. Wua, Y. S. Meng, C. Wu, *Chem. Mater*. **2018**, *30*, 2498.

[56] S. Park, J. N. Chotard, D. Carlier, I . Moog, M. Courty, M. Duttine, F. Fauth, A. Iadecola, L. Cognuennec, C. Masquilier, *Chem. Mater*. **2021**, *33*, 5355.

[57] P. Lavela, R. Klee, J. L. Torado, *Sustainable Energy Fuels*, **2021**, *5*, 4095.

[58] P. Lavela, R. Klee, M. A. Hidalgo, J. L. Torado, *Journal of Electroanalytical Chemistry*, **2021**, *895*, 115533.

[59] H. Gao, Y. Li, K. Park, J. B. Goodenough, *Chem. Mater*. **2016**, *28*, 6553.

[60] H. Gao, I. D. Seymour, S. Xin, L. Xue, G. Henkelman, J. B. Goodenough, *J. Am. Chem. Soc*. **2018**, *140*, 18192.

[61] K. Kawai, W. Zhao, S-i. Nishimura, A. Yamada, *ACS Appl. Energy Mater*. **2018**, *1*, 928.

[62] J. Wang, Y. Wang, D-H. Seo, T. Shi, S. Chen, Y. Tian, H. Kim, G. Ceder, *Adv. Energy Mater*. **2020**, *10*, 1903968.

[63] J. Zhang, Y. Liu, X. Zhao, L. He, H. Liu, Y. Song, S. Sun, Q. Li, X. Xing, J. Chen, *Adv. Mater*. **2020**, *32*, 1906348.

Chapter 2

2. Experimental Techniques

2.1. Synthesis

The NASICON cathodes are synthesized *via* high-temperature solid-state synthesis route,[1-5] which is widely practiced in both laboratories and industries. We adapted this synthesis route in Chapter 3, which enables monitoring actual impact of chemical substitution without the interference of carbon-coating. In this method, initially all the precursors were taken in a stainless steel ball milling jar (25 ml) and ball milled for 30 minutes (weight of powder to ball ratio : 1:20). Thereafter, the powder was collected and annealed at 350 °C under N_2 atmosphere and 750 °C under Ar/H_2 (5 mol%) atmosphere for 10 and 12 h, respectively with an intermittent grinding. For the sol-gel assisted solid-state synthesis,[6-8] V_2O_5 was first reduced by citric acid in the distilled water for overnight at room temperature followed by addition of other precursors into the solution. The solution was thoroughly mixed and subsequently dried at 100 °C. The collected powder was annealed in the similar conditions as mentioned above. Note that the sol-gel assisted route is well known for producing nanoparticles embedded in carbon matrix.

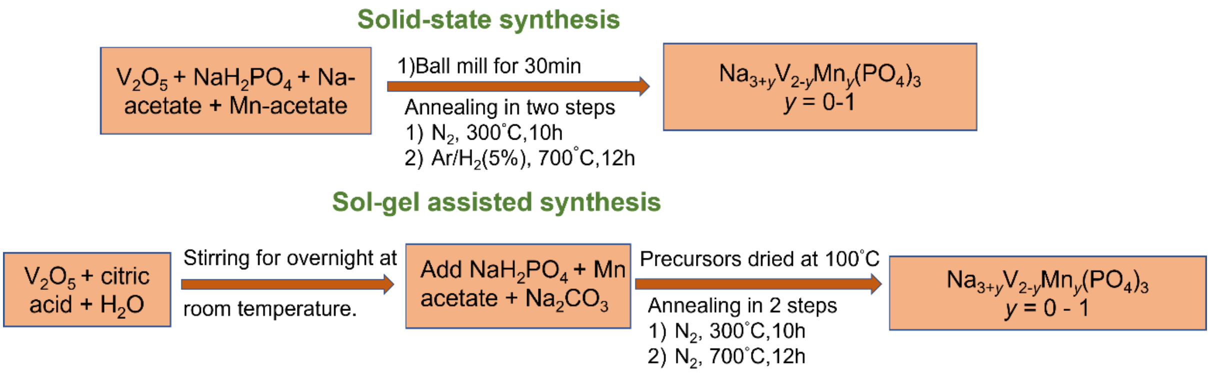

Schematic 2.1. Synthesis of NASICON cathodes *via* solid-state and sol-gel assisted synthesis routes.

2.2. Material Characterization

Powder X-ray diffraction is an analytical technique used for the determination of phase purity and crystal structure of materials. The XRD patterns displayed in this thesis were on a Bruker D8 diffractometer using Cu-Kα source (l = 1.5406 Å) in the 2θ region of 10-100°. The recorded XRD patterns were initially analyzed with ICSD data base to check for the phase formation and the presence of impurities. Thereafter, the patterns were refined using Rietveld method with the FullProf program.[9] It utilizes the least square approach to refine a theoretical diffraction pattern until it matches the experimental one, to obtain lattice parameters, atomic positions, site occupancies and thermal factors.

Temperature dependent *in-situ* XRD measurement was performed in the same Bruker D8 diffractometer under vacuum. The sample was heated from room temperature to 700 °C followed by cooling back to room temperature at the rate of 5 °C/min. The XRD patterns were collected at the interval of 100 °C for one hour.

The as-synthesized phosphate cathode materials were examined by scanning electron microscope (Jeiss Ultra-55 SEM instrument) to get the microstructures. Carbon, hydrogen, and nitrogen (CHN) analysis was conducted on a Perkin–Elmer EA 2400 instrument. Thermogravimetric analysis (TGA, Mettler Toledo) was performed in the temperature range of 30 to 500 °C at 10 °C min^{-1} in air. DSC experiment was conducted using a TA DSC Q 2000 instrument in Ar atmosphere in the temperature range -20 to 190 °C at 5 °C/min rate. To determine the content of Na/V/Mn/Mg/Al in the NASICON samples, the elemental analyses were performed using flame atomic absorption spectrometer (AnalytikJena novAA-350).

X-absorption spectroscopic (XAS) studies of the as-synthesized NASICON compounds (studied in Chapter 3, 4 and 6) and their electrodes with different state-of-charge were performed at the PETRA-III (P65 beamline, operating at 100 mA and 7.0 GeV) of Deutsches Elektronen-Synchrotron (DESY). The as-synthesized NASICON samples were mixed with boron nitride and pressed into pellets (13 mm diameter, thickness 0.5-0.9 mm). The NASICON electrodes harvested from electrochemical cells were packed inside Kapton tape to avoid air exposure during the XAS measurements. For data collection purpose the electrodes at different charge states and the pellets were sealed in Kapton tape. The edge energy of 5349 eV was chosen for vanadium at the inflection point with the energy resolution of 1eV. Each measurement was calibrated to the absorption energy of V metal plate reference. A double crystal monochromator consistent of parallel Si (1 1 1) crystals was used for the measurement in transmission mode. Three consecutive ionization detectors, filled with gas mixtures of (first) 1250 mbar N_2, 750 mbar He; (second) 250 mbar Ar, 1000 mbar N_2, 750 mbar He; (third) 1000 mbar N_2, 300 mbar He, 700 mbar Ar, are at a pathlength of 30 cm. AutoBK algorithm as implemented in Athena and a graphical front-end for the IFFEFIT software package were used for the normalization of data and removal of background.[10,11]

X-ray absorption spectroscopy (XAS) measurements were performed on the $Na_3VIn(PO_4)_3$ cathodes (studied in Chapter 5) at V K-edge (5464 eV) in a transmission mode at Beamline 8 (BL8), Synchrotron Light Research Institute (SLRI), Thailand using Ge (220) double crystal monochromator with storage ring running at 1.2 GeV and beam current of 80-150 mA.[12] X-ray absorption near edge structure (XANES) and extended X-ray absorption fine structure (EXAFS) spectra were divided into three regions with the following relative energy ranges and energy step: -200 to -20 eV (5 eV step), -20 to 80 eV (0.3 eV step) and 80 eV to 15k (0.05k step). Dwell time of each step was 1 second and three scans were collected from each sample. The normalization procedure of XANES spectra, including the pre-edge and post-edge background subtraction was achieved using the ATHENA program. The EXAFS spectra were converted by Fourier transform from *k* space to real space using a k^3 – weighting factor and without phase correction. All spectra were normalized using the ATHENA program.

Room temperature ^{23}Na and ^{31}P solid-state nuclear magnetic resonance (NMR) spectra were collected (in collaboration with Dr. R. J. Clément’s group from University of California Santa Barbara) on $Na_{3+y}V_{2-y}Mg_y(PO_4)_3$ powder samples using a 7.05 T (300 MHz for ^{1}H) Bruker superwide bore NMR spectrometer equipped with an Avance III console and operating at Larmor frequencies of 79.39 MHz and 121.5 MHz, respectively**.** Additional ^{23}Na solid-state NMR experiments were performed at 18.8 T (800 MHz for ^{1}H) on a Bruker standard bore NMR spectrometer equipped with an Avance III console and operating at a Larmor frequency of 211.65 MHz. All NMR spectra were obtained under magic angle spinning (MAS) at a rate of 30 kHz using a 2.5 mm double-resonance HX probe. The ^{23}Na spectra were referenced against a 1M NaCl solution ($\delta(^{23}Na) = 0$ ppm), and the ^{31}P spectra against a 1M H_3PO_4 solution ($\delta(^{31}P) = 0$ ppm). Line shape analysis was carried out within the Bruker TopSpin software using the SOLA line shape simulation package. ^{23}Na and ^{31}P NMR spectra were recorded using a rotor-synchronized spin echo ($90° - \tau_R - 180° - \tau_R$ – acq). Low field (7.05 T) ^{23}Na spin echo were obtained using a 90° RF pulse of 0.8 μs and a 180° pulse of 1.6 μs at 300 W, with a recycle delay of 100 ms and averaged over 16,384 transients. High field (18.8 T) ^{23}Na NMR data were obtained using a 90° RF pulse of 0.97 μs and a 180° pulse of 1.94 μs at 200 W, with a recycle delay of 100 ms and averaged over 4,096 transients. Low field (7.05 T) ^{31}P spin echo spectra were obtained using a 90° RF pulse of 1.1 μs and a 180° pulse of 2.2 μs at 250 W, with a recycle delay of 100 ms.

2.3. Electrochemical Characterization:

All electrochemical tests of the NASICON cathode materials were performed in two-electrode Swagelok cells. The cathode materials were mixed with carbon (C45 TIMCAL) and polyvinylidene fluoride (PVDF) binder in a weight ratio of 70:22:8 in N-Methyl-2-pyrrolidone solvent. The slurry was coated on aluminum foil and dried under vacuum at 90 °C for overnight. Thereafter, electrodes were punched into 10 mm diameter discs and the mass loading of active materials was found be ~2.0-3.0 mg cm^{-2}. Sodium (Sigma, >99%) metal was used as the counter electrode and 1 M $NaClO_4$ in EC/PC/DMC (in a weight ratio of 4.5:4.5:0.1) with 3 wt% FEC was used as the electrolyte. The cells were assembled in an Ar-filled glovebox (O_2 < 0.1 ppm, H_2O < 0.1 ppm) and evaluated in a battery cycler (BT-lab, Biologic) over the voltage range 3.8-2.75 V *vs*. Na^+/Na^0 at different C-rates.

Galvanostatic intermittent titration technique (GITT) measurements were performed to understand the kinetics of sodium (de)intercalation into NASICON cathodes. GITT experiments were carried out by applying a constant current of C/10 for 1 h followed by a relaxation time of 1 h. The calculation of D/R^2 is carried out using the following equation [13]

$$\frac{D}{R^2} = \frac{4}{\pi\tau}\frac{(\Delta E_s)^2}{(\Delta E_\tau)^2}$$

D is the diffusion coefficient of sodium ion and R is the particle radius. ΔE_s and ΔE_τ represent the steady state voltage change due to the current change and the voltage change during the constant current pulse, eliminating the iR drop, respectively. The value of D/R^2 corresponds to inverse of time constant associated with sodium ion diffusion process. Note that we have not attempted to calculate the D values (from D/R^2) because of inaccuracy about the particle radius measurement using SEM.

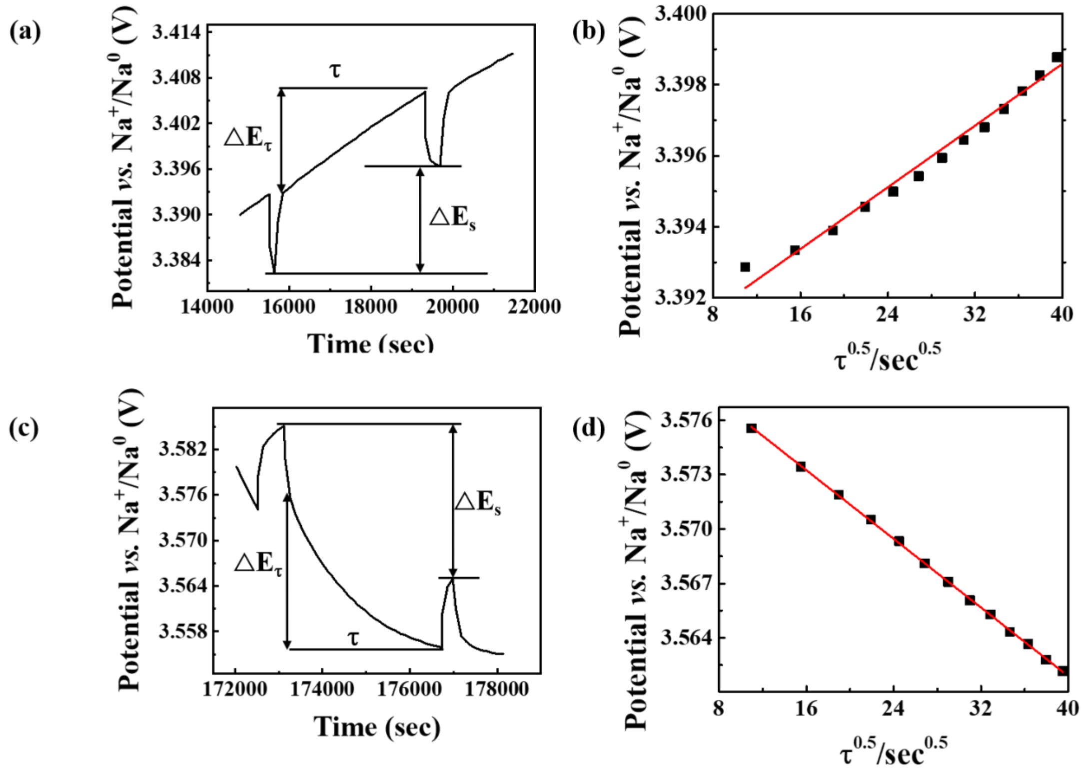

Figure 2.2. Schematic graph of a single GITT step of the NASICON-$Na_4VMn(PO_4)_3$ cathode (a) at ~3.395 V during charging and (c) ~3.570 V during discharging, and (b, d) their corresponding linear potential vs. $\tau^{0.5}$ plots.[6]

For *ex-situ* XRD analysis, the electrodes were coated on pin hole free thin aluminum foil (99.99%, Alfa, 10-micron thickness). The electrodes were harvested from the Swagelok cells at different state-of-charge, washed and dried inside the glove box. Then, they were mounted on a glass plate upside down in a way which Al foil serves as the window and were hermitically sealed with Kapton tape.

In-operando XRD measurements were conducted using the same BRUKER D8 diffractometer with Cu-Kα source in an *in-situ* electrochemical cell fitted with Be window. The cell was cycled at a C/10 rate in different voltage windows. Each pattern was recorded in the 2θ range of 10 to 60° for one hour. Selected *in-situ* XRD patterns were refined using Le Bail method to obtain cell parameters.

2.4. Theoretical calculations

First Principles Density Functional Theory (DFT) calculations were performed (in collaboration with Prof. S. K. Pati's group at JNCASR) using the PAW (Projector Augmented Plane Wave)[14] formalism as implemented in VASP (Vienna Ab-Initio Simulation Package).[15-17] The PBE (Perdew-Burke-Ernzerhorf) functional under the Generalized Gradient Approximation (GGA) was used to treat exchange and correlation effects.[18] A Hubbard U correction term (U_V = 3.25 eV, U_{Mn}=3.59 eV) was employed to treat electronic correlation in transition metal 3d orbitals, with the effective on-site exchange interaction parameter J fixed to 1 eV. A Kinetic Energy cutoff of 520 eV was used for PW expansion. The Brillouin Zone integration was performed using a 2x2x1 Monkhorst-Pack grid. All systems were optimized using the conjugate-gradient algorithm with a convergence criterion of 10^{-4} eV on energy 10^{-4} eV Å^{-1} for residual forces. Crystal symmetry was preserved for all configurations.

Bader charge analysis was performed using a code developed by Henkelman *et al.* to determine the evolution of atomic charges and V-O bonding across the compositional series.[19]

The Climbing-Image Nudged Elastic Band (CI-NEB) method was utilized to determine activation barriers for Na ion hopping. For single ion hops, a path was interpolated from a filled Na site to the nearest vacant Na site.[20]

References

[1] J. B. Goodenough, H. Y-P. Hong, J. A. Kafalas, *Mat. Res. Bull.* **1976**, *11*, 203.

[2] C. Delmas, F. Cherkaoui, A. Nadiri, P. Hagenmuller, *Mat. Res. Bull.* **1987**, *22*, 631.

[3] L. S. Plashnitsa, E. Kobayashi, Y. Noguchi, S. Okada, J-i. Yamaki, *J. Electrochem. Soc.* **2010,** *157*, A536.

[4] Z. Jian , W. Han , X. Lu , H. Yang, Y-S. Hu, J. Zhou, Z. Zhou, J. Li, W. Chen, D. Chen, L. Chen, *Adv. Energy Mater*. **2013**, *3*, 156.

[5] Z. Jian, L. Zhao, H. Pan, Y-S. Hu, H. Li, W. Chen, L. Chen, *Electrochemistry Communications*, **2012**, *14*, 86.

[6] K. Saravanan, C. W. Mason, A. Rudola, K. H. Wong, P. Balaya, *Adv. Energy Mater*. **2013**, *3*, 444.

[7] W. Zhou, L. Xue, X. Lü, H. Gao, Y. Li, S. Xin, G. Fu, Z. Cui, Y. Zhu, J. B. Goodenough, *Nano Lett*. **2016**, *16*, 7836.

[8] M. V. Zakharkin, O. A. Drozhzhin, I. V. Tereshchenko, D. Chernyshov, A. M. Abakumov, E. V. Antipov, K. J. Stevenson, *ACS Appl. Energy Mater*. **2018**, *1*, 5842.

[9] J. R. Carvajal, *Phys. B*, **1993**, *192*, 55.

[10] M. Newville, *J. Synchrotron Radiat.* **2001**, *8*, 322.

[11] B. Ravel, M. Newville, *J. Synchrotron Radiat.* **2005**, *12*, 537.

[12] W. Klysubun, P. Tarawarakarn, N. Thamsanong, P. Amonpattaratkit, C. Cholsuk, S. Lapboonrueng, S. Chaichuay, W. Wongtepa, *Radiation Physics and Chemistry*, **2020**, *175*, 108145.

[13] G. Assat, C. Delacourt, D. A. D. Corte, J.-M. Tarascon, *J. Electrochem. Soc*. **2016**, *163*, A2965.

[14] S. Ghosh, N. Barman, P. Senguttuvan, *Small*, **2020**, *16*, 2003973.

[15] G. Kresse, D. Joubert, *Phys. Rev. B: Condens. Matter Mater. Phys.* **1999**, *59*, 1758.

[16] G. Kresse, J. Hafner, *Phys. Rev. B* **1993**, *47*, 558.

[17] G. Kresse, J. Furthmüller, *Computational Materials Science* 1996, *6*, 15.

[18] G. Kresse, J. Furthmüller, *Phys. Rev. B* **1996**, *54*, 11169.

[19] W. Tang, E. Sanville, G. Henkelman, *Journal of Physics: Condensed Matter* **2009**, *21*, 084204.

[20] G. Henkelman, B. P. Uberuaga, H. Jonsson, *J. Chem. Phys*. **2000**, *113*, 9901.

Chapter – 3

High Capacity and High Rate NASICON-$Na_{3.75}V_{1.25}Mn_{0.75}(PO_4)_3$ Cathode for Na-ion Batteries *via* Modulating Electronic and Crystal Structures

Sodium superionic conductor (NASICON) cathodes are attractive for Na-ion battery (SIB) application as they exhibit both high structural stability and high sodium ion mobility. Herein, a comprehensive study is presented on the structural and electrochemical properties of the NASICON-$Na_{3+y}V_{2-y}Mn_y(PO_4)_3$ ($0 \leq y \leq 1$) series. A phase miscibility gap is observed at $y = 0.5$, defining two solid solution domains with low and high Mn contents. Although, members of each of these domains $Na_{3.25}V_{1.75}Mn_{0.25}(PO_4)_3$ and $Na_{3.75}V_{1.25}Mn_{0.75}(PO_4)_3$ reversibly exchange sodium ions with high structural integrity, the activity of Mn^{3+}/Mn^{2+} redox couple is found to be absent and present in the former and the later candidate, respectively. Galvanostatic cycling and rate studies reveal higher capacity and rate capability for the $Na_{3.75}V_{1.25}Mn_{0.75}(PO_4)_3$ cathode (100 and 89 mA h g^{-1} at 1C and 5C rate, respectively) in the $Na_{3+y}V_{2-y}Mn_y(PO_4)_3$ series. Such remarkable performance is attributed to optimum bottleneck size (~ 5 $Å^2$) and modulated V- and Mn-redox centers as deduced from Rietveld analysis and DFT calculations, respectively. This study shows how important it is to manipulate electronic and crystal structures to achieve high performance NASICON cathodes.

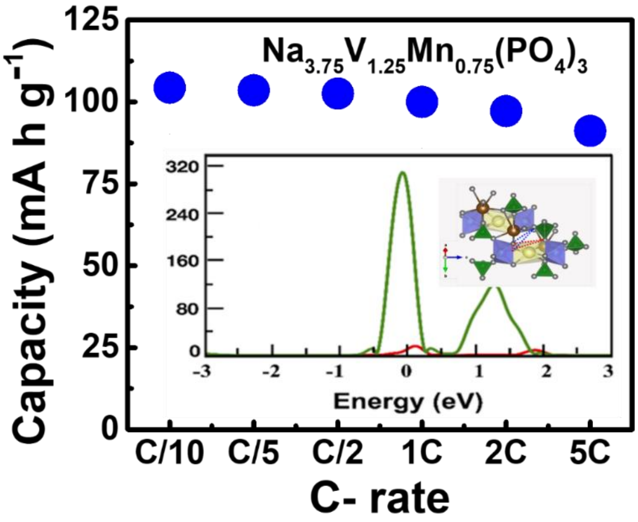

3.1. Introduction

The successful realization of Na-ion batteries relies on the exploration of high performance electrode materials which have high energy and power densities, low cost and safety.[1,2] Different classes of (P2, P3 and O3) layered oxides have been investigated as potential Na-ion cathodes, however, the issues related to their air stability, poor cyclability associated with successive phase transitions and large volume changes are yet to addressed.[3,4] On the other hand, polyanionic compounds exhibit high intercalation voltages for a given $TM^{(n+1)+}/TM^{n+}$ (TM = transition metal) redox couple and high structural stability in comparison with the layered oxides.[5] Recently, NASICON-type cathodes have been pursued in aqueous and non-aqueous Na-ion batteries, due to their higher Na-ion conductivities and rate capabilities.[6-8] Among them, $Na_3V_2(PO_4)_3$ (NVP) is attractive because of its high energy density (~ 400 Wh kg^{-1}), high structural and thermal stabilities.[9,10] It exhibits a flat voltage plateau at 3.4 V *vs.* Na^+/Na^0, which represents a two-phase reaction ($\mathrm{Na_3V_2(PO_4)_3} \leftrightarrow \mathrm{NaV_2(PO_4)_3} + 2\mathrm{Na}^+ + 2e^-$) operating on V^{4+}/V^{3+} redox couple. However, the NVP cathode, which consists of micron size particles and is free of conducive carbon coating, suffers from lower reversible capacities (~ 85 mA h g^{-1}) and Coulombic efficiencies (~< 90 %) and limited cycle life. Such inferior performances impede its practical application and can be attributed to its poor electronic conductivity and larger particle sizes.[11] Two major approaches are pursued to enhance its electrochemical performances: i) downsizing the NVP particles into nano-scale and coating them with conducive carbon,[12-23] and ii) partial substitution of alio-/iso-valent cations in the place of vanadium ions of the NVP lattice.[24-30] While the former approach is highly successful to achieve higher rate performances, Coulombic efficiencies and cycling stabilities, the energy density of the cathode is reduced because of the large amount of inactive carbon and lesser tap densities.

In the second approach, a variety of cations are doped/substituted in the NVP lattice to improve its electrochemical performances. Among them, the $Na_4VMn(PO_4)_3$ cathode developed by Goodenough's group is highly attractive because of its reduced cost and toxicity, and enhanced average intercalation voltage with respect to the unsubstituted NVP cathode (i.e., ~ 3.5 V for $Na_4VMn(PO_4)_3$ *vs.* 3.35 V for $Na_3V_2(PO_4)_3$).[31] It exhibits two-step voltage profiles (~ 3.4 V (V^{4+}/V^{3+}) and 3.6 V (Mn^{3+}/Mn^{2+})) with a reversible exchange of two moles of sodium ions. More importantly, it demonstrated higher rate performances and long-term cyclability (90 mA h g^{-1} at 1C rate for 1000 cycles). In the following study, Jiao *et al.* highlighted the importance of particle nano-sizing and carbon coating of the $Na_4VMn(PO_4)_3$ cathode to achieve superior rate performances and long cycle life.[32] The $Na_4VMn(PO_4)_3$ cathode synthesized by solid state method has exhibited limited reversible capacity (58 mA h g^{-1}), which is attributed to its poor electronic conductivity and larger particle size (> 5 μm). When the same cathode is made of small particles (< 200 nm) with conductive carbon network (8.6 wt.%), it shows stellar electrochemical performances (109 mA h g^{-1} at 0.5C and 87 % of capacity retention after 4000 cycles at 20C rate). Further, the $Na_4VMn(PO_4)_3$ cathode delivers higher first charge capacity (~150 mA h g^{-1} for an extraction of 3 mol of Na) upon high voltage oxidation, thanks to the activation of V^{5+}/V^{4+} couple at ~ 4.0 V *vs.* Na^+/Na^0. [33,34] However, it irreversibly transforms into another NASICON phase at higher voltages, which leads to its rapid capacity decay on the subsequent cycles. Overall, these reports have outlined the benefits of Mn substitution into the NVP lattice in terms of improving the cell voltage, storage capacities and cycling performances. However, they lack fundamental understanding on the effect of Mn substitution, i.e., how the structural and electrochemical properties of the NVP cathode can be varied upon different levels of substitution. Besides, most of them utilize carbon coated nanoparticles, thus the significance of substitution has been overlooked.

In the present work, we elucidate the role of Mn^{2+} on the structural and electrochemical sodium (de)intercalation properties of the $Na_{3+y}V_{2-y}Mn_y(PO_4)_3$ ($0 \leq y \leq 1$) cathodes. The systematic introduction of Mn^{2+} into the NVP lattice can alter the electronic structures of the cathodes, which is expected to improve the cell voltages through the participation of different V- and Mn-redox couples.[31,33] Further, it also increases the Na-ion concentration in the framework, which can affect its mobility.[35,36] Through these modulations, we demonstrate that high capacity and rate performances can be achieved for the $Na_{3.75}V_{1.25}Mn_{0.75}(PO_4)_3$ cathode, which has optimum bottleneck size and highly active V- and Mn-redox centers.

3.2. Experimental

$Na_{3+y}V_{2-y}Mn_y(PO_4)_3$ compounds were synthesized by solid state method. Stoichiometric amount of V_2O_5 (99.6%, Sigma), NaH_2PO_4 (99%, Sigma), Na_2CO_3 (99.5%, Sigma) and Mn-acetate (99%, Sigma) were mixed through high-energy ball milling (SPEX) for 30 min. The ball-milled product was subsequently annealed at 350 °C for 10 h and 700 °C for 12 h in Ar/H_2 (5 mol%) atmosphere with an intermittent grinding.

For the details on materials and electrochemical characterizations, and first-principle calculations, see Chapter 2.

3.3. Results and Discussion

3.3.1. Formation of solid solution

The crystal structure of NVP can be described as a three-dimensional framework made of so-called “lantern units”, consisting of two VO_6 octahedra corner shared with three PO_4 tetrahedra, stacked along [001]-direction (Figure 3.1a).[37] In this network, sodium ions occupy two independent sites, namely Na(1) and Na(2). Na(1) ions sit in six-coordinate sites in between two VO_6 octahedra to make infinite columns of $[O_3NaO_3VO_3NaO_3]$ along *c*-axis, which are connected by PO_4 units. Na(2) ions are located in between these columns in eight-fold coordination sites. The sodium-ion diffusion occurs from Na(1) to Na(2) through T1 and T2 bottleneck areas as shown in Figure 3.1b.[35,36] The substitution of aliovalent Mn^{2+} cation in the place of V^{3+} of the NVP structure is accompanied by the insertion of additional sodium ions with the final composition of $Na_{3+y}V_{2-y}Mn_y(PO_4)_3$ $(0 \leq y \leq 1)$.

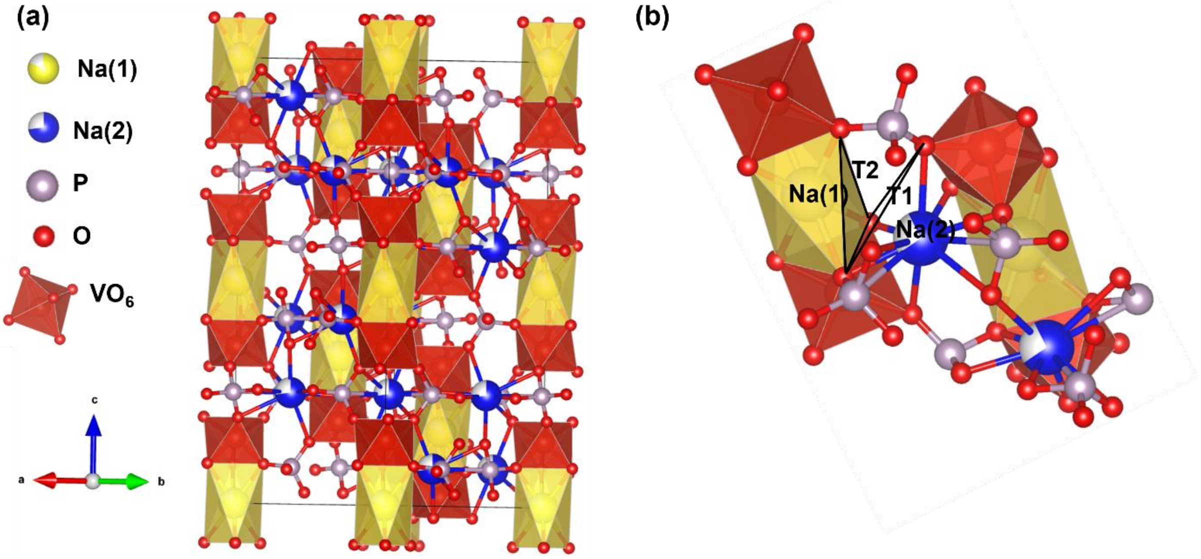

Figure 3.1. (a) Crystal structure of $Na_3V_2(PO_4)_3$. (b) T1 and T2 represent bottleneck areas for Na-ion diffusion.

The effect of Mn^{2+} substitution into the NVP structure was investigated based on the powder X-ray diffraction (XRD) patterns collected on the $Na_{3+y}V_{2-y}Mn_y(PO_4)_3$ $(0 \leq y \leq 1)$ samples (Figure 3.2a). The observed diffraction peaks of all the samples can be fully indexed with $R\bar{3}c$ space group and no extra reflections are noticed. The progressive shift of the diffraction peaks towards lower 2θ angles indicates the formation of solid solution and statistical distribution of Mn^{2+} and V^{3+} cations in the NVP structure. To grasp more insights on the structural changes upon Mn^{2+} substitution into the NVP structure, Rietveld analysis on the powder XRD patterns of the $Na_{3+y}V_{2-y}Mn_y(PO_4)_3$ samples were carried out (Figure 3.2a). The crystallographic details obtained from the refinements are displayed in Table 3.1 and 3.2. The

XRD pattern of the $y = 0.5$ sample presents broader peaks and it could only be fitted with two NASICON phases with $R\bar{3}c$ space group (Figure 3.2a). From the Rietveld refinement (Table 3.1), we could deduce an approximation of the compositions for these two phases: $Na_{3.3}V_{1.7}Mn_{0.3}(PO_4)_3$ (23%) and $Na_{3.6}V_{1.4}Mn_{0.6}(PO_4)_3$ (77%). Further, to grasp more understanding on the phase immiscibility of the $Na_{3.5}V_{1.5}Mn_{0.5}(PO_4)_3$ sample, temperature dependent *in-situ* XRD measurement were conducted (Figure 3.3). As the temperature is raised from the room temperature to 700 °C, the presence of the two NASICON phases are still observed, which clearly signifies the existence of phase immiscibility even at higher temperatures.

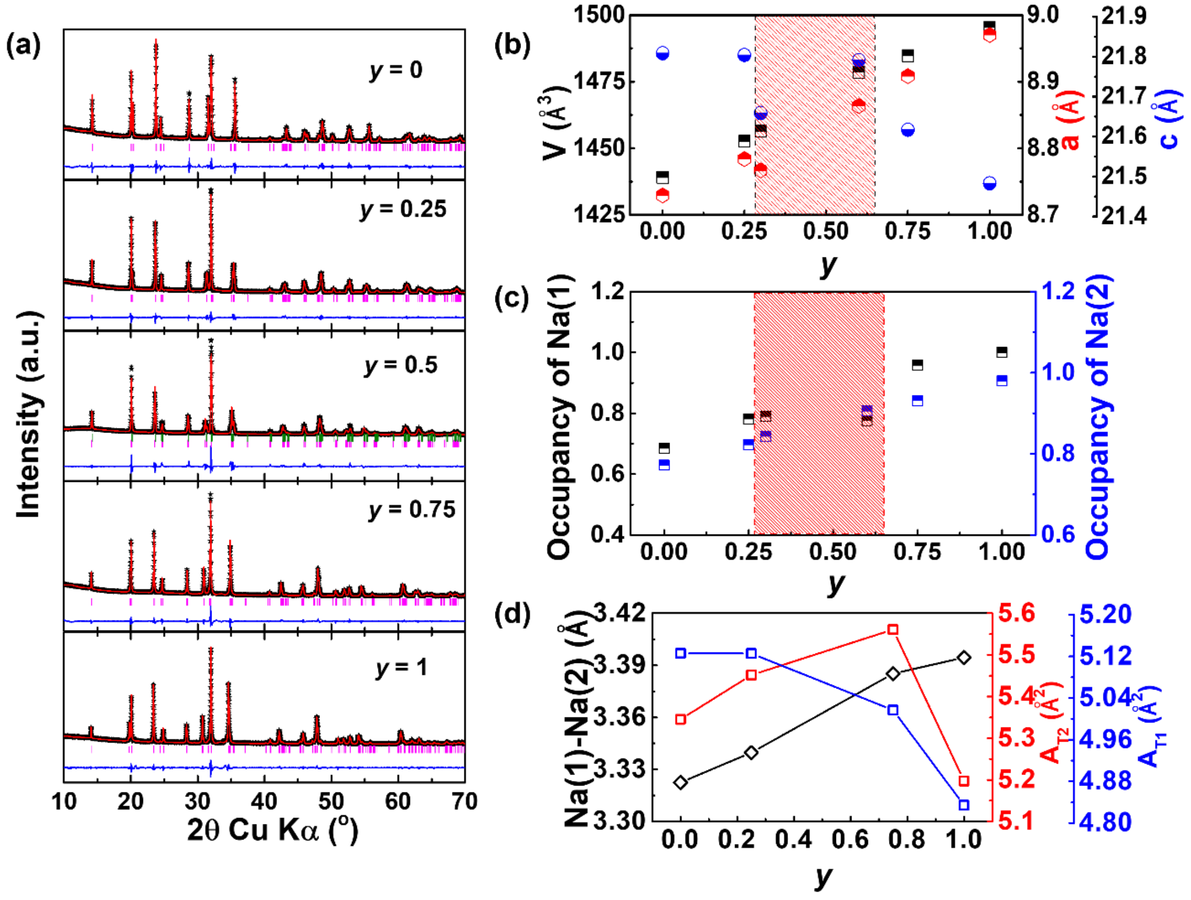

Figure 3.2. (a) Rietveld refinement of the as-synthesized $Na_{3+y}V_{2-y}Mn_y(PO_4)_3$ samples. (b) Cell parameters and unit cell volumes, (c) sodium ion occupancies and (d) Na(1)-Na(2) distances and bottleneck areas (T1 and T2) obtained from Rietveld analysis as the function of *y*. The green shaded areas represent the two-phase region.

To follow the structural evolution of $Na_{3+y}V_{2-y}Mn_y(PO_4)_3$ phases, their corresponding cell parameters and unit cell volumes along with sodium occupancies are plotted against the amount of Mn^{2+} substituted (*y*) (Figure 3.2b and c). As the amount of Mn^{2+} substitution increases, Na(1) and Na(2) sites are progressively filled. Accordingly, an increase in *a*-axis, a decrease in *c*- axis and overall increase in unit cell volume are noticed. The decrease in *c*-parameter could be ascribed to the increase of Na(1) population which is expected to decrease the electrostatic repulsion between two $(V/Mn)O_6$ octahedra.[38] On the other hand, the increase of *a*-parameter could be correlated to the relative increase of $[O_3NaO_3(V/Mn)O_3NaO_3]$ column size (which is due to the replacement of smaller V^{3+} cations ($\boldsymbol{r_{V^{3+}}}$ = 0.64 Å)[39] with larger Mn^{2+} cations ($\boldsymbol{r_{Mn^{2+}}}$ = 0.83 Å)[39] as well as to the increase of Na(2) occupancy. Further, to track down the changes in bottleneck sizes which affect the Na-ion mobility in the NASICON framework, the Na(1)–Na(2) distances and triangular bottleneck areas (T1 and T2 as shown in Figure 3.2d) are plotted against *y* (Figure 3.2d).[35,36] The increase of Na(1)–Na(2) distances upon the increase of Mn^{2+} substitution could be related to the enhanced electrostatic repulsion between the adjacent sodium ions. Despite there is no direct correlation between T2 area and *y*, the $Na_{3.75}V_{1.25}Mn_{0.75}(PO_4)_3$ cathode is found to have the maximum T2 area of 5.55 $Å^2$ in these series of compounds. Interestingly, the T1 areas decrease as *y* increases from 0 to 1 which indicates an increase of activation energy for Na-ion mobility in the NVP framework. It is also worth mentioning that the $Na_4VMn(PO_4)_3$ structure contains the smallest T1 and T2 areas (4.84 and 5.2 $Å^2$, respectively) in these series of compounds.

Table 3.1. Lattice parameters and atomic coordinates of $Na_{3+y}V_{2-y}Mn_y(PO_4)_3$ samples.

	Wyckoff site	**x**	**y**	**z**	**occupancy**	**B_{iso} (Å^2)**
$Na_3V_2(PO_4)_3$ ***Space group $R\bar{3}c$; a* = 8.72942(8) Å & *c* = 21.8182(3) Å** **Chi^2 = 2.37 & R_{wp} = 3.23%**						
Na(1)	6*b*	1/3	2/3	1/6	0.685(2)	6.56(14)
Na(2)	18*e*	2/3	0.9679(6)	1/8	0.772(2)	6.56(14)
V	12*c*	1/3	2/3	0.01846(8)	1	1.02(5)
P	18*e*	-0.0414(3)	1/3	1/8	1	1.89(7)
O1	36*f*	0.1422(3)	0.4974(4)	0.0806(2)	1	1.00(6)
O2	36*f*	0.5457(4)	0.8462(4)	-0.02559(14)	1	1.00(6)
$Na_{3.25}V_{1.75}Mn_{0.25}(PO_4)_3$ ***Space group $R\bar{3}c$; a* = 8.78401(8) Å & *c* = 21.7430(2) Å** **Chi^2 = 3.29 & R_{wp} = 3.49%**						
Na(1)	6*b*	1/3	2/3	1/6	0.781(2)	4.46(10)
Na(2)	18*e*	2/3	0.9695(4)	1/8	0.823(2)	4.46(10)
V/Mn	12*c*	1/3	2/3	0.01837(7)	0.875/0.125	0.43(4)

P	18*e*	-0.0372(2)	1/3	1/8	1	1.62(6)
O1	36*f*	0.1433(3)	0.4987(3)	0.07928(17)	1	0.10(5)
O2	36*f*	0.5446(3)	0.8516(3)	-0.02661(11)	1	0.10(5)
$Na_{3.5}V_{1.5}Mn_{0.5}(PO_4)_3$ **Chi^2 = 5.04 & R_{wp} = 5.94%** **Composed of two phases** **Phase 1 (77 w%): $Na_{3.6}V_{1.4}Mn_{0.6}(PO_4)_3$,** ***Space group $R\bar{3}c$*; a = 8.86348(6) Å & c = 21.6359(7) Å**						
Na(1)	6*b*	1/3	2/3	1/6	0.776(8)	2.16(14)
Na(2)	18*e*	2/3	0.9752(11)	1/8	0.906(8)	2.16(11)
V/Mn	12*c*	1/3	2/3	0.01851(7)	0.7/0.3	0.32(4)
P	18*e*	-0.0408(9)	1/3	1/8	1	0.72(9)
O1	36*f*	0.14193(8)	0.49765(8)	0.07762(3)	1	0.28(3)
O2	36*f*	0.54047(2)	0.8448(2)	-0.02643(14)	1	0.28(3)
Phase 2 (23 w%): $Na_{3.3}V_{1.7}Mn_{0.3}(PO_4)_3$ ***Space group $R\bar{3}c$*; a = 8.7669(7) Å & c = 21.7295(3) Å**						
Na(1)	6b	1/3	2/3	1/6	0.790(3)	1.35(14)
Na(2)	18e	2/3	0.9699(6)	1/8	0.843(3)	1.35(14)

V/MN	12c	1/3	2/3	0.01849(10)	0.85/0.15	0.18(5)
P	18e	-0.0349(4)	1/3	1/8	1	0.81(2)
O1	36f	0.1356(5)	0.4946(5)	0.0761(2)	1	0.47(4)
O2	36f	0.5482(5)	0.8490(5)	-0.02542(17)	1	0.47(4)
$Na_{3.75}V_{1.25}Mn_{0.75}(PO_4)_3$ **_Space group_ $R\bar{3}c$; _a_ = 8.90837(7) Å & _c_ = 21.6140(2) Å** **Chi^2 = 1.47 & R_{wp} = 2.90%**						
Na(1)	6*b*	1/3	2/3	1/6	0.958(2)	1.19(10)
Na(2)	18*e*	2/3	0.9727(5)	1/8	0.931(2)	1.19(10)
V/Mn	12*c*	1/3	2/3	0.01794(9)	0.625/0.375	0.24(5)
P	18*e*	-0.0379(3)	1/3	1/8	1	0.83(8)
O1	36*f*	0.1442(4)	0.4968(4)	0.0799(2)	1	0.39(7)
O2	36*f*	0.5474(5)	0.8579(4)	-0.02649(16)	1	0.39(7)
$Na_4VMn(PO_4)_3$ **_Space group_ $R\bar{3}c$; _a_ = 8.97022(6) Å & _c_ = 21.4719(2) Å** **Chi^2 = 3.64 & R_{wp} = 3.31%**						
Na(1)	6*b*	1/3	2/3	1/6	1	1.19(7)
Na(2)	18*e*	2/3	0.9742(3)	1/8	0.98	1.19(7)

V/Mn	12*c*	1/3	2/3	0.01751(8)	0.5/0.5	0.54(4)
P	18*e*	-0.0341	1/3	1/8	1	0.88(7)
O1	36*f*	0.1458(3)	0.4956(3)	0.08217(18)	1	0.25(6)
O2	36*f*	0.5464(4)	0.8650(3)	-0.02585(12)	1	0.25(6)

Table 3.2: Selected bond distances for $Na_{3+y}V_{2-y}Mn_y(PO_4)_3$ samples

Compound	(V/Mn)−O (Å)	Na (1)−O (Å)	Na (2)−O (Å)
$Na_3V_2(PO_4)_3$	2.0296(16) × 6	2.4539(15)× 6	2.4607(28)× 2 2.3703(35)× 2 2.8169(25)× 2 2.5955(39)× 2
$Na_{3.25}V_{1.75}Mn_{0.25}(PO_4)_3$	2.0320(18) × 6	2.5598(18)× 6	2.5068(60)× 2 2.3835(36)× 2 2.8179(54)× 2 2.5871(38)× 2
$Na_{3.75}V_{1.25}Mn_{0.25}(PO_4)_3$	2.0667(13) × 6	2.4680(12)× 6	2.5235(33)× 2 2.4540(25)× 2 2.8684(35)× 2

			2.5933(26)× 2
$Na_4VMn(PO_4)_3$	2.0928(12) × 6	2.4530(12)× 6	2.5256(33)× 2 2.4841(22)× 2 2.9182(30)× 2 2.5743(25)× 2

Further, to get more insights about the oxidation states and changes in the local structure, X-ray absorption spectroscopy (XAS) experiments were performed on the as-synthesized $Na_{3+y}V_{2-y}Mn_y(PO_4)_3$ ($0 \leq y \leq 1$) samples. No significant changes are noticed in the energy positions at the V and Mn K-edges for all the samples (Figure 3.4a and b), thus confirming the oxidation states of vanadium and manganese as +3 and +2, respectively. Figure 3.4c and d shows the magnitude plots of Fourier-transformed extended X-ray adsorption fine structure (FT-EXAFS) for V and Mn K-edges. The first prominent peak at ~1.5 Å can be assigned to the first (V/Mn)-O coordination shell and the next 1-2 peaks extending to ~3.2 Å belong to (V/Mn)-P and (V/Mn)-Na outer shells. Note that FT-EXAFS spectra are not phase corrected, thus the observed values are lower than the actual bond lengths. As amount of the Mn^{2+} substitution is increased, the peak positions of (V/Mn)-O shell remain same for all the samples. Interestingly, the distances of V-P and V-Na outer shells are found to be slightly increased for $Na_{3.75}V_{1.25}Mn_{0.75}(PO_4)_3$ cathode compared to the other samples, which might influence the sodium ion mobility in the NASICON framework.

The morphology of the as-synthesized $Na_{3+y}V_{2-y}Mn_y(PO_4)_3$ ($0 \leq y \leq 1$) samples were studied using SEM technique (Figure 3.5). In contrast to the $Na_3V_2(PO_4)_3$ sample which consists of nanoscale (~500 nm) primary particles, the y = 0.25 substituted sample shows the presence of micron size particles (~> 2.0 µm). On the other hand, the $Na_{3.75}V_{1.25}Mn_{0.75}(PO_4)_3$ and $Na_4VMn(PO_4)_3$ samples contain large chunks, consisting of micron (~> 1.0 µm) and sub-micron (~> 500 nm) size primary particles, respectively. Interestingly, the y = 0.5 sample presents inhomogeneous particles, ranging from nano size (~< 500 nm) to micron size large chunks (~< 2 µm), thus confirming decomposition of the NASICON phases as observed in our XRD experiments.

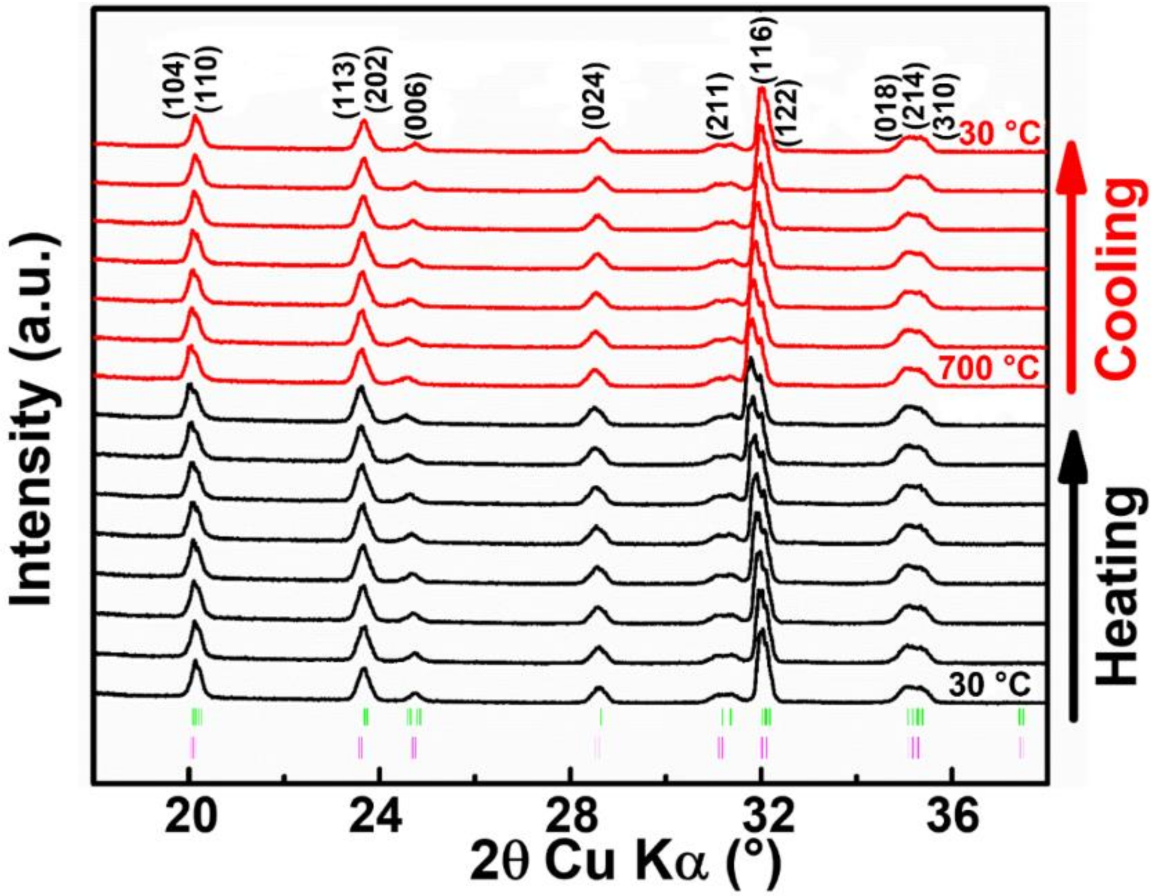

Figure 3.3. Temperature dependent *in-situ* XRD of $Na_{3.5}V_{1.5}Mn_{0.5}(PO_4)_3$. Green and pink bars correspond to the $Na_{3.3}V_{1.7}Mn_{0.3}(PO_4)_3$ and $Na_{3.6}V_{1.5}Mn_{0.6}(PO_4)_3$ phases, respectively.

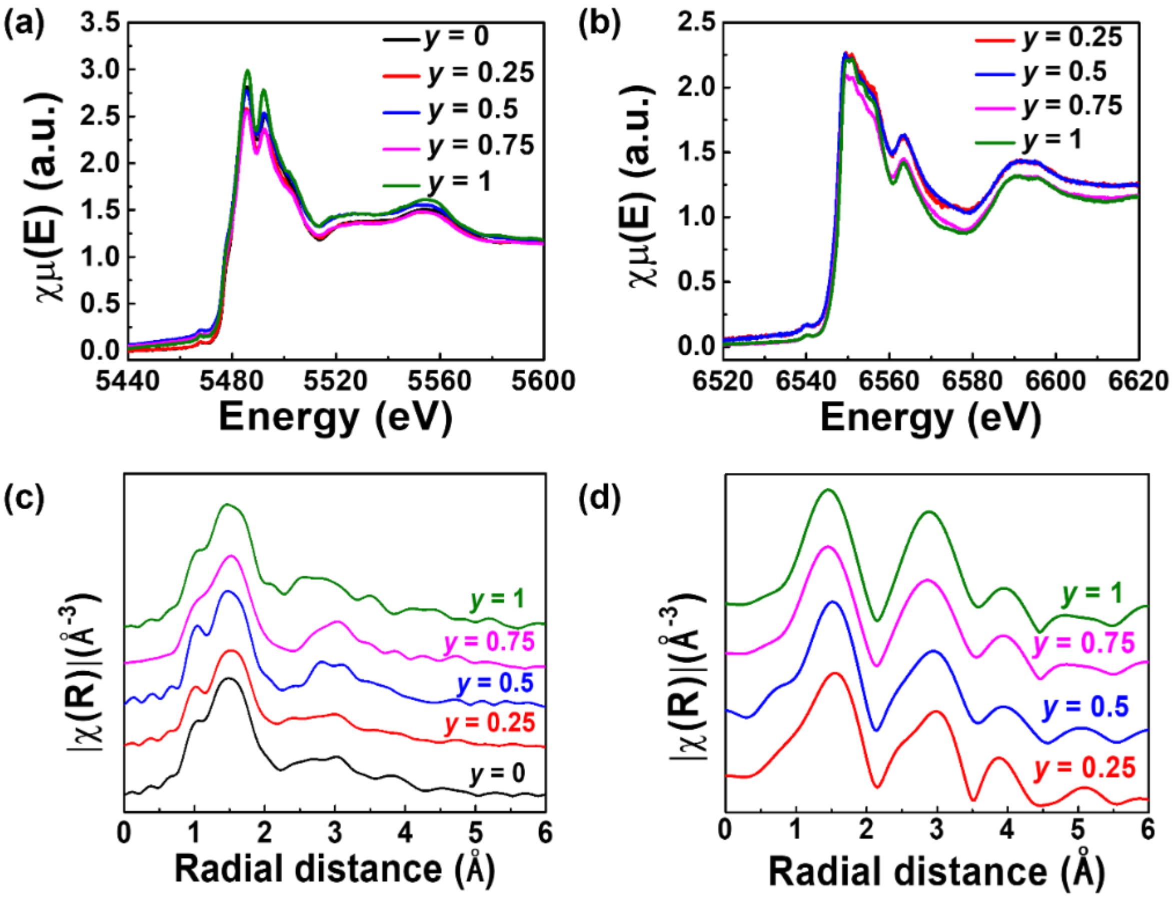

Figure 3.4. Normalized absorption spectra of the as-synthesized $Na_{3+y}V_{2-y}Mn_y(PO_4)_3$ samples at (a) V-K edge and (b) Mn-K edge. Fourier-transform EXAFS spectra of the as-synthesized $Na_{3+y}V_{2-y}Mn_y(PO_4)_3$ samples at (c) V-K edge and (d) Mn-K edge.

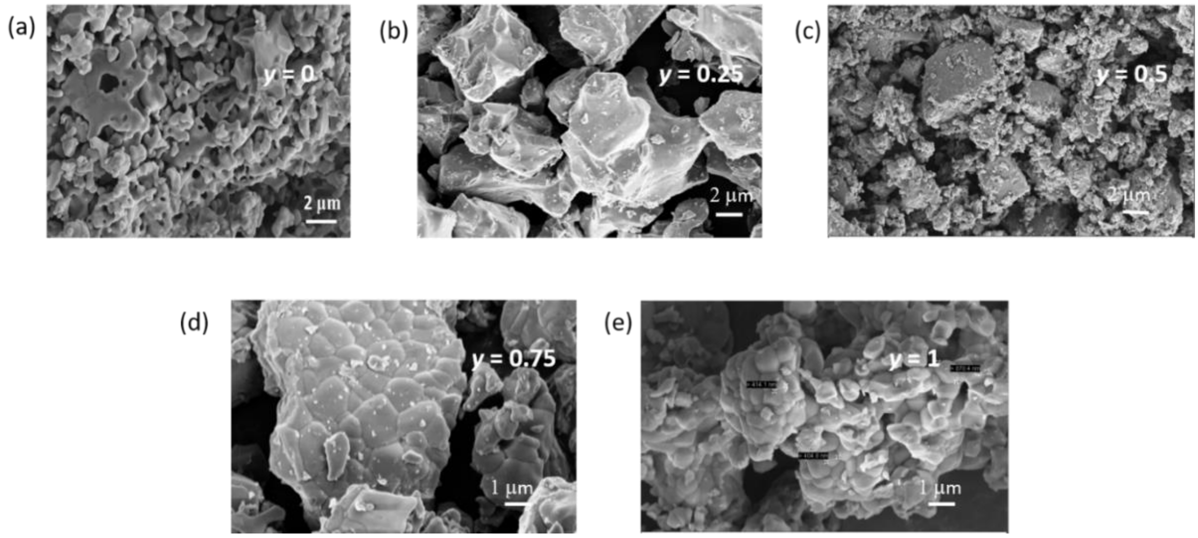

Figure 3.5. SEM image of $Na_{3+y}V_{2-y}Mn_y(PO_4)_3$ cathodes. y = (a) 0, (b) 0.25, (c) 0.5, (d) 0.75 and (e) 1.

3.3.2. Electrochemical (de)intercalation properties of $Na_{3+y}V_{2-y}Mn_y(PO_4)_3$ cathodes

The electrochemical behaviors of $Na_{3+y}V_{2-y}Mn_y(PO_4)_3$ cathodes were studied by galvanostatic cycling at C/10 rate in between 3.8-2.75 V *vs.* Na^+/Na^0 and the corresponding voltage profiles are shown in Figure 3.6a. During the first cycle, the $Na_3V_2(PO_4)_3$ electrode shows an intercalation plateau at an average voltage of *ca.* ~3.37 V *vs.* Na^+/Na^0 due to the operation of V^{4+}/V^{3+} redox couple. The corresponding electrochemical exchange is found to be *ca.* ~1.73 and 1.5 moles of sodium ions per formula unit (*pfu*) of the cathode on the charge and discharge, respectively. The limited amount of sodium exchange of the NVP cathode in comparison with the earlier reports could be due to the presence of micron sized particles and its limited electronic conductivity.[9,13] As the amount of Mn^{2+} substitution is increased from $y = 0$ to 0.5 in the NVP structure, the voltage profiles of the corresponding cathodes have become slightly sloppier, whilst the amount reversible sodium (de)intercalation is decreased to *ca.* ~1.2 moles *pfu*. Surprisingly, when the substitution of Mn^{2+} has reached to $y = 0.75$ in the NVP structure, the amount of reversible sodium ion exchange is increased to *ca.* ~1.9 moles *pfu,* with an average intercalation voltage of 3.46 V *vs.* Na^+/Na^0. Finally, the end member $Na_4VMn(PO_4)_3$ cathode shows two step voltage profiles with the intercalation voltages of *ca.* ~3.4 and 3.55 V *vs.* Na^+/Na^0 and the corresponding redox activities could be ascribed to the operation of V^{4+}/V^{3+} and Mn^{3+}/Mn^{2+} redox couples, in accordance with the previous reports.[31] The corresponding reversible electrochemical exchange is found to be *ca.* ~1.8 moles of sodium ions *pfu*. To better understand the underlying redox process in the above-mentioned cathodes, their corresponding dQ/dV plots from the first cycle are shown in the Figure 3.6c. Whilst, the $Na_3V_2(PO_4)_3$ cathode shows a sharp voltage features at *ca.* ~3.35 V, the $Na_4VMn(PO_4)_3$ cathode exhibits two distinct voltage features at *ca*. ~3.4 and 3.6 V *vs*. Na^+/Na^0, in accordance with the earlier reports.[9,31] Further, the derivative curves of the $y = 0.25$ and 0.5

samples show broader voltage features and their average intercalation voltages have slightly increased (~10 mV), which could be attributed to the operation of V^{4+}/V^{3+} redox couple. More interestingly, the $Na_{3.75}V_{1.25}Mn_{0.75}(PO_4)_3$ cathode shows two superimposed yet discernable redox features at *ca*. ~3.44 and 3.52 V *vs*. Na^+/Na^0, and 3.3 and 3.48 V *vs*. Na^+/Na^0 on oxidation and reduction, respectively. These voltage features could be tentatively ascribed to the activities of V^{4+}/V^{3+} and Mn^{3+}/Mn^{2+} redox couples, which will be confirmed by XAS analysis in the following section.

Further to see the possibility of exchanging more number of Na-ions, we have increased the upper cut-off voltage to 4.2 V *vs.* Na^+/Na^0 (Figure 3.6b and d). Despite the voltage and length of the (de)intercalation plateau (at 3.37 V *vs.* Na^+/Na^0) has remained same for the $Na_3V_2(PO_4)_3$ cathode, additional charge and irreversible capacities are noticed, which could be due to the electrolyte degradation. Further, the $y = 0.25$ and 0.5 substituted samples exhibit an additional voltage feature at *ca.* ~3.85 V *vs.* Na^+/Na^0 along with the voltage plateau at 3.37 V *vs.* Na^+/Na^0, which could be better viewed from the zoomed view of their corresponding dQ/dV curves as shown in the Figure 3.6e. The corresponding high voltage redox activity could be ascribed to the operation of V^{5+}/V^{4+} couple, as reported earlier for other cation doped NVP structures.[24,25,27] Correspondingly, the reversible electrochemical exchange has also increased, from 1.2 moles of sodium ions *pfu* as in the case of the lower cut-off voltage cycling, to *ca.* ~1.35 moles of sodium ions *pfu*. Moreover, when the $Na_{3.75}V_{1.25}Mn_{0.75}(PO_4)_3$ cathode is charged to 4.2 V *vs.* Na^+/Na^0, the voltage profile presents an additional sloppier curve above 3.6 V *vs.* Na^+/Na^0 along with the previously mentioned voltage feature at 3.46 V *vs.* Na^+/Na^0. Accordingly, the electrochemical sodium (de)intercalation is increased to *ca.* ~2.5 moles *pfu*. On the subsequent discharge, the voltage profile has become sloppier with an average voltage of *ca.* ~3.38 V *vs.* Na^+/Na^0 and an intercalation capacity of *ca.* ~1.85 moles of sodium ions *pfu*.

An amount of 0.65 moles of sodium ion *pfu* is lost during the first cycle. Similar trends in the voltage profiles are observed for the $Na_4VMn(PO_4)_3$ cathode, when it is charged to 4.2 V *vs.* Na^+/Na^0 with the electrochemical exchanges of *ca.* ~2.29 and 1.6 moles of sodium ions *pfu* during the first charge and discharge, respectively.[33,34] The pronounced changes in the voltage profile of the last two cathodes can be better viewed in their corresponding dQ/dV curves (Figure 3.6d and e). Altogether, it is observed that the introduction of Mn^{2+} into the NVP cathodes increases their average intercalation voltages compared to the unsubstituted cathode through the activation of V^{5+}/V^{4+} and $Mn^{4+}/Mn^{3+}/Mn^{2+}$ redox couples at higher voltages.

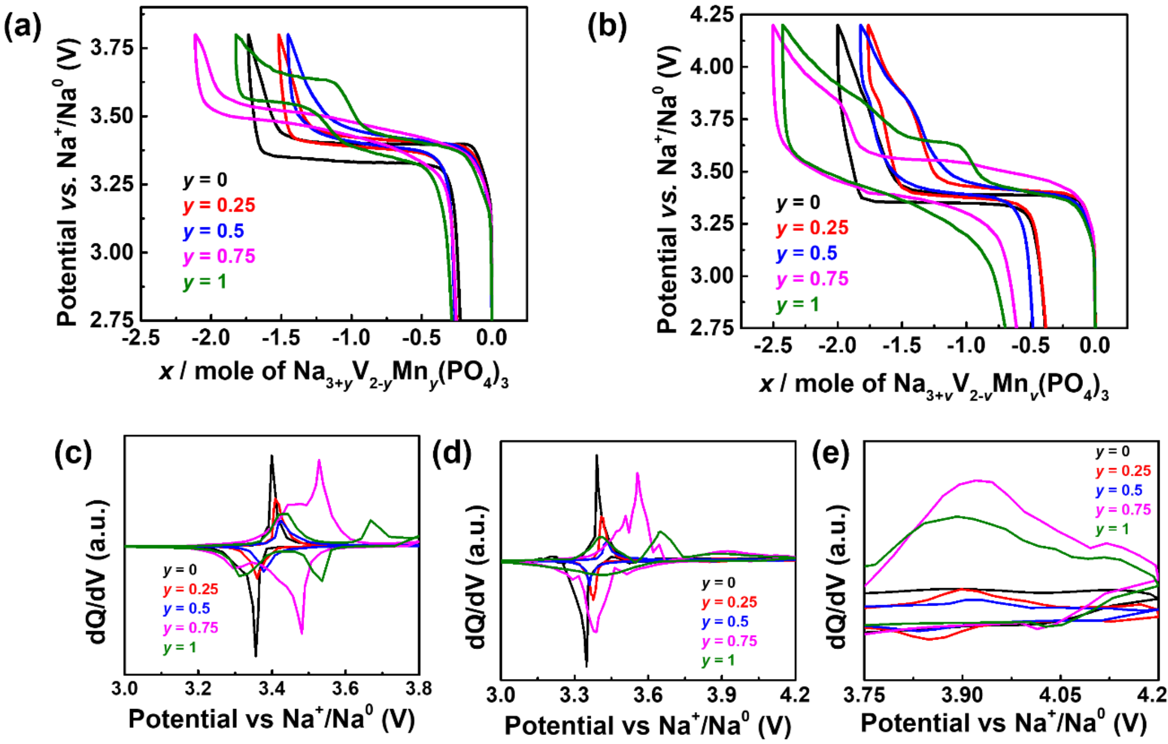

Figure 3.6. The potential *vs*. composition (x) of $Na_{3+y}V_{2-y}Mn_y(PO_4)_3$ cathodes (a) & (b) and their corresponding derivative plots (c) & (d) in the voltage window of 3.8-2.75 V and 4.2-2.75 V *vs*. Na^+/Na^0, respectively. (e) A magnified view of figure d.

3.3.3. *Ex-situ* XRD and XAS studies on $Na_{3+y}V_{2-y}Mn_y(PO_4)_3$ cathodes

To shed more insights on the structural evolution and the corresponding redox processes of $Na_{3+y}V_{2-y}Mn_y(PO_4)_3$ cathodes, two representative samples, i.e., $y = 0.25$ and 0.75, from the series are further subjected for *ex-situ* XRD and XAS studies. Note that the detailed studies on the (de)intercalation mechanism of the end members were previously reported.[9,33,34,40,41] The *ex-situ* XRD patterns of $Na_{3.25}V_{1.75}Mn_{0.25}(PO_4)_3$ cathode with different state of charge are displayed in Figure 3.7a and d and the corresponding refined lattice parameters are shown in Table 3.3. The electrodes harvested at 3.8 and 4.2 V *vs.* Na^+/Na^0 exhibit a new set of reflections in comparison with the pristine electrode, which could be fully indexed with $R\bar{3}c$ space group. The refinement results show a decrease of *a*- and *c*- lattice parameters as well as the unit cell volume and these results are in agreement with the previous studies involving other cation doping.[27] Further, when the electrodes were discharged back to 2.75 V *vs.* Na^+/Na^0, the original reflections belonging to the pristine electrode are restored. The normalized absorption spectra of $Na_{3.25}V_{1.75}Mn_{0.25}(PO_4)_3$ cathode at the V and Mn K-edges with different state of charge are shown in the Figure 3.7b and e, respectively. The V K-edge continuously shifts towards higher energy values during charging to 3.8 V/4.2 V *vs.* Na^+/Na^0 and the intensity of the pre-edge peaks also increase, thus indicating the progressive oxidation of V^{3+} to V^{4+} and V^{5+}. Interestingly, no significant changes in the energy position of the Mn K-edge are noticed, which implies the electrochemical inactivity of Mn^{2+} cations. The slight change in the profile can be ascribed to the local structural changes during charging process. When the cathodes are discharged back to 2.75 V *vs.* Na^+/Na^0, the spectrum nicely recovers to the same energy and profile as the pristine sample. The comparison between $\chi(k)$ signals of *ex-situ* $Na_{3.25}V_{1.75}Mn_{0.25}(PO_4)$ cathodes at different state of charge are shown in Figure 3.7c and f. The reduction of the amplitude of EXAFS oscillations along with overall damping is observed for the cathodes charged to 3.8/4.2 V *vs.* Na^+/Na^0. The chemical shift of the EXAFS signal obtained for the cathode at 2.75 V *vs.* Na^+/Na^0 matches with pristine sample. Overall, the *ex-situ* XRD and XAS analysis confirm the full reversibility of the redox processes that occur at both cycling windows.

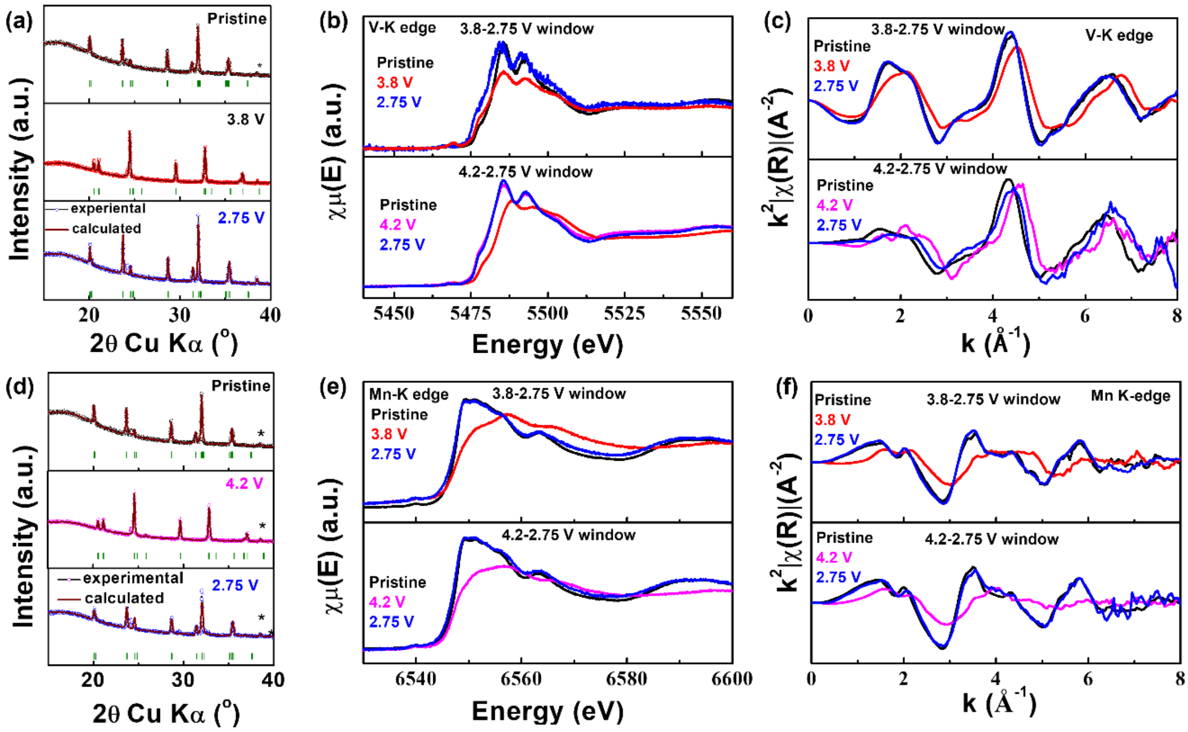

Figure 3.7. *Ex-situ* XRD patterns of the $Na_{3.25}V_{1.75}Mn_{0.25}(PO_4)_3$ cathode at various state of charges in the voltage window of a) 3.8-2.75 V and d) 4.2-2.75 V *vs.* Na^+/Na^0 (calculated fit – brown solid line, Bragg peak- green). Normalized absorption spectra (b & e) and k^2-wieghted χ(k) signals (c & f) collected at V-Kedge and Mn-K edges, respectively for $Na_{3.25}V_{1.75}Mn_{0.25}(PO_4)_3$ cathode.

Table 3.3. Refined cell parameters and unit cell volumes of *ex-situ* $Na_{3+y}V_{2-y}Mn_y(PO_4)_3$ (y = 0.25 and 0.75) cathodes

$Na_{3.25}V_{1.75}Mn_{0.25}(PO_4)_3$			
	a (Å)	*c* (Å)	V (Å^3)
Pristine	8.7900(5)	21.7448(16)	1454.99(16)
3.8 V	8.4312(4)	21.4989(15)	1323.52(13)
3.8-2.75 V	8.76102(3)	21.7378(11)	1444.96(9)

4.2 V	8.4060(5)	21.491(2)	1315.11(18)
4.2-2.75 V	8.7699(14)	21.728(4)	1447.3(4)
$Na_{3.75}V_{1.25}Mn_{0.75}(PO_4)_3$			
Pristine	8.8938(4)	21.5821(12)	1478.42(12)
3.5 V	8.8015(3)	21.506(3)	1442.79(19)
3.8 V	8.5129(4)	21.5721(16)	1353.88(14)
3.8-3.4 V	8.5327(6)	21.5792(17)	1360.63(17)
3.8-2.75 V	8.8865(2)	21.5921(10)	1476.69(9)
4.2 V	8.4642(5)	21.675(3)	1344.8(2)
4.2-2.75 V	8.8757(3)	21.616(4)	1474.7(3)

Let us turn our attention towards the *ex-situ* XRD experiments of $Na_{3.75}V_{1.25}Mn_{0.75}(PO_4)$ cathode (Figure 3.8a and d). As the electrode is charged to 3.5 V *vs.* Na^+/Na^0, the removal of 1.25 moles of sodium ions *pfu* leads to the formation of $Na_{2.50}V_{1.25}Mn_{0.75}(PO_4)$. This intermediate phase presents a similar set of peaks as the pristine electrode, but they are shifted towards higher 2θ angle. Further upon charging to 3.8 V *vs.* Na^+/Na^0, a new NASICON phase (with $R\overline{3}c$ space group) appears with a composition of $Na_{1.75}V_{1.25}Mn_{0.75}(PO_4)$ (i.e., after the removal of additional 0.75 moles of sodium ions *pfu*). The refinements on the corresponding XRD patterns have shown a strong and slight decrease of *a* and *c*-parameters, respectively (Table 3.3), implying the progressive removal of Na-ions from Na(2) while the occupancy of Na(1) remains unchanged.[33,34] The change in the unit cell volume (from $Na_{3.75}V_{1.25}Mn_{0.75}(PO_4)$ to $Na_{1.75}V_{1.25}Mn_{0.75}(PO_4)$) is found to be 8.4% and is comparable with the volume changes reported for the end members ($Na_3V_2(PO_4)_3$) & $Na_4VMn(PO_4)_3$).[9,33,34,40,41] After the discharge to 2.75 V *vs.* Na^+/Na^0, the structure of the electrode is fully restored which demonstrated the high reversibility of the electrochemical reactions when the upper cut-off voltage is set to 3.8 V *vs.* Na^+/Na^0. To seek further details on the contribution of vanadium and manganese cations during this redox process, *ex-situ* XAS are collected on $Na_{3.75}V_{1.25}Mn_{0.75}(PO_4)$ cathodes with different state of charges and the normalized absorption spectra at V and Mn K-edges are shown in Figure 3.8b and e, respectively. When cycled in the voltage window of 3.8-2.75 V *vs*. Na^+/Na^0, both edges are shifted towards higher energies during charging followed by moving back to the original energy positions upon the subsequent discharge. These observations indicate the activities of V^{4+}/V^{3+} and Mn^{3+}/Mn^{2+} couples during the cycling. Further, the $\chi(k)$ signals at V-and Mn K edges have shown similar trends in the chemical shifts as in the case of $Na_{3.25}V_{1.75}Mn_{0.25}(PO_4)_3$ cathode (Figure 3.8c and f). Thus, the combined *ex-situ* XRD and XAS analysis have confirmed the high reversibility of sodium (de)intercalation process when the cycling window is set to 3.8-2.75 V *vs.* Na^+/Na^0.

Further, as the charging window is extended to 4.2 V *vs.* Na^+/Na^0, another 0.5 moles of Na-ions *pfu* could be removed which leads to the formation of $Na_{1.25}V_{1.25}Mn_{0.75}(PO_4)_3$ phase. Despite the corresponding XRD pattern can be indexed with $R\bar{3}c$ space group, the refined lattice parameters show anisotropic changes (i.e., decrease of *a*- and increase *c*-parameters, respectively), which indicates the possible removal of Na-ions from Na(1) and Na(2) sites. Upon subsequent discharge to 2.75 V *vs.* Na^+/Na^0, a new phase is formed with a composition of $Na_{3.1}V_{1.25}Mn_{0.75}(PO_4)$, whose lattice parameters are quite closer to the pristine electrode despite the significant irreversible capacity as mentioned earlier. Similar trends about the structural evolution upon charging and discharging were previously reported for the $Na_4VMn(PO_4)_3$ cathode.[33,34] The normalized absorption spectra at V and Mn K-edges of the $Na_{3.75}V_{1.25}Mn_{0.75}(PO_4)$ cathodes with different state of charge are shown in the Figure 3.8b and e. Upon charging to 4.2 V *vs.* Na^+/Na^0, further shifts towards higher energies are observed in the XAS spectra which indicates the formation of mixed V^{5+}/V^{4+} and Mn^{4+}/Mn^{3+} redox states. Interestingly, the appearance and amplitude associated with the 2nd shell (V/Mn)-Na of the $\chi(k)$ signals of the discharged cathode at both V and Mn K-edges do not reconcile with the pristine cathode (Figure 3.8c and f), thus confirming the irreversible losses occurred during the additional Na-ion extraction, which corroborates our *ex-situ* XRD findings.

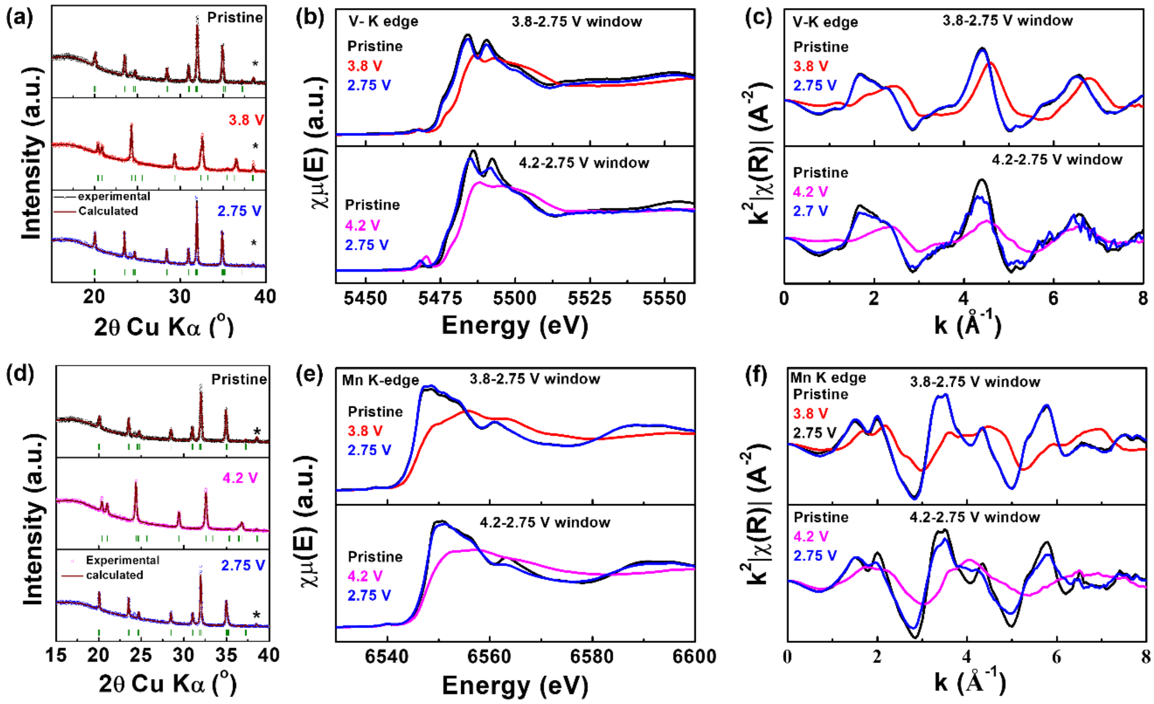

Figure 3.8. *Ex-situ* XRD patterns of the $Na_{3.75}V_{1.25}Mn_{0.75}(PO_4)_3$ cathode at various state of charges in the voltage windows of a) 3.8-2.75 V and d) 4.2-2.75 V *vs.* Na^+/Na^0(calculated fit - brown solid line, Bragg peak - green). Normalized absorption spectra (b & e) and k^2-weighted $\chi(k)$ signals (c & f) collected at V-Kedge and Mn-K edges, respectively for $Na_{3.75}V_{1.25}Mn_{0.75}(PO_4)_3$ cathode.

3.3.4. Theoretical approach

Based on the aforementioned discussions, it is clear that the Mn^{2+} is completely soluble in the NVP structure except in the case of $y = 0.5$, where the miscibility gap appears. The substituted Mn^{2+} is electrochemical inactive in the cathodes with lower concentration ($y \leq 0.5$). Besides, $Na_{3.75}V_{1.25}Mn_{0.75}(PO_4)_3$ not only shows high discharge capacities, but also high rate capabilities and low polarization amongst other phases. To grasp more insights into these experimental findings, DFT calculations were performed to look at the relative stabilities and the corresponding electronic structures of the $Na_{3+y}V_{2-y}Mn_y(PO_4)_3$ phases (Figure 3.9). The relative stabilization energies of the $Na_{3+y}V_{2-y}Mn_y(PO_4)_3$ systems have been ascertained from their formation energies with respect to varying Mn content(y) and V content (2-y)[42] :

$$\Delta E_f = E[Na_{(3+y)}V_{(2-y)}Mn_y(PO_4)_3] - (1-y)E[V_{(2-y)}Mn_y(PO_4)_3] - yE[Na_4VMn(PO_4)_3] \quad (1)$$

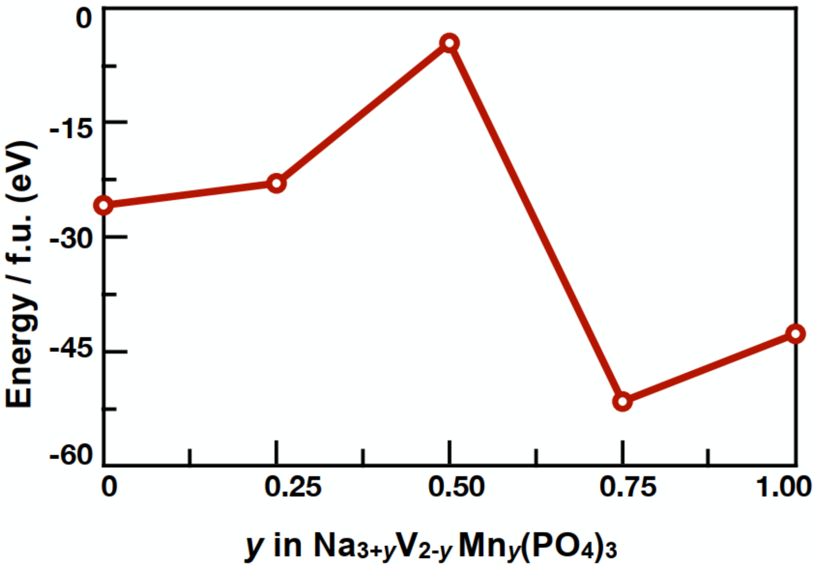

Figure 3.9. Formation energy *vs*. composition (y) of $Na_{3+y}V_{2-y}Mn_y(PO_4)_3$ cathodes.

It is important to mention here that all energies are calculated per formula unit of the species. The trend in the values of formation energies does not follow a typical convex hull in the compositional phase diagram; a break appears at $y = 0.50$, as indicated by a sharp shoot-up in the formation energy value (Figure 3.9). This suggests the possibility of a phase segregation, at $y = 0.50$, which was earlier confirmed from our experimental observations. We observe the irregular (V/Mn)-O bond lengths in the highly distorted octahedra, which makes it relatively unstable from the other compositions. Surprisingly, the minima in the formation energy *vs.* composition plot appears at $y = 0.75$ configuration, which indicates that $Na_{3.75}V_{1.75}Mn_{0.75}(PO_4)_3$ has a lower energy ground state compared to the other members of this series.

To better understand the participation of the redox couples of vanadium and manganese cations during the electrochemical sodium (de)intercalation, we have analyzed the projected Density of States (pDOS) of the $Na_{3+y}V_{2-y}Mn_y(PO_4)_3$ cathodes at various compositions (Figure 3.10). The activity of the transition metal (TM) cations can be ascribed to the electronic distribution of the 3d orbitals of the TM atom near the Fermi Level and the crystal field environment of the TM atoms. The 3d orbitals of V have a generous distribution near the Fermi Level in the $Na_3V_2(PO_4)_3$ system, thereby confirming that the redox activity of V is totally contributed by its valence 3d electrons. It is naturally expected that for the Mn-substituted systems the electrons of Mn 3d orbitals would participate in the Mn redox transitions. However, for the systems with compositions $y = 0.25$, the electronic density of the Mn 3d orbitals is almost negligible, thus rendering electrochemically inactive Mn center. For the $y = 0.75$ case, both V and Mn 3d electron densities are significant at the Fermi level, with the Mn density being slightly excess of the V density. This suggests that both V and Mn centers viably undergo redox reactions. Here the contribution from Mn will be more than that from V, due to greater number of valence electrons in the former and the gap between Fermi level and conduction states also proves that the voltage will be higher for this system, compared to the $y = 0.25$ composition. (Figure 3.10). At $y = 1.00$, Mn and V electron densities are fairly high and almost equal, but lesser than that of *y* = 0.75 cathode, which accounts for the reduced redox activity. Altogether, the pDOS observations are in agreement with our electrochemical studies, thus signifying the importance of modulating the V- and Mn-redox centers to achieve higher electrochemical activity.

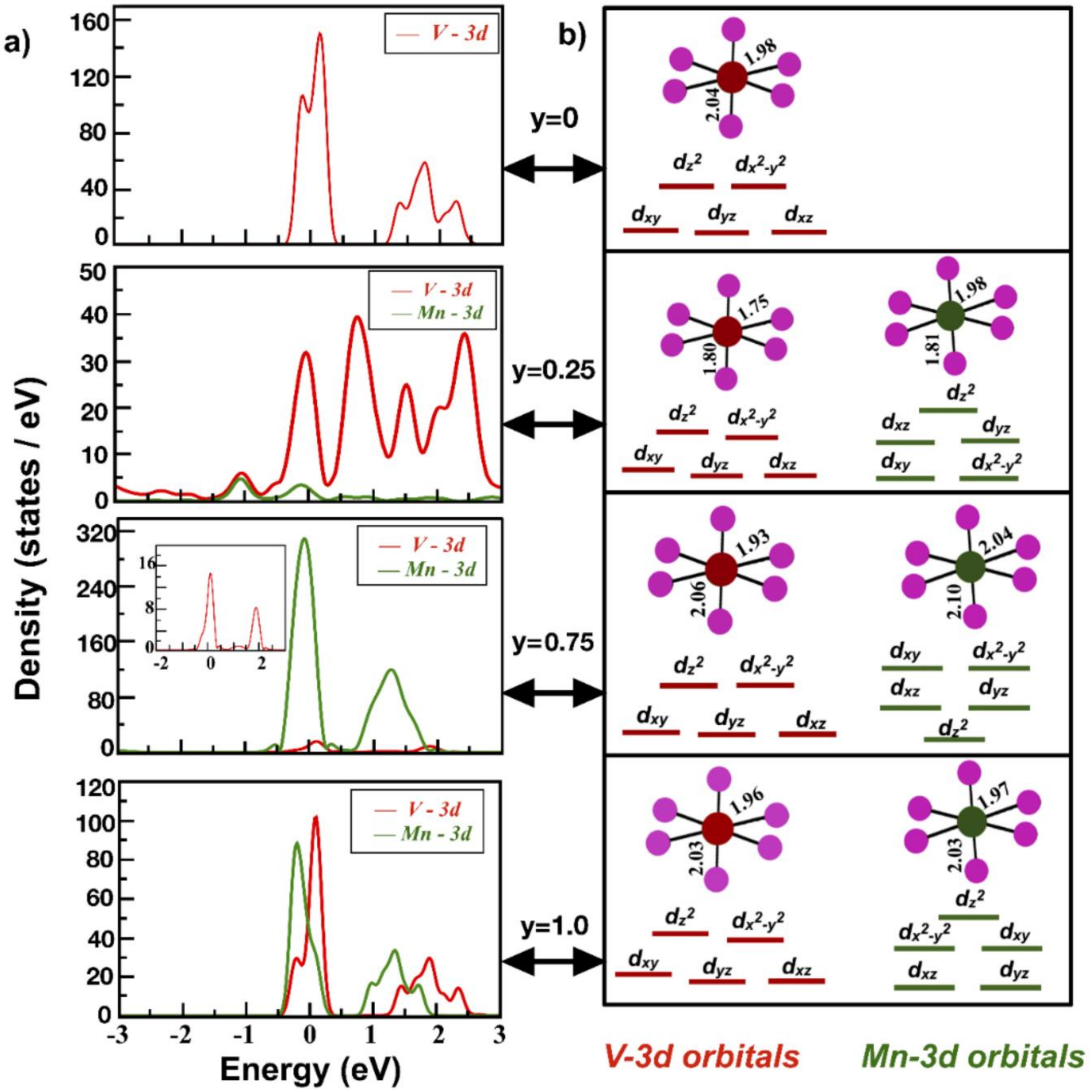

Figure 3.10. (a) Projected Density of States of $Na_{3+y}V_{2-y}Mn_y(PO_4)_3$ cathode. (b) Schematic representation of d-orbital splitting of Mn and V species in the of $Na_{3+y}V_{2-y}Mn_y(PO_4)_3$ framework along with (V/Mn)-O bond distances (Å) obtained from AIMD simulations.

A detailed study of the pDOS of the 3d orbitals of V and Mn reveals quite a few interesting observations in terms of the d-orbital behavior in the TM's (figure 3.10). The electronic density of states describes the orbital occupancy in the valence states, Fermi level and conduction states. We have also carried out AIMD simulations to obtain optimized geometry of $Na_{3+y}V_{2-y}Mn_yPO_4)_3$ systems at room temperature. Optimized geometries obtained from DFT calculations have corroborated with those obtained from AIMD simulations. From these optimized geometries and different energies, we infer the 3d orbital distribution and hence, the crystal field splitting. For all the compositions, vanadium coordination does not undergo any conspicuous change and the 3d orbital splitting is commensurate with an octahedral crystal field. The scenario is much more complex in case of Mn. In case of $y = 0.25$, Mn has highly distorted octahedra, which is manifested in the reduction of the Mn-O bond lengths along the z-direction through the Mn $3d_{z^2}$ orbitals. For $y = 0.75$ and 1, the Mn-O bonds form nearly octahedral symmetry and in both cases Mn centers contribute to the redox activity of the systems. From these observations, it may be concluded that the geometry drives the d-orbital splitting and thereby the redox activity.

3.3.5. Cycling performances of $Na_{3+y}V_{2-y}Mn_y(PO_4)_3$ cathodes

The cycling performances of the $Na_{3+y}V_{2-y}Mn_y(PO_4)_3$ cathodes were assessed at C/10 rate in two voltage windows (Figure 3.11a, c and e). To better understand the influence of Mn-substitution on their cycle life, the plots of normalized capacity *vs*. cycle number are also shown in Figure 3.11b, d and f. In the window of 4.2-2.75 V *vs.* Na^{+}/Na^{0}, all the Mn-substituted samples display slightly improved initial capacities when compared to their low voltage window cycling. We recall our previous observations that the redox activities of V^{5+}/V^{4+} and Mn^{4+}/Mn^{3+} couples in $y = 0.75$ and 1 contribute to their additional capacities, whereas the V^{5+}/V^{4+} couple is solely responsible for such enhancements in the $y = 0.25$ and 0.5 cathodes.

Further, the $y \leq 0.5$ cathodes show similar trends on the capacity retentions (~ 80 % of their initial capacities are retained at the end of 50th cycle). However, $y = 0.75$ and 1 cathodes undergo rapid capacity fade (i.e., only 61 and 30 % of their initial values are retained at the end of 50th cycle). Although, such rapid decay could be ascribed to the structural changes occurring at higher voltages as previously discussed,[33,34] it seems that the $y = 0.75$ cathode exhibit slower degradation in comparison with $y = 1$ sample.

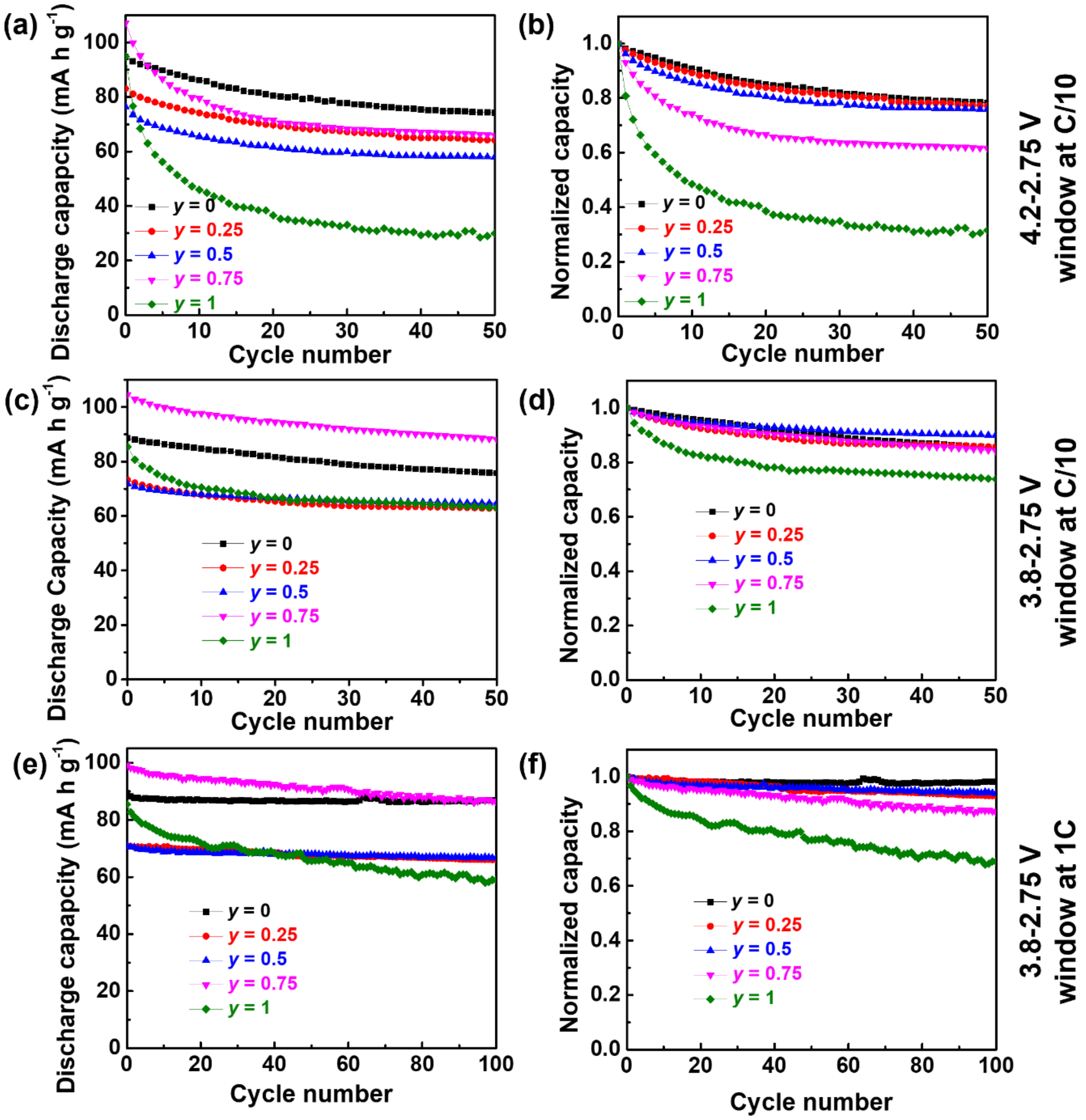

Figure 3.11. Discharge (a, c, e) and normalized (b, d, f) capacity *vs.* cycle number plots of the $Na_{3+y}V_{2-y}Mn_y(PO_4)_3$ cathodes.

When the cycling window is restricted to 3.8-2.75 V *vs.* $Na^{+/}Na^0$, the end member cathodes ($y = 0$ and 1) display similar first cycle capacities (~ 90 mA h g^{-1}). Whilst the former candidate maintains ~ 86 % of it, significant capacity loss (~ 26 %) is observed for the later during the first 50 cycles. The $y = 0.25$ and 0.5 cathodes show slightly lower initial capacities (~ 70 mA h g^{-1}) in comparison with the unsubstituted NVP cathode, which could be due to the presence of electrochemically inactive Mn^{2+}. Besides, all three cathodes have retained ~ 90 % of their initial capacities at the end of 50th cycle. As discussed earlier, the $y = 0.75$ cathode delivers higher capacity (~ 104 mA h g^{-1}) in this cathode series and maintains ~85 % of it at the end of 50th cycle. Further, the cycling stabilities of these NASICON cathodes are also evaluated at 1C rate for 100 cycles in the same voltage window (Figure 3.11e and f). All the cathodes display similar capacity retention trends in comparison with C/10 rate tests with slightly lower capacities. Thus, it is clear that the $y \leq 0.5$ cathodes show better capacity retention in comparison with the other two Mn-rich candidates. While the reason for such decay is still unclear, we presume that it could be due to the repeated phase transformations associated with the formation of Jahn-Teller Mn^{3+} cations during cycling, as observed in the other Mn containing NASICON cathode.[43,44] More importantly, the $Na_{3.75}V_{1.25}Mn_{0.75}(PO_4)$ cathode delivers initial capacities of 98 and 88 mA h g^{-1} at 1C and 5C with the capacity retentions of 87 and 96 %, respectively after 100 cycles (Figure 3.12a). The corresponding initial Coulombic efficiencies are found to be 82 and 91 % at 1C and 5C, respectively and they are maintained closer to 100 % for the remaining cycles.

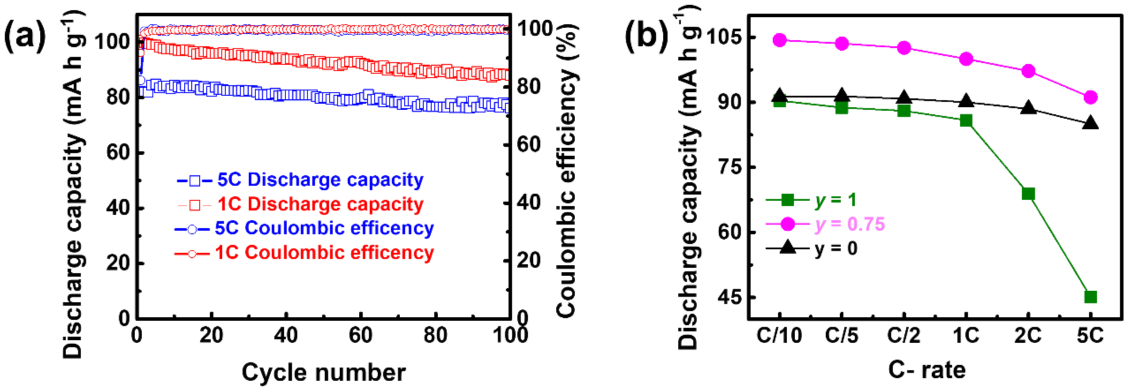

Figure 3.12. (a) Capacity retention plots of $Na_{3.75}V_{1.25}Mn_{0.75}(PO_4)_3$ cathode at different C-rates. (b) rate capability of the $Na_{3+y}V_{2-y}Mn_y(PO_4)_3$ cathodes.

Lastly, another figure of merit, i.e., rate capability of the $Na_{3.75}V_{1.25}Mn_{0.75}(PO_4)_3$ cathode is compared with that of the end members (Figure 3.12b). The $Na_3V_2(PO_4)_3$ cathode delivers discharge capacities of 90 and 84 mA h g^{-1} at C/10 and 5C, respectively. However, the discharge capacities of the $Na_4VMn(PO_4)_3$ cathode have severely decreased at higher C-rates (69 and 44 mA h g^{-1} at 2C and 5C rates, respectively). Interestingly, the $Na_{3.75}V_{1.25}Mn_{0.75}(PO_4)_3$ exhibits capacities as high as 100 and 95 mA h g^{-1} at 1C and 2C, respectively and even 86% of its initial capacity (i.e., 104 mA h g^{-1}) can be obtained during a discharge time of ~20 minutes (i.e., 5C rate). Such stellar rate performance is found to be better than layered oxides and could be comparted to $Na_3V_2(PO_4)_2F_3$ cathode.[45]

To better understand about the outstanding performance of the $Na_{3.75}V_{1.25}Mn_{0.75}(PO_4)_3$ cathode in comparison with the end members, their potential *vs*. capacity plots are compared at different C-rates (Figure 3.13 and Table 3.4). We also recall our earlier findings on bottleneck sizes (T1 and T2) and V- and Mn-redox activities from the Rietveld and DFT analyses, respectively (Figure 3.2d and 3.10). Despite the fact that fair redox activities for both V- and Mn-redox centers are observed in the $Na_4VMn(PO_4)_3$ cathode, it shows the largest polarizations and limited capacities at all C-rates in this series of cathodes. This could be ascribed to its smaller bottleneck size (~4.7 Å^2), which needs higher activation energies.[36] The other endmember cathode ($Na_3V_2(PO_4)_3$) presents the larger bottleneck size (~5.15 Å^2), which requires lower activation energies for Na-ion mobility. Thus, it shows minimum increase of polarization and decrease of capacity (93 %) when the C-rate is increased from C/10 to 5C. Turning back to the performances of the $Na_{3.75}V_{1.25}Mn_{0.75}(PO_4)_3$ cathode, it exhibits similar polarization value compared to $Na_3V_2(PO_4)_3$ at C/10. As the C-rate increases to 5C, its capacities decline by 86 % along with moderate increase of polarizations. These observations clearly indicate that the kinetics of sodium (de)intercalation is relatively slower in the $Na_{3.75}V_{1.25}Mn_{0.75}(PO_4)_3$ cathode compared to the $Na_3V_2(PO_4)_3$ at higher C-rates. It could be attributed to its relatively smaller bottleneck size (i.e., ~ 0.1 Å^2 lesser than that of $Na_3V_2(PO_4)_3$). Nevertheless, the highly active V- and Mn- redox centers enables it to deliver higher capacities at high C-rates.

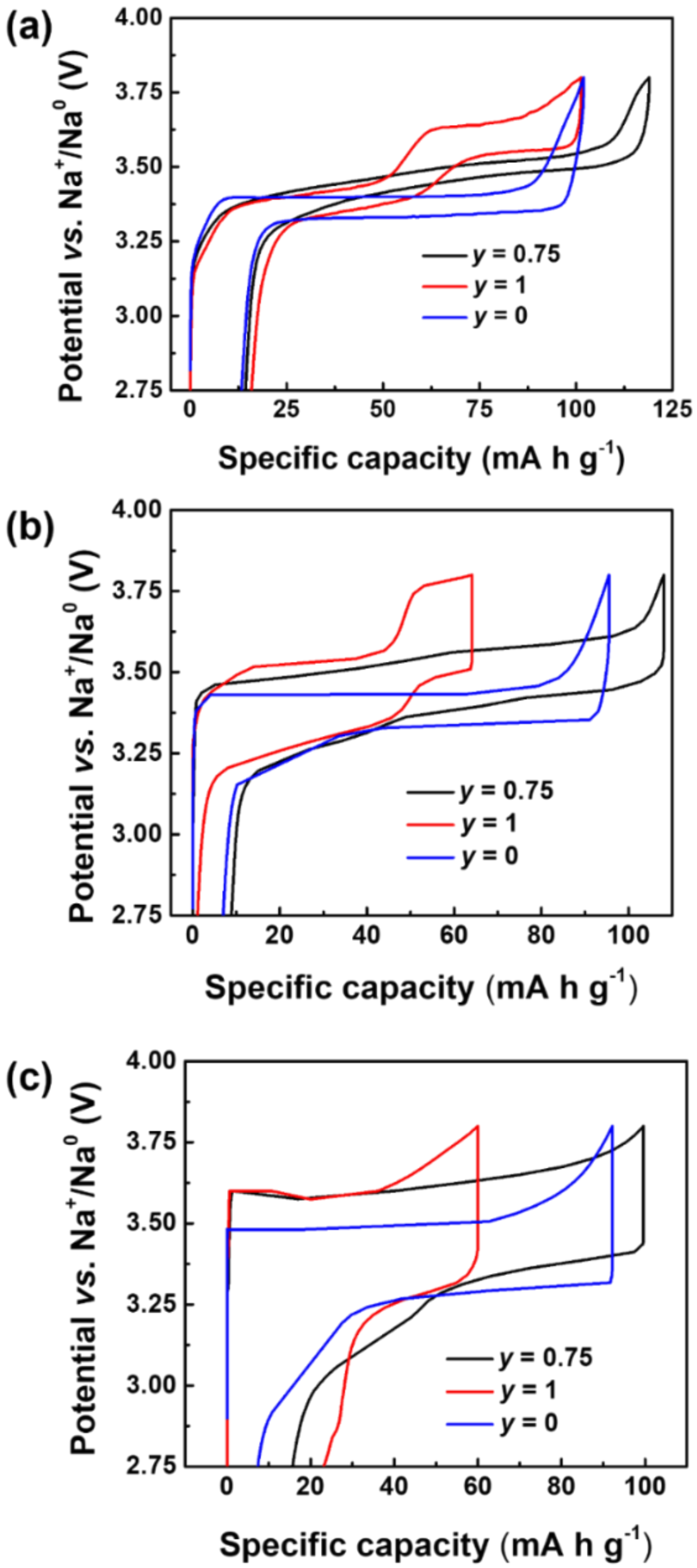

Figure 3.13. Potential *vs.* capacity plots of the $Na_{3+y}V_{2-y}Mn_y(PO_4)_3$ cathodes cycled at (a) C/10, (b) 1C and (c) 5C.

Table 3.4. Polarization values (V) of the $Na_{3+y}V_{2-y}Mn_y(PO_4)_3$ cathodes calculated from Figure 3.12.

NASICON cathodes	**C/10**	**1C**	**5C**
$Na_3V_2(PO_4)_3$	0.05	0.1	0.22
$Na_{3.75}V_{1.25}Mn_{0.75}(PO_4)_3$	0.047	0.17	0.33
$Na_4VMn(PO_4)_3$	0.05	0.3	0.4

3.4. Conclusion

To sum up, we have performed a comprehensive study to understand the role of Mn^{2+} cation in the NVP structure with respect to their structural and electrochemical sodium (de)intercalation properties. The Mn^{2+} is completely soluble in the NVP structure, except at $y = 0.5$ where the product is decomposed into two NASICON phases. Further, the DFT calculations have verified the lower stability of the $Na_{3.5}V_{1.5}Mn_{0.5}(PO_4)_3$ phase which could be attributed to the significant mismatch between VO_6 and MnO_6 octahedra. The $Na/Na_{3+y}V_{2-y}Mn_y(PO_4)_3$ cells show the decrease of intercalation capacities of the $Na_{3+y}V_{2-y}Mn_y(PO_4)_3$ cathodes when y is increased from 0 to 0.5 followed by the increase for the case of $y = 0.75$ and 1 cathodes within the voltage window of 3.8-2.75 V vs. $Na^{+/}Na^0$. Further upon extending the upper cutoff voltage to 4.2 V vs. $Na^{+/}Na^0$, the reversible capacities are slightly increased (~80 mA h g^{-1}) for the case of $y = 0.25$ and 0.5 cathodes. On the other hand, despite their enhanced first charge capacity, the $y = 0.75$ and 1 cathodes show faster capacity degradation. The *ex-situ* XRD studies have shown the structural integrity of the $Na_{3.25}V_{1.75}Mn_{0.25}(PO_4)_3$ cathode in both voltage windows, whereas the $Na_{3.75}V_{1.25}Mn_{0.75}(PO_4)_3$ phase undergoes irreversible structural changes when it is charged to 4.2 V vs. Na^+/Na^0. The *ex-situ* XAS studies have clearly distinguished the redox inactive and active Mn^{2+} centers in the $Na_{3.25}V_{1.75}Mn_{0.25}(PO_4)_3$ and $Na_{3.75}V1._{25}Mn_{0.75}(PO_4)_3$ cathodes, respectively. Further, the DFT calculations have provided insights on V- and Mn-redox centers. Finally, the galvanostatic cycling and rate tests reveal high reversible capacity and rate capability for the $Na_{3.75}V_{1.25}Mn_{0.75}(PO_4)_3$ cathode, which could be ascribed to the optimum bottleneck size for Na-ion diffusion as well as the modulated V- and Mn-redox centers. We believe our experimental findings will encourage researchers to focus more on fine tuning electronic and crystal structures of NASICON frameworks by carefully controlling the substituent concentrations to achieve high performance Na-ion cathodes.

References

[1] N. Yabuuchi, K. Kubota, M. Dahbi, S. Komaba, *Chem. Rev.* **2014**, *114*, 11636.

[2] L. Li, Y. Zheng, S. Zhang, J. Yang, Z. Shao, Z. Guo, *Energy Environ. Sci.* **2018**, *11*, 2310.

[3] P. F. Wang, Y. You, Y. X. Yin, Y. G. Guo, *Adv. Energy Mater.* **2017**, *8*, 1701912.

[4] M. H. Han, E. Gonzalo, G. Singh, T. Rojo, *Energy Environ. Sci*. **2015**, *8*, 81.

[5] C. Masquelier, L. Croguennec, *Chem. Rev.* **2013**, *113*, 6552.

[6] S. Chen, C. Wu, L. Shen, C. Zhu, Y. Huang, K. Xi, J. Maier, Y. Yu, *Adv. Mater.* **2017**, *29*, 1700431.

[7] W. Song, X. Ji, Y. Zhu, H. Zhu, F. Li, J. Chen, F. Lu, Y. Yao, C. E. Banks, *ChemElectroChem*, **2014**, *1*, 871.

[8] H. Gao, J. B. Goodenough, *Angew. Chem. Int. Ed*. **2016**, *55*, 12768.

[9] S. Y. Lim, H. Kim, R. A. Shakoor, Y. Jung, J. W. Choi, J. Electrochem. Soc. **2012**, 15*9*, A1393.

[10] X. Zhang, X. Rui, D. Chen, H. Tan, D. Yang, S. Huang, Y. Yu, *Nanoscale*, **2019**, *11*, 2556.

[11] L. S. Plashnitsa, E. Kobayashi, Y. Noguchi, S. Okada, J. Yamaki, *J. Electrochem. Soc*. **2010**, *157,* A536.

[12] J. Kang, Sora Baek, V. Mathew, J. Gim, J. Song, H. Park, E. Chae, A. K. Rai, J. Kim, *J. Mater. Chem.* **2012**, *22*, 20857.

[13] Z. Jian, L. Zhao, H. Pan, Y. S. Hu, H. Li, W. Chen, L. Chen, *Electrochem. commun.* **2012**, *14*, 86.

[14] K. Saravanan ,C. W. Mason, A. Rudola, K. H. Wong, P. Balaya, *Adv. Energy Mater.* **2013**, *3*, 444.

[15] Q. Zhu, X. Chang, N. Sun, R. Chen, Y. Zhao, B. Xu, F. Wu, *ACS Appl. Mater. Interfaces*, **2019**, *11*, 3107.

[16] C. Zhu, K. Song, P. A. Van Aken, J. Maier, Y. Yu, *Nano Lett.* **2014**, *14*, 2175.

[17] Z. Jian, W. Han, X. Lu, H. Yang, Y. S. Hu, J. Zhou, Z. Zhou, J. Li, W. Chen, D. Chen,

L. Chen, *Adv. Energy Mater.* **2013**, *3*, 156.

[18] Y. H. Jung, C. H. Lim, D. K. Kim, *J. Mater. Chem. A*, **2013**, *1*, 11350.

[19] J. Hwang, K. Matsumoto, R. Hagiwara, *ACS Appl. Energy Mater.* **2019**, *2*, 2818.

[20] L. Chen, Y. Zhao, S. Liu, L. Zhao, *ACS Appl. Mater. Interfaces*, **2017**, *9*, 44485.

[21] X. Jiang, T. Zhang, J. Y. Lee, *ACS Sustain. Chem. Eng.* **2017**, *5*, 8447.

[22] L. Zhao, H. Zhao, X. Long, Z. Li, Z. Du, *ACS Appl. Mater. Interfaces*, **2018**, *10*, 35963.

[23] C. Zhu, K. Song, P. A. Van Aken, J. Maier, Y. Yu, *Nano Lett.* **2014**, *14*, 2175.

[24] M. J. Aragón, P. Lavela, G. F. Ortiz, J. L. Tirado, *ChemElectroChem*, **2015**, *2*, 995.

[25] A. Inoishi, Y. Yoshioka, L. Zhao, A. Kitajou, S. Okada, *ChemElectroChem*, **2017**, *4*, 2755.

[26] W. Shen, H. Li, Z. Guo, Z. Li, Q. Xu, H. Liu, Y. Wang, *RSC Adv.* **2016**, *6*, 71581.

[27] F. Lalère, V. Seznec, M. Courty, R. David, J. N. Chotard, C. Masquelier, *J. Mater. Chem. A*, **2015**, *3*, 16198.

[28] H. Li, H. Tang, C. Ma, Y. Bai, J. Alvarado, B. Radhakrishnan, S. P. Ong, F. Wua, Y. S. Meng, C. Wu, *Chem. Mater.* **2018**, *30*, 2498.

[29] X. Liu, G. Feng, E. Wang, H. Chen, Z. Wu, W. Xiang, Y. Zhong, Y. Chen, X. Guo, B. Zhong, *ACS Appl. Mater. Interfaces*, **2019**, *11*, 12421.

[30] R. Liu, G. Xu, Q. Li, S. Zheng, G. Zheng, Z. Gong, Y. Li, E. Kruskop, R. Fu, Z. Chen, K. Amine, Y. Yang, *ACS Appl. Mater. Interfaces*, **2017**, *9*, 43632.

[31] W. Zhou, L. Xue, X. Lü, H. Gao, Y. Li, S. Xin, G. Fu, Z. Cui, Y. Zhu, J. B. Goodenough, *Nano Lett.* **2016**, *16*, 7836.

[32] H. Li, T. Jin, X. Chen, Y. Lai, Z. Zhang, W. Bao, L. Jiao, *Adv. Energy Mater.* **2018**, *8*, 1801418.

[33] F. Chen, V. M. Kovrugin, R. David, O. Mentré, F. Fauth, J. N. Chotard, C. Masquelier, *Small Methods*, **2019**, *3*, 1800218.

[34] M. V. Zakharkin, O. A. Drozhzhin, I. V. Tereshchenko, D. Chernyshov, A. M. Abakumov, E. V. Antipov, K. J. Stevenson, *ACS Appl. Energy Mater.* **2018**, *1*, 5842.

[35] E. R. Losilla, M. A. G. Aranda, S. Bruque, M. A. París, J. Sanz, A. R. West, *Chem. Mater.* **1998**, *10*, 665.

[36] M. Guin, F. Tietz, *J. Power Sources*, **2015**, *273*, 1056.

[37] I. V. Zatovsky, *Acta Cryst.* **2010**, *66*, i12.

[38] C. Delmas, R. Olazcuaga, G. Le Flem, P. Hagenmuller, F. Cherkaoui, R. Brochu, *Mat. Res. Bull.* **1981**, *16*, 285.

[39] R. D. Shannon, *Acta Cryst.* **1976**, *A32*, 751.

[40] G. Zhang, T. Xiong, M. Yan, Y. Xu, W. Ren, X. Xu, Q. Wei, L. Mai, *Chem. Mater*. **2017**, *29*, 8057.

[41] Z. Jian, C. Yuan, W. Han, X. Lu, L. Gu, X. Xi, Y. S. Hu, H. Li, W. Chen, D. Chen, Y. Ikuhara, L. Chen, *Adv. Funct. Mater.* **2014**, *24*, 4265.

[42] Q. Bai, L. Yang, H. Chen, Y. Mo, *Adv. Energy Mater*. **2018**, *8*, 1702998.

[43] H. Gao, Y. Li, K. Park, J. B. Goodenough, *Chem. Mater*. **2016**, *28*, 6553.

[44] H. Gao, I. D. Seymour, S. Xin, L. Xue, G. Henkelman, J. B. Goodenough, *J. Am. Chem. Soc*. **2018**, *140*, 18192.

[45] S. Mariyappan, Q. Wang, J. M. Tarascon, *J. Electrochem. Soc.* **2018**, *165*, A3714.

Chapter – 4

Elucidating the Impact of Mg Substitution on the Properties of NASICON-$Na_{3+y}V_{2-y}Mg_y(PO_4)_3$ Cathodes

Vanadium multi-redox based NASICON-$Na_zV_{2-y}M_y(PO_4)_3$ ($3 \leq z \leq 4$; M = Al^{3+}, Cr^{3+} and Mn^{2+}) cathodes are particularly attractive for Na-ion battery applications due to their high Na insertion voltage (>3.5 V vs. Na^+/Na^0), reversible storage capacity (~150 mA h g^{-1}) and rate performance. However, their practical application is hindered by rapid capacity fade due to bulk structural rearrangements at high potentials involving complex redox and local structural changes. To decouple these factors, we have studied a series of Mg^{2+} substituted $Na_{3+y}V_{2-y}Mg_y(PO_4)_3$ ($0 \leq y \leq 1$) cathodes for which the only redox-active species is vanadium. Whilst X-ray diffraction (XRD) confirms the formation of solid solutions between the $y = 0$ and 1 end members, X-ray absorption spectroscopy and solid-state nuclear magnetic resonance reveal a complex evolution of the local structure upon progressive Mg^{2+} substitution for V^{3+}. Concurrently, the intercalation voltage rises from 3.35 to 3.45 V, due to increasingly more ionic V-O bonds, and the sodium (de)intercalation mechanism transitions from a two-phase for $y \leq 0.5$ to a solid solution process for $y \geq 0.5$, as confirmed by *in-operando* XRD, whilst Na-ion diffusion kinetics follow a non-linear trend across the compositional series.

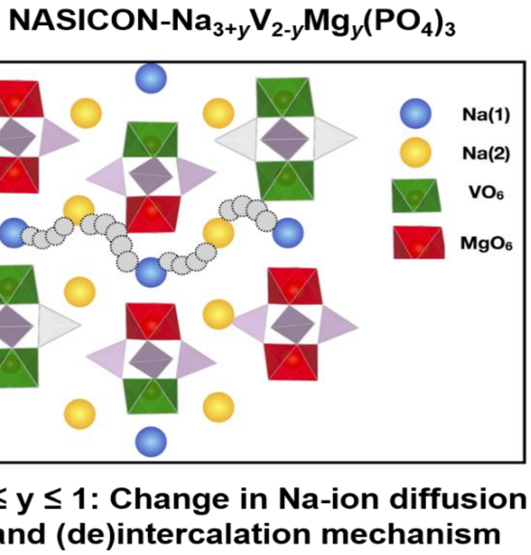

4.1. Introduction

The successful utilization of renewable energy derived from intermittent sources, such as wind and solar, necessitates the deployment of large-scale electrochemical energy storage devices.[1] Given their successful implementation in portable electronics and electric vehicle applications, Li-ion batteries are serious contenders for grid-level storage. However, the soaring price of lithium precursors and geopolitical uncertainty associated with their supply chain have encouraged researchers to develop alternative technologies. Among those, Na-ion batteries are very promising due to their inexpensive and Earth abundant precursors.[2] Over the past decade, a large number of Na-ion electrode and electrolyte materials have been discovered, in part thanks to the materials design knowledge gained from earlier investigations of Li-based systems and the similar properties of Li and Na alkali metals. However, the exploration of suitable Na-ion cathodes with high energy density, good rate performance and long cycle life remains critical. To this end, NA SuperIonic CONductor (NASICON)-type phosphate cathodes are particularly appealing because of their high insertion voltages and good sodium diffusivity, as well as excellent structural and thermal stabilities.[3]

The general chemical composition of transition metal-based NASICON phosphates can be written as $Na_zM_2(PO_4)_3$ ($0 \leq z \leq 4$; M = first and second row early transition metals).[4] Their three-dimensional crystal structure is generally described using a rhombohedral $R\bar{3}c$ space group and is built from so-called ‘lantern’ units, which consist of two MO_6 octahedra and three XO_4 tetrahedra, stacked along the *c*-direction. In this structure, Na^+ ions occupy two different crystallographic sites, namely 6*b* Na(1) and 18*e* Na(2), with a maximum number of four Na per formula unit. Earlier studies on $Na_3M_2(PO_4)_3$ (M = Ti, V, Cr and Fe) [5-8] have reported a maximum reversible exchange of two moles of Na per formula unit (*pfu*), corresponding to a one-electron redox process per transition metal center, leading to moderate charge storage capacities of ~100-120 mA h g^{-1}. One obvious avenue to improve the capacity of NASICON phosphate cathodes is to introduce multi-electron redox centers to enable the exchange of a larger number of sodium ions in the framework. From this viewpoint, the $Na_3V_2(PO_4)_3$ (NVP) cathode has received a lot of attention as V^{3+} can, in theory, undergo a two-electron redox process to form V^{5+} on charge, yet only V^{4+}/V^{3+} redox has been realized experimentally.[9] This limitation has motivated several studies of *iso*- and *alio*-valent cationic substitutions into NVP to realize multi-electron $V^{5+}/V^{4+}/V^{3+}$ redox reactions.[10-16] This strategy has proven successful for *iso*-valently substituted cathodes, such as $Na_3V_{1.5}Al_{0.5}(PO_4)_3$ and $Na_3VCr(PO_4)_3$, which exhibit two step voltage profiles at 3.4 and 4.0 V *vs*. Na^+/Na^0 corresponding to the redox activity of the V^{4+}/V^{3+} and V^{5+}/V^{4+} couples, respectively. Although the high intercalation voltage of the V^{5+}/V^{4+} couple leads to improvements in energy density compared to unsubstituted NVP, their intercalation capacities are similar to that of NVP (i.e., two moles of Na-ions exchanged *pfu*). Alternatively, aliovalent Mn^{2+} substitution into the NVP framework results in the formation of a fully sodiated NASICON-$Na_4VMn(PO_4)_3$ cathode.[17] When cycled between 3.75 and 2.5 V *vs*. Na^+/Na^0, this material exhibits two voltage plateaus at 3.4 (V^{4+}/V^{3+}) and 3.6 V (Mn^{3+}/Mn^{2+}) *vs*. Na^+/Na^0, but is again limited to two moles of reversible Na-ion exchange *pfu*. Upon extending the charge voltage window to 4.2 V *vs*. Na^+/Na^0, an additional one mole of sodium ions can be removed, raising the total charge capacity of the $Na_4VMn(PO_4)_3$ cathode to 150 mA h g^{-1}.[18] This additional capacity has been attributed to the redox activities of the V^{5+}/V^{4+} and Mn^{4+}/Mn^{3+} couples. Unfortunately, on subsequent discharge, only 1.5 moles of Na^+ ions are reinserted into the structure. *In-operando* XRD studies have attributed this capacity loss to an irreversible structural transformation of the NASICON framework at high voltage, triggered by the removal of Na^+ ions from Na(1) sites and possible vanadium cation migration into them.[19,20] Further, the $Na_4VMn(PO_4)_3$ cathode displays rapid capacity fade upon cycling. Structural and capacity degradation upon high voltage cycling has also been observed in Mn-rich $Na_{3+y}V_{2-y}Mn_y(PO_4)_3$ cathodes.[21,22]

However, it is not yet clear what role concomitant local structural and electronic processes occurring at higher voltages play in the abovementioned issues. Specifically, the interplay between the removal of Na^+ ions from Na(1) and Na(2) sites and the oxidation of V^{4+} to V^{5+} as well as Mn^{3+} to Mn^{4+} and associated changes to $(V/Mn)O_6$ local environments makes it difficult to separate individual contributions to the observed electrode degradation phenomena. Therefore, it is necessary to decouple structural and electronic processes to better understand the links between structure/composition and electrochemical properties.

In the present work, we have designed a series of Mg^{2+}-substituted NASICON cathodes with compositions $Na_{3+y}V_{2-y}Mg_y(PO_4)_3$ akin to previously-studied Mn^{2+}-substituted NVP compounds.[21,22] The electrochemical inactivity of Mg^{2+} entails that V redox centers are solely responsible for Na^+ exchange in the $Na_{3+y}V_{2-y}Mg_y(PO_4)_3$ cathodes, which enables us to follow structural and electrochemical (de)sodiation processes during charge-discharge more clearly than in the structurally and compositionally-similar V^{3+}-Mn^{2+} system. Specifically, this study allows us to evaluate the impact of metal mixing on the V site on the Na (de)intercalation mechanism, on the electrochemical reversibility, and on Na^+ diffusion kinetics, without the complications of multi-metal redox processes on charge-discharge. We find that the progressive replacement of V^{3+} by Mg^{2+} in these Na-ion intercalation hosts provides a convenient handle for tuning their average intercalation voltage, voltage hysteresis and Na (de)intercalation mechanism.

4.2. Experimental

NASICON-$Na_{3+y}V_{2-y}Mg_y(PO_4)_3$ samples were synthesized using sol–gel method. Initially V_2O_5 (99.6%, Sigma) was reduced using citric acid (99.5%, Sigma) in water following addition of stoichiometric amount of NaH_2PO_4 (99%, Sigma), Na_2CO_3 (99.5%, Sigma), and Mg-acetate (99%, Sigma) and the solution was subsequently heated at 100 °C to obtain powder mixture. The recovered powders were grinded using a mortar and pestle followed by annealing at 350 °C for 10 h and 700 °C for 12 h in N_2 atmosphere with an intermittent grinding.

For the details of the material and electrochemical characterizations, see Chapter 2.

4.3. Results and Discussion

NASICON-$Na_{3+y}V_{2-y}Mg_y(PO_4)_3$ (y = 0, 0.25, 0.5, 0.75 and 1) cathodes were prepared *via* a sol-gel assisted high temperature method. Particle morphology of the as-prepared cathodes was studied using scanning electron microscopy (SEM) (Figure 4.1). The micrographs indicate the formation of micron-sized secondary particles composed of nanoscale primary particles, while CHN elemental analysis reveals the presence of 3-5 wt% carbon in the NASICON samples (Table 4.1).

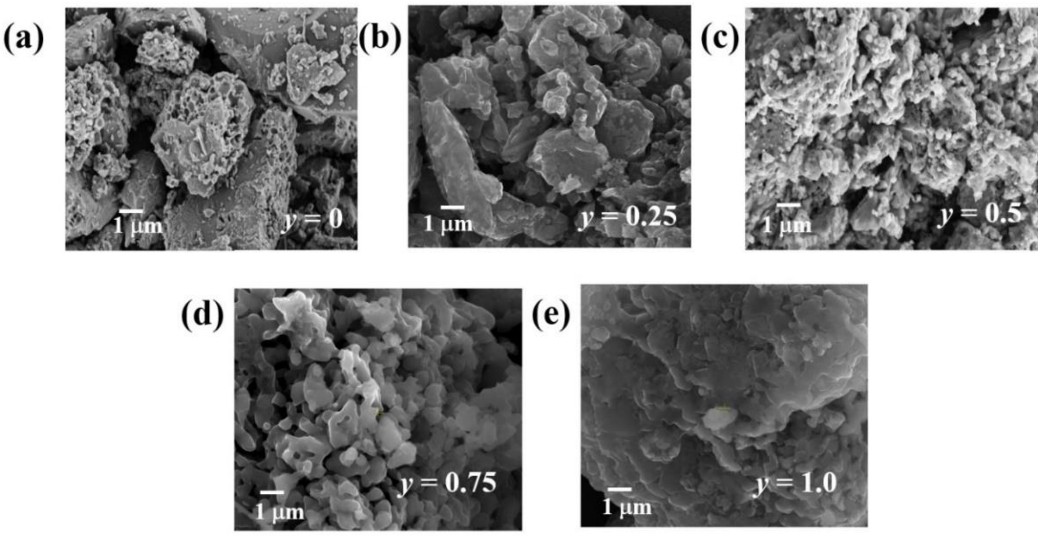

Figure 4.1. SEM images of NASICON-$Na_{3+y}V_{2-y}Mg_y(PO_4)_3$ cathodes.

Table 4.1. CHN analysis of as-synthesized $Na_{3+y}V_{2-y}Mg_y(PO_4)_3$.

$Na_{3+y}V_{2-y}Mg_y(PO_4)_3$	Carbon content (%)
$y = 0$	3.25
$y = 0.25$	4.97
$y = 0.5$	4.51
$y = 0.75$	5.13
$y = 1$	4.07

X-ray diffraction (XRD) measurements were conducted to study the solubility of Mg^{2+} cations in the NVP framework (Figure 4.2a). All of the Bragg peaks observed for the $Na_{3+y}V_{2-y}Mg_y(PO_4)_3$ cathode samples can be fully indexed using a rhombohedral $R\bar{3}c$ space group, with no evidence of crystalline impurities. It is also worth noting that Inoishi *et al.*[11] highlighted the solubility limit of Mg^{2+} in the NVP lattice as $y = 0.5$, however, their sample preparation involved a high temperature annealing (800 °C) step that could lead to phase decomposition. To gain insights into long-range structural changes upon Mg^{2+} substitution, Rietveld refinements of the lab XRD data were carried out, and the results are displayed in Figures 4.2b, with structural parameters summarized in Table 4.2. Although NVP undergoes a series of phase transitions upon cooling from the $R\bar{3}c$ form to a monoclinic C2/c structure near room temperature due to Na^+-ion/vacancy ordering,[23] herein its XRD pattern is refined using the rhombohedral $R\bar{3}$c setting for the sake of comparison across the compositional series, and because the use of a C2/c structural model does not improve the refinement significantly. As the concentration of Mg^{2+} (y) increases from 0 to 1 in the NVP framework, we notice anisotropic changes to the lattice parameters along with an expansion of the unit cell volume ($\Delta a/a = +1.75$ %, $\Delta c/c = -1.75$ %, and $\Delta V/V = + 1.71$ %). The decrease in the *c*- lattice parameter with increasing y (from $y = 0.25$ to $y = 1$) can be related to the progressive filling of Na(1) sites, which minimizes the electrostatic repulsion between oxygen layers perpendicular to the *c*-axis of the NASICON structure. The larger ionic radius of Mg^{2+} ($r_{Mg^{2+}} = 0.72$ Å), as compared to V^{3+} ($r_{V^{3+}}$ = 0.64 Å), and the increase in Na(2) site population, are responsible for the increase in *a*-parameter. Further, BVS calculations reveal minor changes to the average (V/Mg)-O and Na(1)-O bond lengths, and reduced $(V/Mg)O_6$ and $Na(1)O_6$ octahedral distortions upon increased Mg^{2+} substitution (Table 4.2), which is also confirmed by X-ray absorption spectroscopy (XAS) results presented in the next section. When comparing these structural changes to those reported in our recent study of Mn^{2+} substitution into the NVP lattice,[21] we notice that $(V/Mg)O_6$ octahedra in $Na_{3+y}V_{2-y}Mg_y(PO_4)_3$ are less distorted (Δ = 2-3 $\times 10^{-4}$) than $(V/Mn)O_6$ octahedra in $Na_{3+y}V_{2-y}Mn_y(PO_4)_3$ (Δ = 5–7 $\times 10^{-4}$), which is presumably due to the different ionic sizes and bonding characteristics of Mg^{2+} and Mn^{2+}.

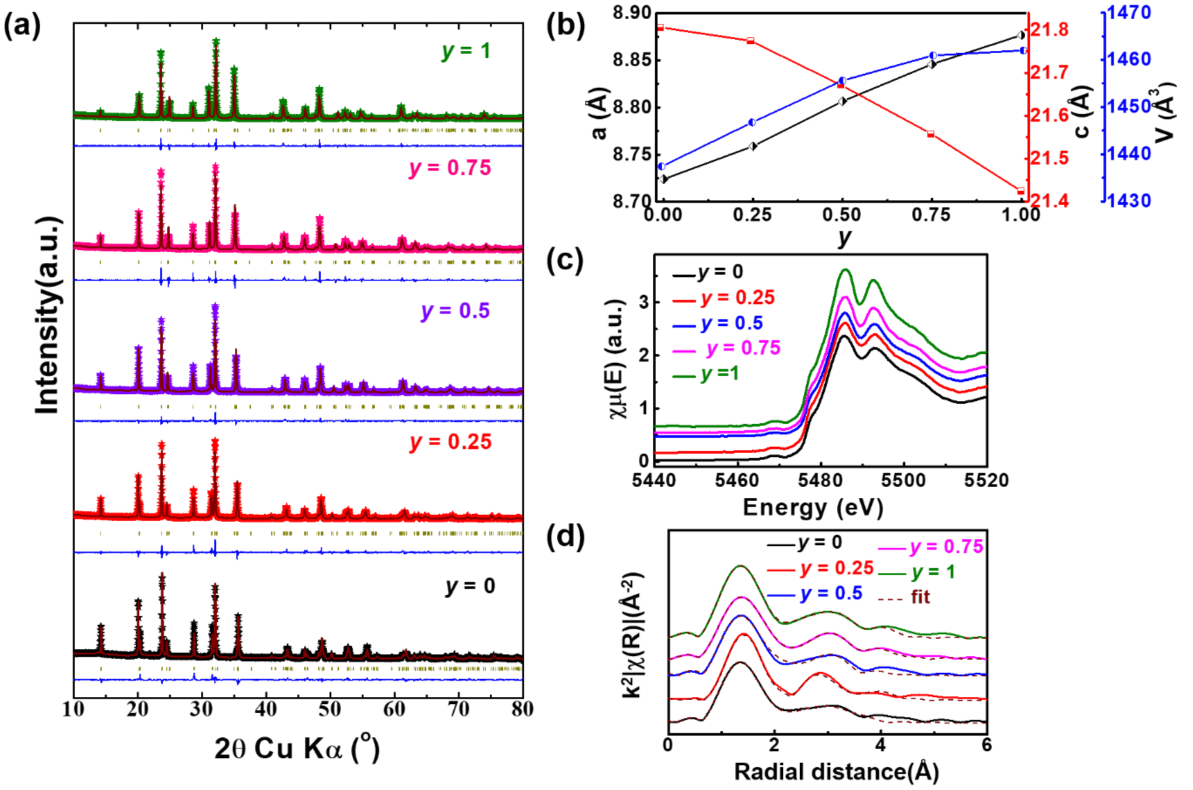

Figure 4.2. (a) Rietveld analysis of powder XRD patterns collected on $Na_{3+y}V_{2-y}Mg_y(PO_4)_3$ samples. (b) Variations in the unit cell parameters and volumes as a function of *y*. (c) Normalized absorption spectra and (d) FT-EXAFS at the V K-edge of the $Na_{3+y}V_{2-y}Mg_y(PO_4)_3$ cathodes.

Table 4.2. Lattice parameters and bond distances obtained from the Rietveld analysis of the powder XRD patterns of $Na_{3+y}V_{2-y}Mg_y(PO_4)_3$ samples.

	$y = 0$	**$y = 0.25$**	**$y = 0.5$**	**$y = 0.75$**	**$y = 1$**
Lattice parameters (Å)	a = 8.724(1) c =21.806(6)	a = 8.7590 (17) c = 21.7745 (7)	a = 8.8067 (33) c = 21.6716 (12)	a = 8.8460 (17) c = 21.5580 (7)	a = 8.8768 (15) c = 21.4240 (6)
Na(1) occupancy	0.79	0.722(7)	0.757(8)	0.913(1)	1
Na(2) occupancy	0.713	0.767(2)	0.848	0.899(5)	0.963(6)
V–O average bond length (Å)	2.0541(1) × 6	2.0375 (1) × 6	2.0418 (5) × 6	2.0447(3) × 6	2.0458 (4) × 6
Na(1)–O average bond length (Å)	2.4305(1)× 6	2.4239(1)× 6	2.4227(1)× 6	2.4199(1)× 6	2.4148(1)× 6
Na(2)–O average bond length (Å)	2.4325(1)× 2 2.4434(1)× 2 2.8855(0)× 2 2.6125(1)× 2	2.4182(2)× 2 2.4713(2)× 2 2.8787(0)× 2 2.6085(1)× 2	2.4314(1)× 2 2.4846(1)× 2 2.8890(0)× 2 2.6006(1)× 2	2.4428(1)× 2 2.4921(1)× 2 2.8998(0)× 2 2.5905(1)× 2	2.4511(1)× 2 2.5019(1)× 2 2.9039(0)× 2 2.5790(1)× 2
Reliability factors	R_{wp} = 3.9% Chi^2 = 3.47	R_{wp} = 3.62% Chi^2 = 3.54	R_{wp} = 2.98% Chi^2 = 2.75	R_{wp} = 3.43% Chi^2 = 2.71	R_{wp} = 3.70% Chi^2 = 2.62

First principles calculations were carried out to confirm the phase stability and to evaluate the most favorable V/Mg ordering for the various $Na_{3+y}V_{2-y}Mg_y(PO_4)_3$ compositions of interest. Before proceeding with electronic structure calculations, we generated all possible configurations of the $Na_{3+y}V_{2-y}Mg_y(PO_4)_3$ series using the Supercell code to identify the most stable arrangement of V/Mg species and most favorable distribution of Na amongst Na(1) and Na(2) lattice sites. Firstly, the crystal structure of $Na_4VMg(PO_4)_3$ obtained from Rietveld analysis was used in a 2 x 1 x 3 primitive cell configuration (containing 6 formula units) to generate multiple random orderings of V/Mg and Na(1/)Na(2). With the help of Supercell code, we generated random prototypical disordered structures, through Special Quasirandom Structures (SQS) approximation. Geometry optimization was carried out for the symmetrically unique structures, which were isolated by visual inspection on VESTA.

Thereafter, we replicated the $Na_4VMg(PO_4)_3$ primitive cell twice along the *c*-axis, generating a 2 x 1 x 6 supercell in the process. This large supercell (containing 12 formula units) allowed for intermediate compositions within the $Na_{3+y}V_{2-y}Mg_y(PO_4)_3$ series to be generated by removing stoichiometric amounts of Na(1) and Na(2), while changing the V/Mg ratio. A similar procedure as the one employed for the $Na_4VMg(PO_4)_3$ was followed to obtain symmetrically-unique optimized structures for all of the compositions of interest.

The formation energies of all these configurations were computed using the following formula: $\Delta E_f = E_i - (y-3) \times E_{[Na_4VMg(PO_4)_3]} - (4-y) \times E_{[Na_3V_2(PO_4)_3]}$, where E_i is the total energy of the $Na_{3+y}V_{2-y}Mg_y(PO_4)_3$ phase, and $E_{[Na_3V_2(PO_4)_3]}$ and $E_{[Na_4VMg(PO_4)_3]}$ are the energies of the end member phases, y = 0 and 1, respectively. A convex hull was constructed for y = 0 through 1, to understand the thermodynamic stability of the intermediate phases with respect to the end members. The most preferred V/Mg and Na(1)/Na(2) distribution for each $Na_{3+y}V_{2-y}Mg_y(PO_4)_3$ composition corresponds to the structure with the lowest formation energy after structural relaxation, as shown in the convex hull in Figure 4.3a. It is observed that the V/Mg ordering has a significant impact on the formation energies for different compositions. While the difference in energies is not conspicuous for exchanging Na ions between Na(1) and Na(2) sites, interchanging the transition metal cation sites leads to the modification of the local environments of Na, which in turn leads to larger differences in formation energies. The reason behind this effect is that upon replacing a V^{3+} center with Mg^{2+}, the average Na(1)-O and Na(2)-O bond distances are slightly reduced due to lower electrostatic repulsions between Na^+ and

Mg^{2+} polyhedra, compared to Na^+ and V^{3+} polyhedra (Table 4.3). However, the increase of number of V/Mg site exchanges lead to destabilization of the system, thus resulting in energies much higher than the hull.

The optimized lattice parameters for the most stable $Na_{3+y}V_{2-y}Mg_y(PO_4)_3$ (in 1x1x1 conventional cell configurations) are summarized in Table 4.4 and their evolution resemble our XRD results. We note here that no particular V and Mg ordering is observed for the lowest energy structures of $Na_{3+y}V_{2-y}Mg_y(PO_4)_3$, in good agreement with our experimental XRD results. We observe 3 types of local environments for Na(1) in the NASICON skeleton, namely, MgO_6-Na(1)O_6-MgO_6, VO_6-Na(1)O_6-MgO_6 and VO_6-Na(1)O_6-VO_6, wherein Na(1)O_6 polyhedra face share with MgO_6 /VO_6 octahedra. In the case of Na(2)O_8 polyhedra, these are found to be face sharing in MgO_6-Na(2)-MgO_6, VO_6-Na(2)-MgO_6 and VO_6-Na(2)-VO_6, and corner sharing in MgO_6-Na(2)-MgO_6 subunits. The calculations reveal that changing the local V/Mg ratio around Na species influences the energies of the configurations significantly, and thus plays a role in the preferred occupation of Na(1) and Na(2) sites across the $Na_{3+y}V_{2-y}Mg_y(PO_4)_3$ compositional series. In the lowest energy structures, both Na1(1) and Na(2) prefer to occupy Mg-rich environments rather than mixed V/Mg and V-rich environments. The most stable configurations for the $y = 0$, 0.25, 0.5, 0.75 and 1 phases have a Na(1): Na(2) occupation ratio of 0.66:0.77, 0.75:0.83, 0.83:0.89, 0.91:0.94 and 0.94:0.99, respectively, and are considered hereafter.

To understand how Mg^{2+} substitution influences Na^+ ion mobility in the NASICON framework, Na^+ diffusion barriers (E_a) and bottleneck sizes (T1) obtained for the series of $Na_{3+y}V_{2-y}Mg_y(PO_4)_3$ compositions are plotted in Figure 4.3b. The bottleneck area (T1) corresponds to the area of an isosceles triangle located in-between Na(1) and Na(2) sites.[24] T1 values obtained from first principles calculations at each Mg^{2+} substitution agree fairly well with those obtained from Rietveld analysis. While a drop in T1 is observed at low substitution levels ($y \leq 0.25$), this is followed by a steady increase in T1 upon further Mg^{2+} substitution. Activation energies were obtained from CI-NEB calculations for sodium-ion hops between Na(1) to Na(2) sites through the T1 area. While E_a and T1 may naively be expected to be inversely related to one another, the trend in E_a is more complex upon increasing the Mg^{2+} content. Indeed, E_a increases from ~0.15 eV at $y = 0$ to ~0.38 eV at $y = 0.25$, and stabilizes at about 0.25 eV for $y = 0.5$ and 0.75 compositions, before increasing again to 0.5 eV in the fully sodiated compound ($y = 1$). This complex evolution is likely the result of the interplay between changes to the T1 bottleneck area and to Na site occupation on Mg^{2+} substitution.

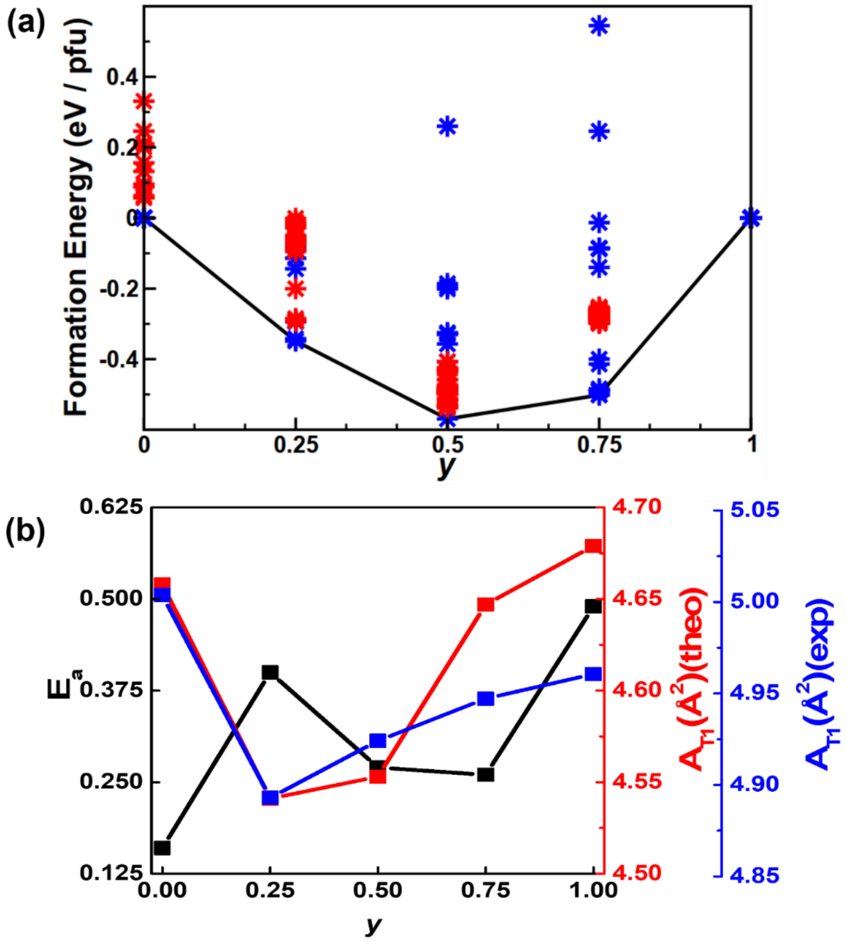

Figure 4.3. (a) Convex Hull Plot showing the formation energies for different orderings of V/Mg (blue asterisk) and Na(1)/Na(2) (red asterisk). (b) Na^+ ion diffusion barriers (E_a) and diffusion bottleneck sizes (T1) computed for the ground state V/Mg and Na(1)/Na(2) orderings are plotted as a function of y in $Na_{3+y}V_{2-y}Mg_y(PO_4)_3$.

Table 4.3. Effect of V/Mg interchange on Na(1) and Na(2) environments in the $Na_{3+y}V_{2-y}Mg_y(PO_4)_3$

$Na_{3+y}V_{2-y}Mg_y(PO_4)_3$	Na(1)-O (Å)	Na(1)-O (Å) - after V/Mg exchange	Na(2)-O (Å) Avg. bond length	Na(2)-O (Å). After V/Mg exchange
$y = 0.25$	2.400	2.391	2.732	2.544
$y = 0.5$	2.392	2.387	2.600	2.559
$y = 0.75$	2.400	2.393	2.610	2.577

Table 4.4. Lattice parameters and bond distances obtained from DFT calculations of $Na_{3+y}V_{2-y}Mn_y(PO_4)_3$ (in 1x1x1 conventional cell configurations).

$Na_{3+y}V_{2-y}Mg_y(PO_4)_3$	a (Å)	c (Å)	V-O (Å)	Na(1)-O (Å)	Na(2)-O (Å)
$y = 0$	8.865	21.48	2.00	2.405	2.53, 2.58, 2.90, 2.92
$y = 0.25$	8.868	21.465	2.01	2.400	2.51, 2.58, 2.91, 2.93
$y = 0.5$	8.872	21.444	2.04	2.39	2.45, 2.48, 2.55, 2.92
$y = 0.75$	8.871	21.452	2.06	2.40	2.48, 2.50, 2.55, 2.91
$y = 1$	8.883	21.392	2.07	2.38	2.45, 2.51, 2.93, 2.91

XAS experiments were performed on as-synthesized $Na_{3+y}V_{2-y}Mg_y(PO_4)_3$ ($0 \leq y \leq 1$) samples to investigate potential changes in the vanadium oxidation state, as well as local structure changes across the series. Normalized V K-edge absorption spectra are shown in Figure 4.2c. Irrespective of the amount of Mg^{2+} substituted into the NVP framework, the position of the absorption edge is similar in all XAS spectra, confirming that the average V oxidation state is +3 in all samples. Magnitude plots of the Fourier-transformed extended X-ray absorption fine structure (FT-EXAFS) at the V K-edge, along with theoretical fits and extrapolated bond distances, are shown in Figure 4.2d and Table 4.5, respectively. We note that the FT-EXAFS data are not phase-corrected and peak positions do not reflect actual bond lengths. The first peak located at ~1.6 Å corresponds to scattering from V-O pairs, while the next two peaks at ~2.8-3.2 Å are associated with V-P and V-Na outer shell correlations. Fits of the EXAFS spectra indicate a slight increase in the average V-O bond length on Mg^{2+} substitution, presumably due to reduced overlap between the V 3d orbitals and O 2p orbitals and enhanced bond ionicity. In contrast, the fits do not show any clear correlation between the evolution of the V-Na(1), V-P and V-Na(2) distances and the Mg^{2+} substitution level, yet significant changes are observed at each $\Delta y = 0.25$ step increase in Mg content. This may be explained by the concurrent increase in the total Na content and variations in the relative occupation of Na(1) and Na(2) sites upon Mg^{2+} substitution, resulting in a unique local structure for each composition.

Table 4.5. EXAFS parameters obtained from the fitting of $Na_{3+y}V_{2-y}Mg_y(PO_4)_3$ samples.

$Na_{3+y}V_{2-y}Mg_y(PO_4)_3$	Co-ordination shell	Distances between atoms (r±Δr) (Å)	S_0^2	σ^2(Å^2)
$y = 0$	**V-O×3**	1.992 +0.071	0.76	0.00904
	V-O×3	1.926+0.096		0.00860
	V-P×6	3.399-0.069		0.03806
	V-Na(1)×3	3.137+0.019		0.01339
	V-Na(2)×3	3.845-0.013		0.01905
$y = 0.25$	**V-O×3**	2.003 -0.013	0.82	0.00764
	V-O×3	1.947+ 0.018		0.00468
	V-P×6	3.148+ 0.011		0.04588
	V-Na(1)×3	3.409+ 0.058		0.00511
	V-Na(2)×3	3.846+0.058		0.00979
$y = 0.5$	**V-O×3**	2.000 +0.019	0.87	0.00088
	V-O×3	1.961+0.043		0.00272
	V-P×6	3.411+ 0.012		0.00091
	V-Na(1)×3	3.151+ 0.087		0.01054

	V-Na(2)×3	3.856-0.038		0.00409
***y* = 0.75**	**V-O×3**	2.003 -0.011	0.89	0.00168
	V-O×3	1.990+0.023		0.00184
	V-P×6	3.413+ 0.017		0.001191
	V-Na(1)×3	3.156+ 0.019		0.00072
	V-Na(2)×3	3.857+ 0.082		0.00478
***y* = 1**	**V-O×3**	2.024+ 0.069	0.83	0.00389
	V-O×3	2.009+0.0167		0.00618
	V-P×6	3.444+ 0.023		0.00050
	V-Na(1)×3	3.189+ 0.0919		0.00982
	V-Na(2)×3	3.891- 0.0355		0.0297

^{23}Na and ^{31}P solid-state nuclear magnetic resonance (NMR) experiments were conducted (in collaboration with Dr. R. J. Clément's group from University of California Santa Barbara) to obtain further insights into local structure changes across the $Na_{3+y}V_{2-y}Mg_y(PO_4)_3$ series. The presence of open-shell V^{3+} species in these compounds results in strong hyperfine (or paramagnetic) interactions between unpaired electron spins nominally present in the V *3d* orbitals and the ^{23}Na / ^{31}P nuclear spins under study. These strong interactions result in significant NMR line broadening and potential signal overlap, complicating the assignment of the spectral features to specific local environments in the material. Furthermore, the isotropic chemical shift (δ_{iso}) is dominated by the Fermi contact shift resulting from delocalization of unpaired electron spin density from the V *3d* orbitals to the ^{23}Na (or ^{31}P) *s* orbitals via bridging O *2p* orbitals. For an $I = 3/2$ quadrupolar nucleus such as ^{23}Na, the interaction between the nuclear quadrupole moment and the electric field gradient (EFG) present at the nucleus leads to a further broadening of the spectrum and to a shift of the ^{23}Na resonant frequency due to second-order effects (denoted δ_Q). The observed chemical shift (δ_{obs}) is then the sum of the isotropic Fermi contact shift and of the second-order quadrupolar shift: $\delta_{obs} = \delta_{iso} + \delta_Q$. In contrast, ^{31}P is a spin-½ nucleus with no quadrupole moment and $\delta_{obs} = \delta_{iso}$.

^{23}Na spin echo NMR spectra obtained at 18.8 T are shown in Figure 4.4a. As expected from the reduced hyperfine interactions upon progressive replacement of paramagnetic V^{3+} by diamagnetic Mg^{2+}, a decrease in signal broadening is observed as *y* increases.[25] A shift of the average ^{23}Na resonant frequency towards 0 ppm is also observed on increasing the Mg^{2+} content, again, as expected from the reduced paramagnetism.

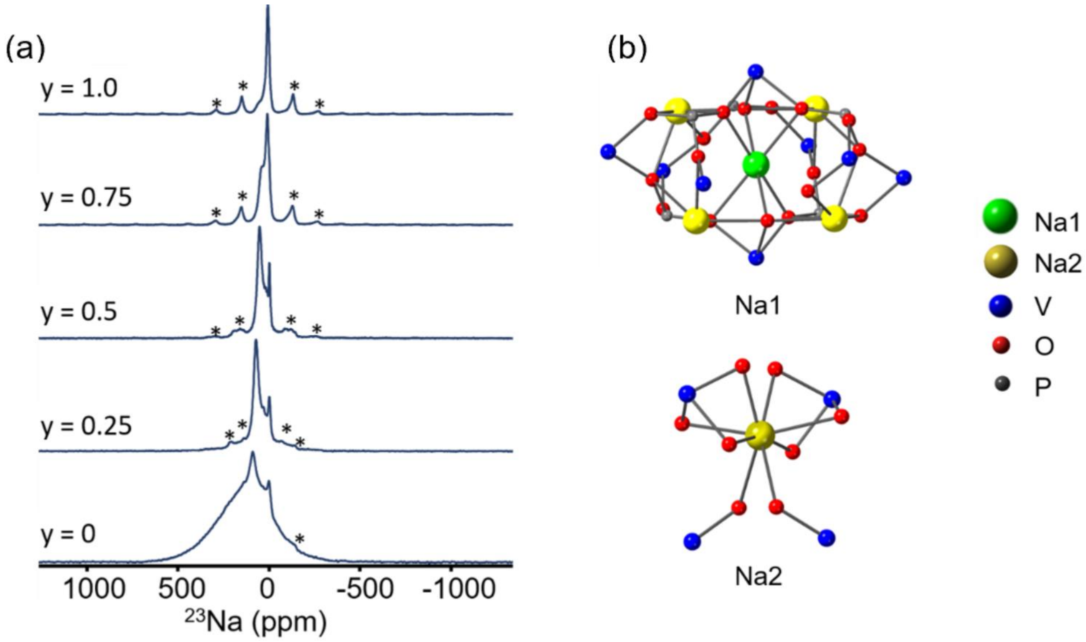

Figure 4.4. (a) ^{23}Na solid-state NMR spectra obtained on as-synthesized $Na_{3+y}V_{2-y}Mg_y(PO_4)_3$ at 18.8 T using a spin echo pulse sequence. (b) Local environments Na(1) (surrounded by 8 V atoms) and Na(2) (surrounded by 4 V atoms) in the $Na_3V_2(PO_4)_3$ structure.

For the Mg-substituted samples, the assignment of the ^{23}Na NMR resonances to specific sites in the NASICON structure is not straightforward. Assuming that Mg randomly substitutes on V sites, a large number of Na local environments are expected with varying numbers of Mg^{2+} species in the first metal coordination shell around Na(1) and Na(2) depicted in Figure 4.4b, resulting in a distribution of chemical shifts. For example, in the $y = 0.5$ sample, a total of 35 distinct Na(1) environments and 6 distinct Na(2) environments are expected. However, only two to three ^{23}Na resonances are observed in the NMR spectra collected on these phases (see Figure 4.4), suggesting that fast chemical exchange between subsets of Na(1) and Na(2) sites in these compounds results in ^{23}Na NMR signal averaging. Additionally, while we assign the sharp ^{23}Na resonance near 0 ppm in the y = 0.25 and 0.5 samples to diamagnetic sodium phosphate / pyrophosphate impurity(ies), the broader resonances in this frequency range in the y = 0.75 and 1 samples likely have contributions from Na sites in the paramagnetic NASICON cathode primarily surrounded by diamagnetic Mg^{2+} species.

^{31}P solid-state NMR experiments were conducted to monitor the evolution of the P local environments across the $Na_{3+y}V_{2-y}Mg_y(PO_4)_3$ series (Figure 4.5). Spectral regions featuring paramagnetic ^{31}P NMR signals arising from the NASICON cathodes are shown in Figure 4.5a, and an example P local environment in NVP is provided in Figure 4.5b.

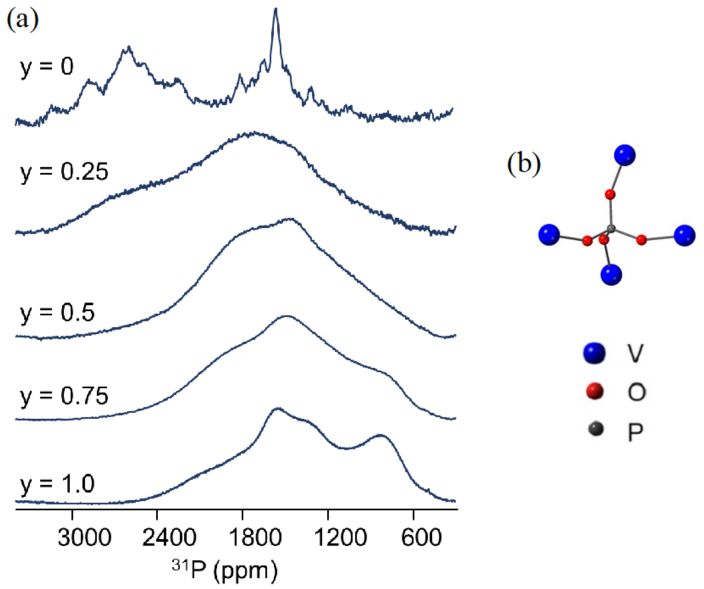

Figure 4.5. (a) Enlargements of the paramagnetic region of ^{31}P variable offset cumulative spectroscopy (VOCS) NMR spectra obtained on pristine $Na_{3+y}V_{2-y}Mg_y(PO_4)_3$ cathode samples at 7.05 T and at a spinning speed of 30 kHz. The full VOCS spectra are shown in Figure 4.6. (b) Example P local environment in $Na_3V_2(PO_4)_3$.

As shown in Figure 4.5a, ^{31}P spectra collected on $Na_{3+y}V_{2-y}Mg_y(PO_4)_3$ pristine compounds are significantly broadened and feature multiple overlapping signals spanning a chemical shift range on the order of thousands of ppm. As the Mg dopant concentration is increased from y = 0.25 to y = 1, the reduced hyperfine interactions result in a decrease of the

^{31}P NMR signal broadening and concomitant shift of the resonant frequencies towards 0 ppm. For the $y = 0$ compound, we see multiple ^{31}P resonances suggesting the presence of multiple local ^{31}P environments in the material. This result is inconsistent with the rhombohedral ($R\bar{3}c$) model of $Na_3V_2(PO_4)_3$,[23] which contains a single P environment, and confirms the presence of a monoclinic structural distortion due to Na^+-ion/vacancy ordering close to room temperature.

Although paramagnetic interactions are reduced on Mg^{2+} substitution into $Na_{3+y}V_{2-y}Mg_y(PO_4)_3$, the $y = 0.25$ spectrum is broader than the $y = 0$ spectrum. The broader line shape can be accounted for by the presence of a broad distribution of chemical shifts reflecting a distribution of P local environments as Mg partially substitutes on the V sites. As the Mg concentration is increased beyond $y = 0.25$, the paramagnetic broadening is decreased but the distribution of ^{31}P environments is still present. Assuming a random substitution of V by Mg, we expect 16 distinct P environments in the rhombohedral ($R\bar{3}c$) Mg-substituted compounds; the probability of finding each of these 16 P sites depends on the exact Mg : V ratio. Full ^{31}P NMR spectra (from -2000 to 4000 ppm) collected on all samples are shown in Figure 4.6, and exhibit additional resonances near 0 ppm attributed to diamagnetic phosphate / pyrophosphate impurities [26,27] and/or to ^{31}P sites in the NASICON structure surrounded by four diamagnetic Mg^{2+} ions. For instance, assuming a statistical distribution of V and Mg species in the $y = 1$ composition, the probability of finding a ^{31}P nucleus surrounded only by 4 Mg is 6.25%.

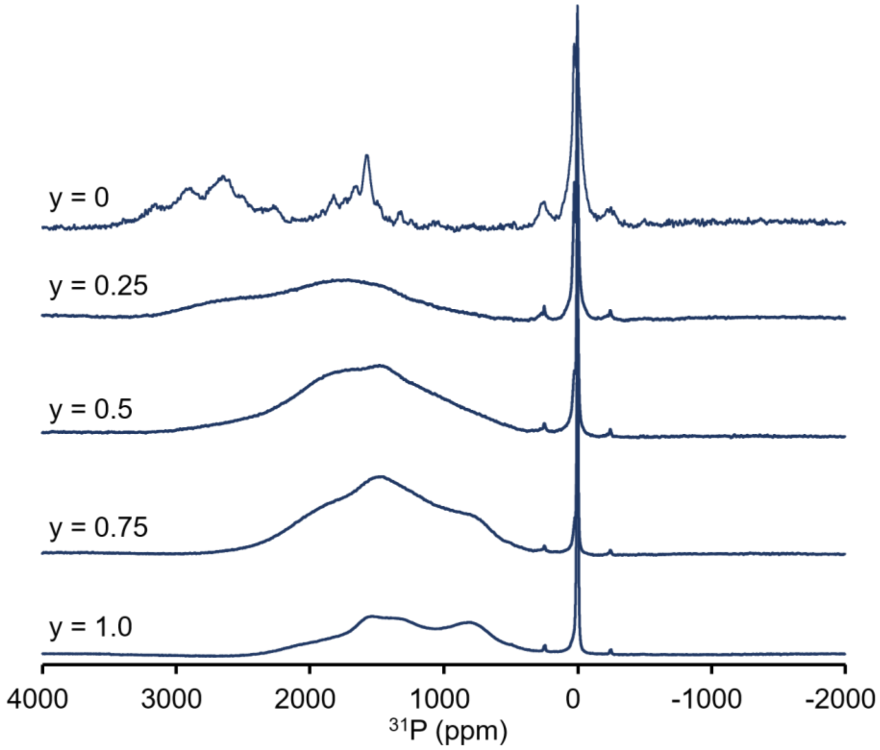

Figure 4.6. Full ^{31}P VOCS NMR spectra obtained on the series of pristine $Na_{3+y}V_{2-y}Mg_y(PO_4)_3$ cathode samples at 7.05 T and at a spinning speed of 30 kHz. While resonances due to ^{31}P nuclei in the paramagnetic NASICON cathode appear above ~200 ppm, signals near 0 ppm correspond to diamagnetic impurities, likely including Na_2HPO_4.

Having established how Mg^{2+} substitution for V^{3+} in $Na_{3+y}V_{2-y}Mg_y(PO_4)_3$ cathodes affects their (local) crystal structure and Na^+ ion diffusion properties, we move on to study their Na (de)intercalation properties through galvanostatic cycling at a C/10 rate in the voltage window of 3.8-2.75 V *vs*. Na^+/Na^0. The voltage-composition (x) profiles of the $Na_{3+y}V_{2-y}Mg_y(PO_4)_3$ cathodes from their second cycle are given in Figure 4.7a, and their cycling stability evaluated at C/10 rate, is shown in Figure 4.7b. Remarkably, all of the NASICON cathodes retain almost 99% of their initial discharge capacities at the end of 50th cycle. The $Na_3V_2(PO_4)_3$ cathode exhibits a flat charge/discharge profile with an average voltage of ~3.45 V *vs*. Na^+/Na^0, corresponding to the reversible exchange of 1.9 moles of Na *pfu*.[6,9] The large voltage plateau indicates that Na (de)intercalation proceeds *via* a two-phase reaction between the $Na_3V_2(PO_4)_3$ and $NaV_2(PO_4)_3$ end-member compositions. Compared to NVP, several changes in the electrochemical properties are observed as y increases: the amount of reversible Na exchange decreases (to 1.7, 1.43, 1.13 and 1.0 moles *pfu* for $y = 0.25$, 0.5, 0.75 and 1, respectively), the slope of the voltage-composition profiles increases, and the average intercalation voltage increases.

The decrease in the amount of cyclable Na (i.e., the charge storage capacity) with increasing y is related to the replacement of redox-active V^{3+} by electrochemically-inactive Mg^{2+} cations. The evolution of the average sodium (de)intercalation voltage and mechanism is best characterized *via* dQ/dV plots, as shown in Figure 4.7c and 4.7d. Changes to the average (de)intercalation potential (Figure 4.7d), from ~3.38 V at $y = 0$ to ~3.49 V at $y = 1$, can be attributed to variations in the V-O bonding character across the $Na_{3+y}V_{2-y}Mg_y(PO_4)_3$ series. Specifically, substitution of more electropositive Mg^{2+} ions for V^{3+} ions in the structure is expected to increase the ionicity of V-O bonds, thus raising the (de)intercalation voltage of the V^{4+}/V^{3+} redox couple. To confirm this, we computed the projected Density of States (pDOS) for all members of the $Na_{3+y}V_{2-y}Mg_y(PO_4)_3$ series (Figure 4.8a and b). We find that, while the valence states are majorly comprised by O-2p and Mg-2s orbitals, the V-3d orbitals dominate the higher energy conduction band states. The density of both V-3d and O-2p orbitals that are located near and below the Fermi level, respectively, decreases with increasing concentration of dopant Mg atoms, indicating a weakening of the hybridization between V and O orbitals due to the more polarizing nature of Mg^{2+}. This leads to a gradual reduction in the V-O bond covalency and to a lowering of the V-O* antibonding states, which in turn increases the V^{4+}/V^{3+} redox voltage. The pDOS results are confirmed by Bader charge analysis, which indicates an increase in the ionicity of V-O bonds and higher Bader charges on the V cations with increasing Mg content[28] (Figure 4.8c). The redox peaks in the dQ/dV plots in Figure 4.7c also become broader as y increases from 0 to 1, indicating a change in the Na (de)intercalation process upon Mg^{2+} substitution.

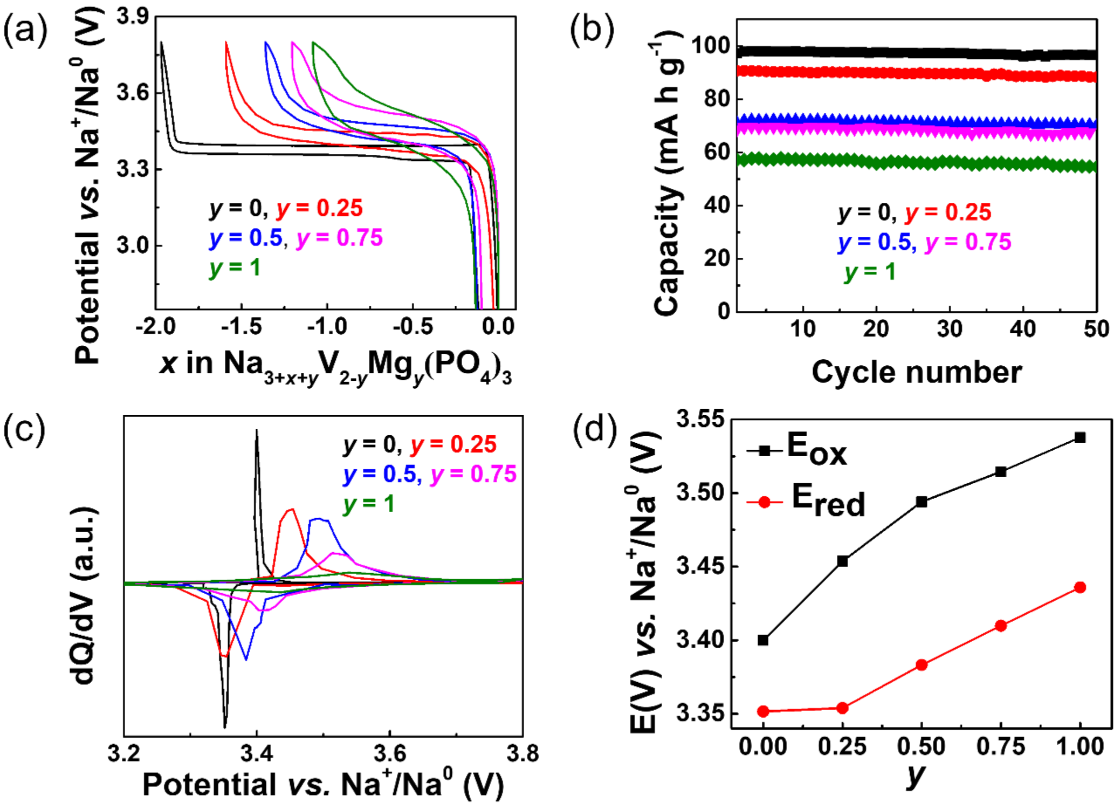

Figure 4.7. (a) Voltage *vs*. composition (x), (b) cycling performance, (c) dQ/dV profiles and (d) evolution of oxidation/reduction voltages (deduced from dQ/dV plots) of the $Na_{3+y}V_{2-y}Mg_y(PO_4)_3$ cathodes.

To understand how Mg^{2+} substitution affects the Na (de)intercalation mechanism of the NVP cathode, we performed *in-operando* XRD studies on the $y = 0.5$ and 1 cathodes (Figure 4.9). Previous *in-operando* XRD studies on the unsubstituted NVP cathode have revealed a complete two-phase transformation mechanism between the $Na_3V_2(PO_4)_3$ and $NaV_2(PO_4)_3$ end-members, accompanied by the oxidation of V^{3+} to V^{4+}.[29] During the initial charge process, the XRD peaks of the $Na_{3.5}V_{1.5}Mg_{0.5}(PO_4)_3$ cathode progressively shift towards higher 2θ angles until 0.5 Na *pfu* has been extracted to form an intermediate $Na_3V_{1.5}Mg_{0.5}(PO_4)_3$, indicating a solid solution mechanism over this compositional range (Figure 4.9a). As the cathode is charged further, the XRD peaks of the $Na_3V_{1.5}Mg_{0.5}(PO_4)_3$ phase diminish whilst a new set of XRD peaks appears and grows at 2θ = 20.65° and 24.11°, confirming a first order phase transformation in this range. The XRD pattern collected at the end of charge (3.8 V *vs*.

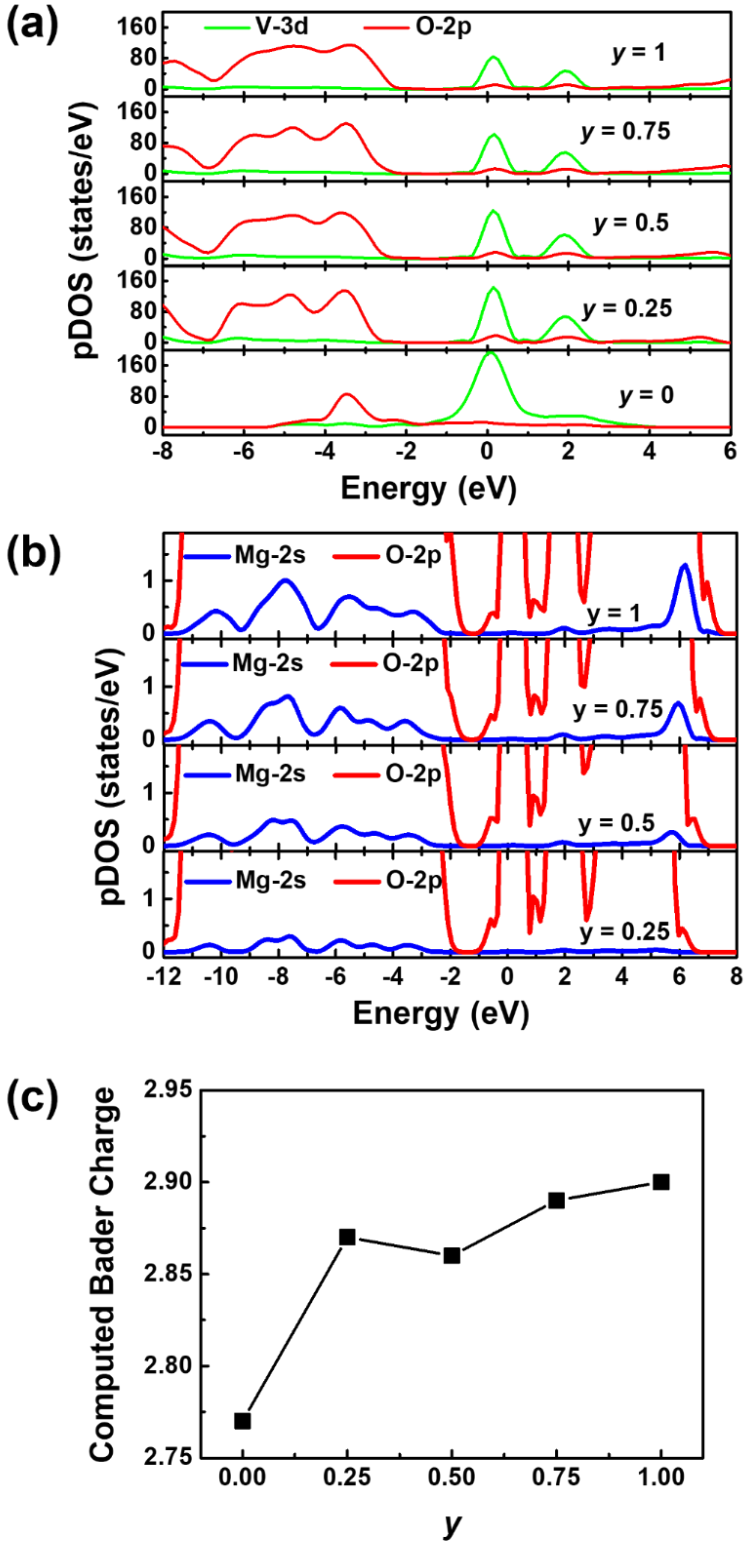

Figure 4.8. Calculated (a) and (b) pDOS, and (c) Bader charges on vanadium in the $Na_{3+y}V_{2-y}Mg_y(PO_4)_3$ cathodes as a function of *y*.

Na^+/Na^0) can be fitted with two NASICON phases (Figure 4.9b) and their corresponding lattice parameters are displayed in Table 4.6. The overall cell volume change between the Na-rich and Na-poor phases is estimated as 6.2 %, which is lower compared to the NVP cathode ($\Delta V/V$ = 8.1 %). It is worth mentioning here that the presence of unextracted Na-ions in the Mg-substituted phases increases their volume and reduces the volume mismatch between Na-rich and Na-poor phases, resulting in enhanced structural integrity during cycling. Upon subsequent discharge, all of the processes observed on charge are reversed, and the XRD pattern collected at the end of the first cycle matches that of the pristine $Na_{3.5}V_{1.5}Mg_{0.5}(PO_4)_3$ cathode perfectly, thus confirming full reversibility of the Na (de)intercalation mechanism. In contrast, the fully sodiated $Na_4VMg(PO_4)_3$ cathode exhibits a solid solution mechanism over the entire Na (de)intercalation range (Figure 4.9c). Its XRD peaks shift towards higher and lower 2θ values during the charge and discharge process, respectively. The desodiated $Na_3VMg(PO_4)_3$ phase observed at 3.8 V *vs*. Na^+/Na^0 shows anisotropic lattice parameter changes (i.e., a decrease and an increase in the *a*- and *c*- lattice parameter, respectively) (see Figure 4.9d and Table 4.6). The increase in *c*-parameter can be correlated to the removal of sodium ions from Na(1) site. This observation is in contrast with the desodiation processes of $Na_3V_2(PO_4)_3$ and $Na_4VMn(PO_4)_3$[17,30] cathodes wherein Na-ions from Na(1) site are not involved in the desodiation process until 3.8 V *vs*. Na^+/Na^0. Thus, it is clear that Mg-substitution affects the preference of sodium ion extraction from Na(1) and Na(2) sites, which could be due to the differences in site energies among the various local environments ($(V/Mg)O_6$-$(Na(1)O_6/Na(2)O_8)$-$(V/Mg)O_6$) as described in the earlier section. Detailed theoretical calculations are underway to decipher about it. Overall, the *in-operando* XRD results prove that the Na (de)intercalation mechanism of Mg-substituted $Na_{3+y}V_{2-y}Mg_y(PO_4)_3$ cathodes progressively changes from a two-phase process to a solid solution process as the Mg content increases in the NVP lattice. Similar behavior has also been noticed in the case of $Na_{3+y}V_{2-y}Mn_y(PO_4)_3$ cathodes.[31]

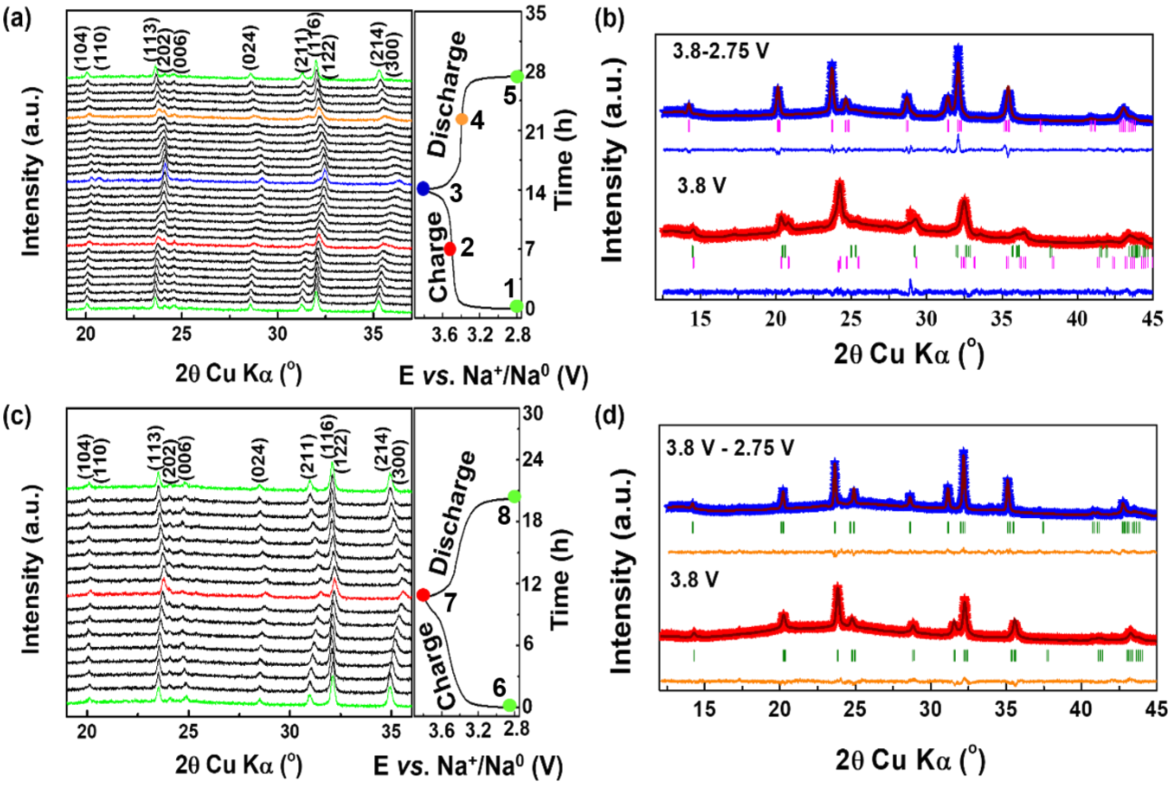

Figure 4.9. *In-operando* XRD (a, c) and *ex-situ* pattern refinements of (b, d) of $y = 0.5$ and 1 cathodes collected in the voltage window of 3.8-2.75 V *vs.* Na^+/Na^0.

Table 4.6. Refined cell parameters and unit cell volumes of *ex-situ* $Na_{3+y}V_{2-y}Mg_y(PO_4)_3$ (y = 0.5 and 1.0) cathodes cycled in the window of 3.8-2.75 V *vs.* Na^+/Na^0.

y = 0.5			
Pattern No.	***a* (Å)**	***c* (Å)**	**V ($Å^3$)**
1	8.80669	21.6716	1455.62
3	8.5278(13)	21.634(4)	1362.5(4)
	8.620(2)	21.389(6)	1376.4(6)
5	8.7774(6)	21.672(2)	1446.0
y = 1			

6	8.8514(11)	21.487(3)	1457.9(3)
7	8.7391(10)	21.563(3)	1426.2(3)
8	8.8524(5)	21.4540(14)	1456.00(15)

To understand the origin of the increased voltage polarization at higher Mg^{2+} substitution levels, GITT experiments were performed (Figure 4.10a-c). We also recall here the theoretical calculation results presented earlier to correlate the Mg-substitution to the kinetic behaviors of the $Na_{3+y}V_{2-y}Mg_y(PO_4)_3$ cathodes. Although we cannot establish a direct correlation between the bottleneck sizes and the Na diffusion barrier (E_a), the latter increases for all of the Mg-substituted cathodes as compared to the NVP. Therefore, we expect an increase in the voltage hysteresis upon Mg substitution. However, we find that the charge-discharge voltage hysteresis initially decreases from $y = 0$ to $y = 0.25$ and 0.5, followed by an increase for the $y = 0.75$ and 1 compounds. The voltage-composition profiles obtained from GITT and galvanostatic cycling experiments are compared in Figure 4.11. For the $y = 0.25$ and 0.5 compositions, polarization is drastically reduced or completely vanishes when the voltage is allowed to relax to its equilibrium value (as in the GITT measurement), which is not the case for the $y = 0.75$ and 1 cathodes. The lowest polarization observed for $y = 0.5$ cathode can be attributed to reduced lattice mismatch between the Na-rich and Na-poor end members of the two-phase reaction, as demonstrated by the *operando* XRD results. Such a phenomenon has been observed in, *e.g.*, related Li(Fe/Mn)PO_4 cathodes.[32-34] The impact of Mg-substitution on the Na (de)intercalation mechanism and kinetics is reflected in the rate performance of the $Na_{3+y}V_{2-y}Mg_y(PO_4)_3$, shown in Figure 4.10d. The $y = 0.25$, 0.5 & 0.75 cathodes deliver similar capacities as the $y = 0$ cathode at 1C and 2C rates, in contrast, the capacity of the $y = 1$ end member declines significantly at these high C-rates. These results highlight that two-phase Na (de)intercalation phenomena is not deleterious for high-rate performance and in fact lower voltage hysteresis can be achieved at intermediate Mg^{2+} substitution levels.

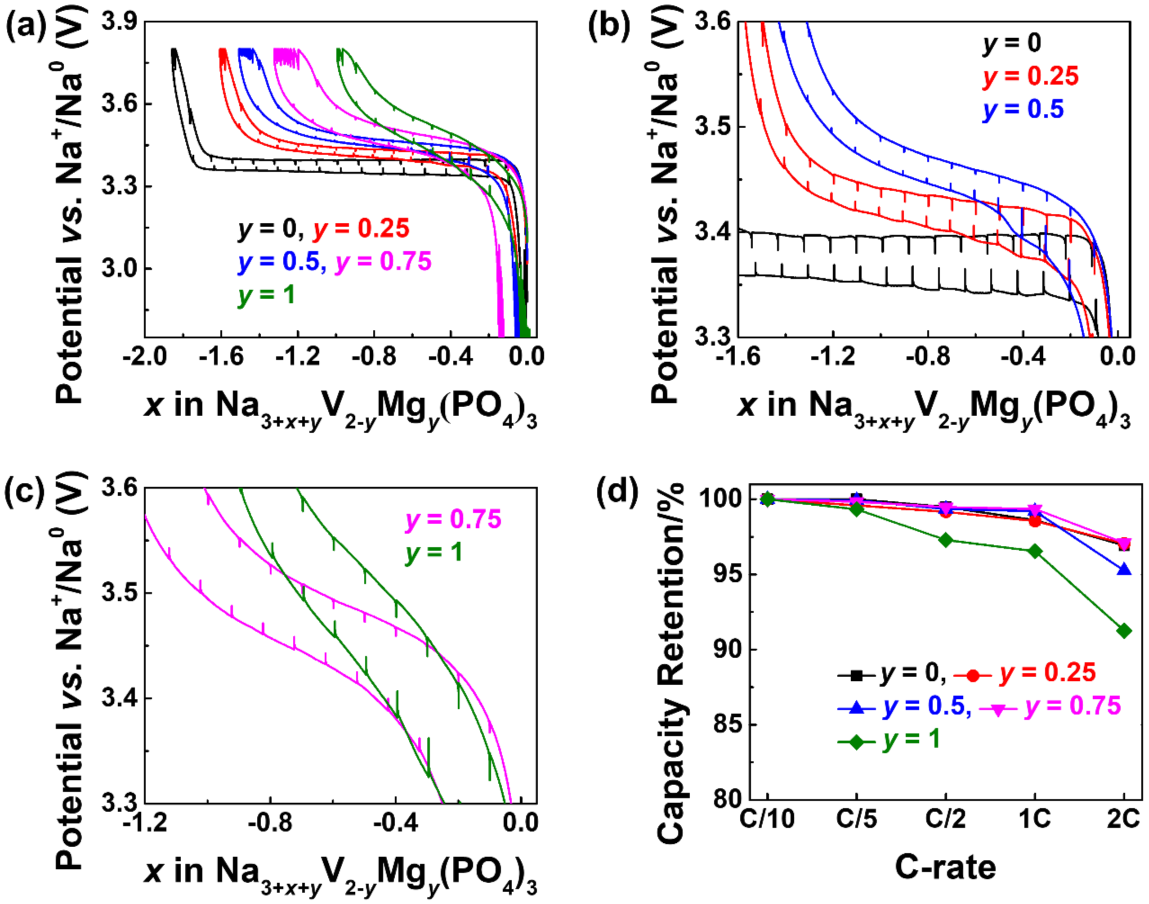

Figure 4.10. (a) GITT profiles of $Na_{3+y}V_{2-y}Mg_y(PO_4)_3$ cathodes and (b) and (c) their enlarged views. (d) Rate capability profiles of the $Na_{3+y}V_{2-y}Mg_y(PO_4)_3$ cathodes.

Further, we have expanded our galvanostatic cycling studies of $Na_{3+y}V_{2-y}Mg_y(PO_4)_3$ cathodes to high voltage region (4.2-2.75 V *vs*. Na^+/Na^0) (Figure 4.12). Upon cycling at C/10 rate, no additional redox feature is observed for the unsubstituted cathode compared to its low voltage window (3.8-2.75 V *vs*. Na^+/Na^0) cycling. The first charge voltage profiles of Mg-substituted cathodes enlist an additional voltage feature at ~ 3.9 V *vs*. Na^+/Na^0 due to the operation of V^{5+}/V^{4+} couple, besides the low voltage V^{4+}/V^{3+} step. Accordingly, the sodium deintercalation capacities of $y = 0.25$, 0.5, 0.75 and 1 cathodes increase to 1.74, 1.97, 1.83 and 1.76 moles of sodium ions pfu, respectively, compared to their low voltage window charge capacities. Interestingly, on the subsequent discharge, the Mg-substituted cathodes display S-shaped voltage profiles. These changes can be better visualized from the corresponding dQ/dV profiles. The charge dQ/dV profiles of Mg-substituted cathodes contain two oxidation peaks at ~3.4-3.6 and 3.9 V *vs*. Na^+/Na^0, corresponding to the activities of V^{4+}/V^{3+} and V^{5+}/V^{4+} couples, respectively (Figure 4.12b). However, the discharge dQ/dV profiles exhibit a broad voltage feature at 3.4-3.5 V *vs*. Na^+/Na^0, which could be tentatively ascribed to the mixed $V^{5+}/V^{4+}/V^{3+}$ activity. From the 2nd cycle onwards, the Mg-substituted cathodes display S-shaped charge-discharge voltage profiles (Figure 4.12c). The cycling stabilities of $Na_{3+y}V_{2-y}Mg_y(PO_4)_3$ cathodes were assessed at C/10 rate in the window of 4.2-2.75 V *vs*. Na^+/Na^0. At the end of 30th cycle, the $y = 0.25$, 0.5, 0.75 and 1 cathodes delivered discharge capacities of 76, 70, 54 and 42 mA h g^{-1}, respectively (Figure 4.12d).

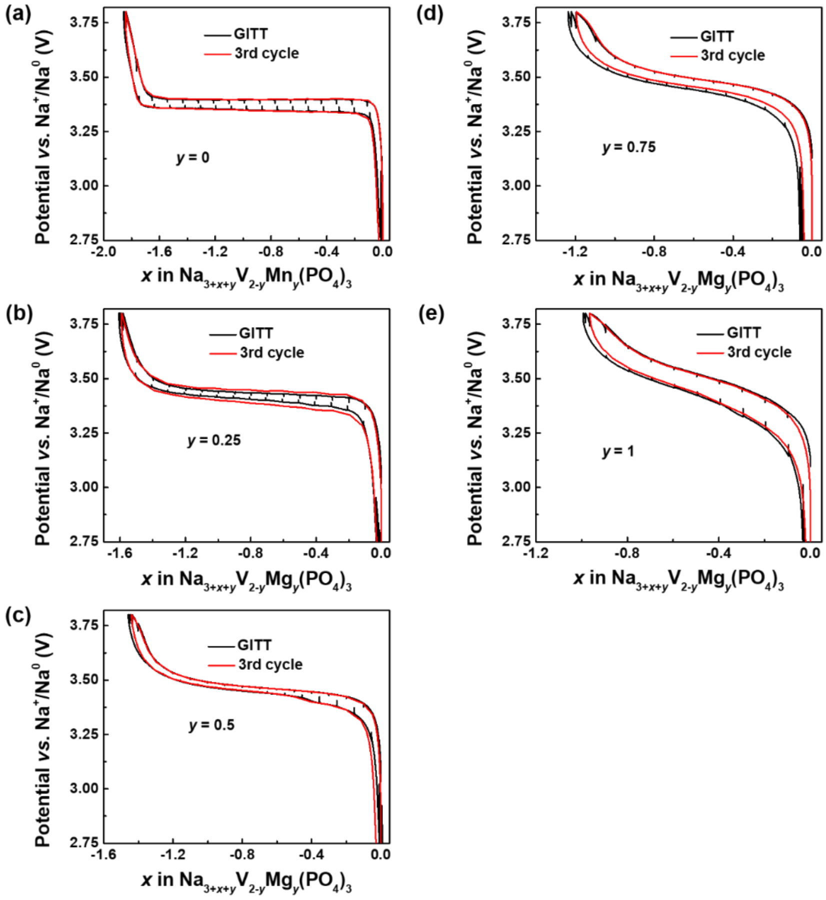

Figure 4.11. Comparison of voltage vs. composition profiles of $Na_{3+y}V_{2-y}Mg_y(PO_4)_3$ cathodes obtained from galvanostatic cycling (C/10 rate) and GITT protocols.

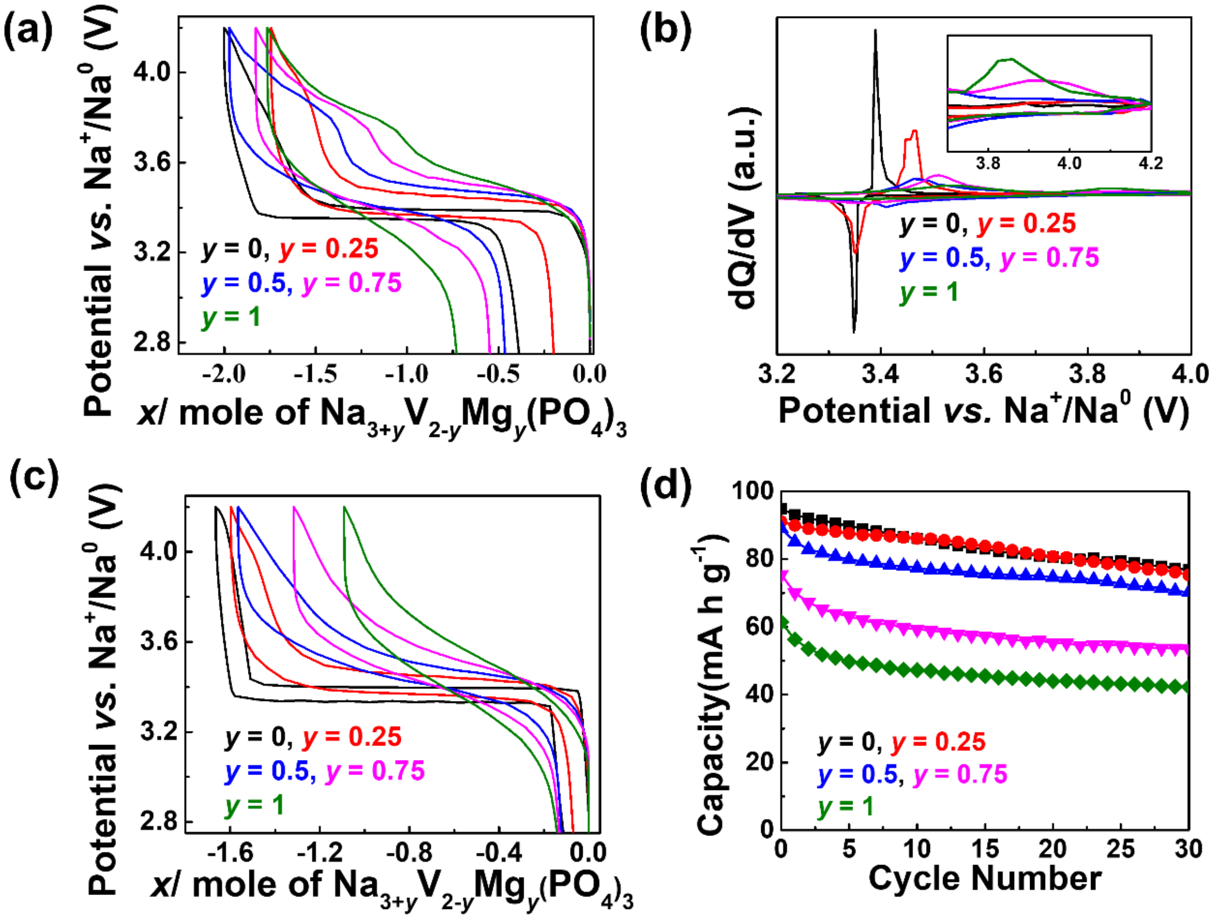

Figure 4.12. (a) First cycle voltage vs. composition (*x*), (b) dQ/dV profiles, (c) second cycle voltage *vs*. composition and (d) cycling performance of the $Na_{3+y}V_{2-y}Mg_y(PO_4)_3$ cathodes.

The aforementioned changes in the electrochemical signatures of $Na_{3+y}V_{2-y}Mg_y(PO_4)_3$ cathodes indicate possible structural transformation during their high voltage cycling. To better understand about it, we performed *in-situ* XRD measurements on the $y = 0.5$ and 1 cathodes in the window of 4.2-2.75 V *vs*. Na^+/Na^0 at C/10 rate (Figure 4.13). The calculated cell parameters of selected XRD patterns are given in Table 4.7. During the first charge, the $y = 0.5$ cathode displays a solid solution mechanism followed by a two-phase phenomena until 3.8 V *vs*. Na^+/Na^0 as described above. Afterward, its desodiation reaction proceeds *via* a solid solution process until 4.2 V *vs*. Na^+/Na^0. On the subsequent discharge, the y = 0.5 cathode exhibits a complete solid solution behavior. Similar Na (de)intercalation phenomena is also observed for the y = 1 cathode upon cycling in the 4.2-2.75 V *vs*. Na^+/Na^0 region. Its desodiated phase

(“$Na_{2.25}VMg(PO_4)_3$”) collected at 4.2 V *vs.* Na^+/Na^0 shows enhanced anisotropic changes of cell parameters compared to $Na_3VMg(PO_4)_3$ intermediate collected at 3.8 V *vs.* Na^+/Na^0, implying more amount of Na-ion removal from Na(1) site. Most importantly, the XRD patterns of cycled $y = 0.5$ and 1 cathodes collected at 2.75 V *vs.* Na^+/Na^0do not exactly match with their pristine state, thus proving bulk structural degradation upon cycling at higher voltages.

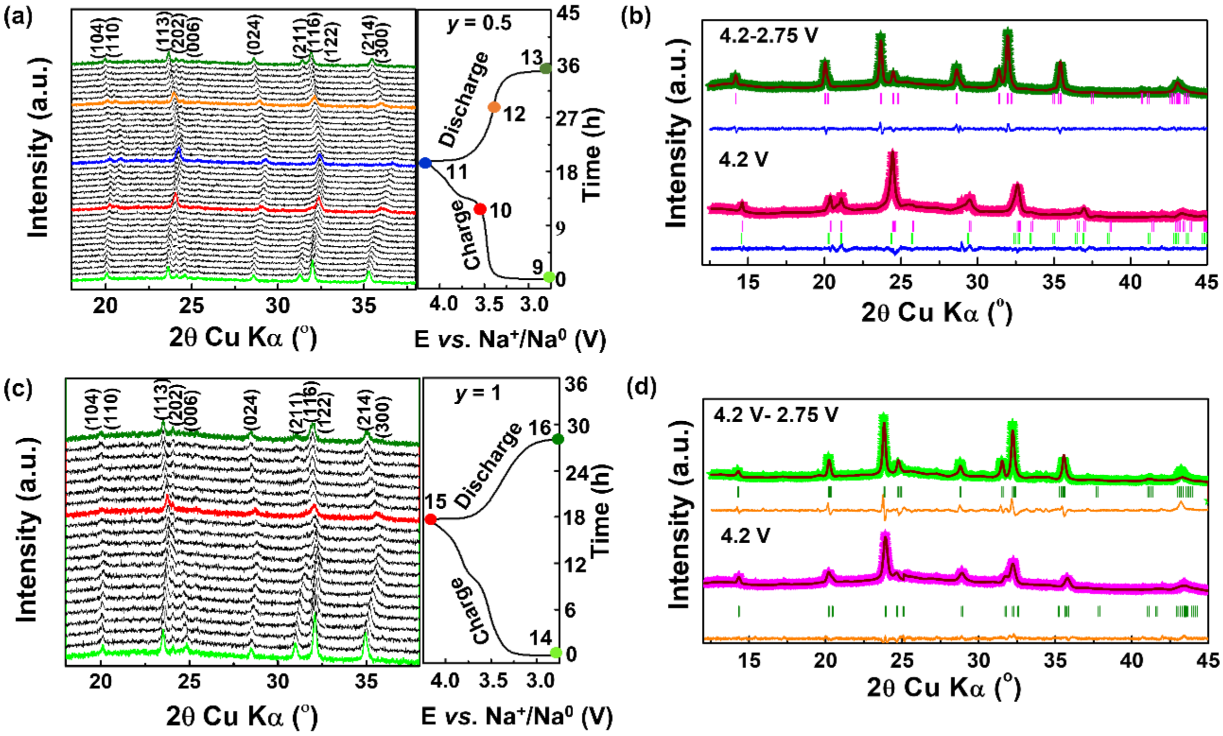

Figure 4.13. *In-operando* XRD (a, c) and *ex-situ* pattern refinements of (b, d) of $y = 0.5$ and 1 cathodes collected in the voltage window of 4.2-2.75 V *vs.* Na^+/Na^0.

Table 4.7. Refined cell parameters and unit cell volumes of *ex-situ* $Na_{3+y}V_{2-y}Mg_y(PO_4)_3$ (y = 0.5 and 1.0) cathodes cycled in the window of 4.2-2.75 V *vs.* Na^+/Na^0.

***y* = 0.5**			
Pattern No.	***a* (Å)**	***c* (Å)**	**V (Å^3)**
9	8.80669	21.6716	1455.62
11	8.4196(13)	21.728(5)	1333.9(4)
	8.436(2)	21.930(12)	1351.7(9)

13	8.77818(17)	21.8075(6)	8.77818(17)
***y* = 1**			
14	8.8514(11)	21.487(3)	1457.9(3)
15	8.6881(13)	21.673(3)	1416.7(4)
16	8.7483(9)	21.602(3)	1431.8(3)

4.4. Conclusions

In this work, the impact of Mg^{2+} substitution on the structural and electrochemical Na (de)intercalation properties of $Na_{3+y}V_{2-y}Mg_y(PO_4)_3$ cathodes was investigated. Our combined XRD, XAS, NMR, and first principles results revealed a complex evolution of the (local) structure upon progressive replacement of V^{3+} by Mg^{2+}, along with the addition of Na ions into Na(1)/Na(2) sites, resulting in non-linear changes in the Na^+ diffusion properties across the compositional series. When cycled in the voltage window of 3.8-2.75 V *vs*. Na^+/Na^0, significant differences in the voltage-capacity profiles of the $Na_{3+y}V_{2-y}Mg_y(PO_4)_3$ cathodes were observed, including discrepancies in the average intercalation voltage, in the shape of the voltage curves and in their polarization. The increased Na insertion voltage on Mg substitution was attributed to more ionic V-O bond, as determined from pDOS and Bader charge analyses. A transition from a two-phase for $y \leq 0.5$ to a solid solution process on Na (de)intercalation for $y \geq 0.5$ was confirmed through *in-operando* XRD measurements. The lowest polarization value obtained for the $y = 0.5$ cathode was ascribed to minimized lattice mismatch between the Na-rich and Na-poor end members of the two-phase reaction. Upon extending the voltage window to 4.2-2.75 V *vs*. Na^+/Na^0, the Mg-substituted cathodes showed enhanced desodiation capacities due to additional V^{5+}/V^{4+} redox activity. However, it triggered irreversible structural transformation of the NASICON cathodes upon simultaneous oxidation of V^{4+} to V^{5+} and Na-ion removal from Na(1). Further experimental and theoretical studies are in progress to better understand the high voltage behavior of the $Na_{3+y}V_{2-y}Mg_y(PO_4)_3$ cathodes. Overall, the present work underlines the importance of tunning functionalities of cathodes and understanding their structure-property relationship upon cationic substitution to achieve high energy density NASICON cathodes.

Referrences

[1] Z. Yang, J. Zhang, M. C. W. Kintner-Meyer, X. Lu, D. Choi, J. P. Lemmon, J. Liu, *Chem. Rev*. **2011**, *111*, 3577.

[2] J-Y. Hwang, S-T. Myung, Y-K. Sun, *Chem. Soc. Rev*. **2017**, *46*, 3529.

[3] S. Chen, C. Wu, L. Shen, C. Zhu, Y. Huang, K. Xi, J. Maier, Y. Yu, *Adv. Mater.* **2017**, *29*, 1700431.

[4] J. B. Goodenough, H. Y-P. Hong, J. A. Kafalas, *Mater. Res. Bull*. **1976**, *11*, 203.

[5] C. Delmas, F. Cherkaoui, A. Nadiri, P. Hagenmuller, *Mater. Res. Bull.* **1987**, *22*, 631.

[6] S. Y. Lim, H. Kim, R. A. Shakoor, Y. Jung, J. W. Choi, *J. Electrochem. Soc.* **2012**, *159*, A1393.

[7] K. Kawai, W. Zhao, S-i. Nishimura, A. Yamada, *ACS Appl. Energy Mater.* **2018**, *1*, 928.

[8] R. Rajagopalan, B. Chen, Z. Zhang, X-L. Wu, Y. Du, Y. Huang, B. Li, Y. Zong, J. Wang, G-H. Nam, M. Sindoro, S. X. Dou, H. K. Liu, H. Zhang, *Adv. Mater*. **2017**, *29,* 1605694.

[9] W. Song, X. Ji, Z. Wu, Y. Zhu, Y. Yang, J. Chen, M. Jing, F. Li, C. E. Banks, *J. Mater. Chem. A* **2014**, *2*, 5358.

[10] M. J. Aragón, P. Lavela, G. F. Ortiz, J. L. Tirado, *ChemElectroChem*. 2015, *2*, 995.

[11] A. Inoishi, Y. Yoshioka, L. Zhao, A. Kitajou, S. Okada, *ChemElectroChem*. 2017, *4*, 2755.

[12] H. Li, H. Tang, C. Ma, Y. Bai, J. Alvarado, B. Radhakrishnan, S. P. Ong, F. Wua, Y. S. Meng, C. Wu, *Chem. Mater.* **2018**, *30*, 2498.

[13] W. Shen, H. Li, Z. Guo, Z. Li, Q. Xu, H. Liu, Y. Wang, *RSC Adv*. **2016**, *6*, 71581.

[14] F. Lalère, V. Seznec, M. Courty, R. David, J. N. Chotard, C. Masquelier, *J. Mater. Chem. A* **2015**, *3*, 16198.

[15] R. Liu, G. Xu, Q. Li, S. Zheng, G. Zheng, Z. Gong, Y. Li, E. Kruskop, R. Fu, Z. Chen, K. Amine, Y. Yang, *ACS Appl. Mater. Interfaces* 2017, *9*, 43632.

[16] Y. Zhao, X. Gao, H. Gao, H. Jin, J. B. Goodenough, *Adv. Funct. Mater*. **2020**, *30*, 1908680.

[17] W. Zhou, L. Xue, X. Lü, H. Gao, Y. Li, S. Xin, G. Fu, Z. Cui, Y. Zhu, J. B. Goodenough, *Nano Lett*. **2016**, *16*, 7836.

[18] F. Chen, V. M. Kovrugin, R. David, O. Mentré, F. Fauth, J. N. Chotard, C. Masquelier, *Small Methods*, **2019**, *3*, 1800218.

[19] M. V. Zakharkin, O. A. Drozhzhin, I. V. Tereshchenko, D. Chernyshov, A. M. Abakumov, E. V. Antipov, K. J. Stevenson, *ACS Appl. Energy Mater.* **2018**, *1*, 5842.

[20] R. Liu, S. Zheng, Y. Yuan, P. Yu, Z. Liang, W. Zhao, R. Shahbazian-Yassar, J. Ding, J. Lu, Y. Yang, *Adv. Energy Mater*. **2021**, *11*, 2003256.

[21] S. Ghosh, N. Barman, M. Mazumder, S. K. Pati, G. Rousse, P. Senguttuvan, *Adv. Energy Mater*. **2020**, *10*, 1902918.

[22] D. V. Anishchenko, M. V. Zakharkin, V. A. Nikitina, J. Keith; K. J. Stevenson, E. V. Antipov, *Electrochim. Acta*, **2020**, *354*, 136761.

[23] J-N. Chotard, G. Rousse, R. David, O. Mentré, M. Courty, C. Masquelier, *Chem. Mater*. **2015**, *27*, 5982.

[24] E. R. Losilla, M. A. G. Aranda, S. Bruque, M. A. Paris, J. Sanz, A. R. West, *Chem. Mater*. **1998**, *10*, 665.

[25] R. G. Shulman, *J. Chem. Phys*. **1958**, *29*, 945.

[26] D. Liu, X. Li, L. Wei, T. Zhang, A. Wang, C. Liu, R. Prins, *Dalton Trans*. **2017**, *46*, 6366.

[27] P. Conte, D. Šmejkalová, A. Piccolo, R. Spaccini, *Eur. J. Soil Sci.* **2008**, *59*, 584.

[28] B. C. Melot, D. O. Scanlon, M. Reynaud, G. Rousse, J-N. Chotard, M. Henry, J-M. Tarascon, *ACS Appl. Mater. Interfaces* **2014**, *6*, 10832.

[29] Z. Jian, W. Han, X. Lu, H. Yang, Y-S. Hu, J. Zhou, Z. Zhou, J. Li, W. Chen, D. Chen, L. Chen, *Adv. Energy Mater*. **2013**, *3*, 156.

[30] Z. Jian, C. Yuan, W. Han, X. Lu, L. Gu, X. Xi, Y.-S. Hu, H. Li, W. Chen, D. Chen, Y. Ikuhara, L. Chen, *Adv. Funct. Mater*. **2014**, *24*, 4265.

[31] M. V. Zakharkin, O. A. Drozhzhin, S. V. Ryazantsev, D. Chernyshov, M. A. Kirsanova, I. V. Mikheev, E. M. Pazhetnov, E. V. Antipov, K. J. Stevenson, *Journal of Power Sources*, 2020, *470*, 228231.

[32] F. Omenya, N. A. Chernova, R. Zhang, J. Fang, Y. Huang, F. Cohen, N. Dobrzynski, S. Senanayake, W. Xu, M. S. Whittingham, *Chem. Mater.* **2013**, *25*, 85.

[33] G. Chen, A. K. Shukla, X. Song, T. J. Richardson, *J. Mater. Chem.* **2011**, *21*, 10126.

[34] F. Omenya, B. Wen, J. Fang, R. Zhang, Q. Wang, N. A. Chernova, J. Schneider-Haefner, F. Cosandey, M. S. Whittingham, *Adv. Energy Mater*. **2015**, *5*, 1401204.

Chapter - 5

Multi-redox ($V^{5+}/V^{4+}/V^{3+}/V^{2+}$) Driven Asymmetric Sodium (De)intercalation Reactions in NASICON-$Na_3VIn(PO_4)_3$ Cathode

NASICON-$Na_3V_{2-x}M_x(PO_4)_3$ (M = Al^{3+}, Cr^{3+}, Fe^{3+} & Ga^{3+}) cathodes are attractive for sodium-ion battery application due to their high voltage multi-redox ($V^{5+}/V^{4+}/V^{3+}$) couples and faster sodium-ion diffusivity. However, they suffer from rapid capacity decay due to irreversible structural changes occurring at high voltages. Herein, we present the structural and electrochemical sodium (de)intercalation properties of NASICON-$Na_3VIn(PO_4)_3$ (NVIP) cathode. Although, this In^{3+}-substituted cathode also undergoes similar high voltage structural degradation, but its structure is rejuvenated through the following low voltage deep-sodiation process, resulting in reversible capacities of ~145 mA h g^{-1} (i.e., equivalent to ~2.82 moles of Na per vanadium). Our combined electrochemical, *in-operando* X-ray diffraction and *ex-situ* X-ray absorption spectroscopy analyses reveal asymmetric sodium (de)intercalation pathways of the NVIP cathode in the window of 4.2-1.2 V *vs.* Na^+/Na^0 that is driven by multi-redox ($V^{5+}/V^{4+}/V^{3+}/V^{2+}$) couples.

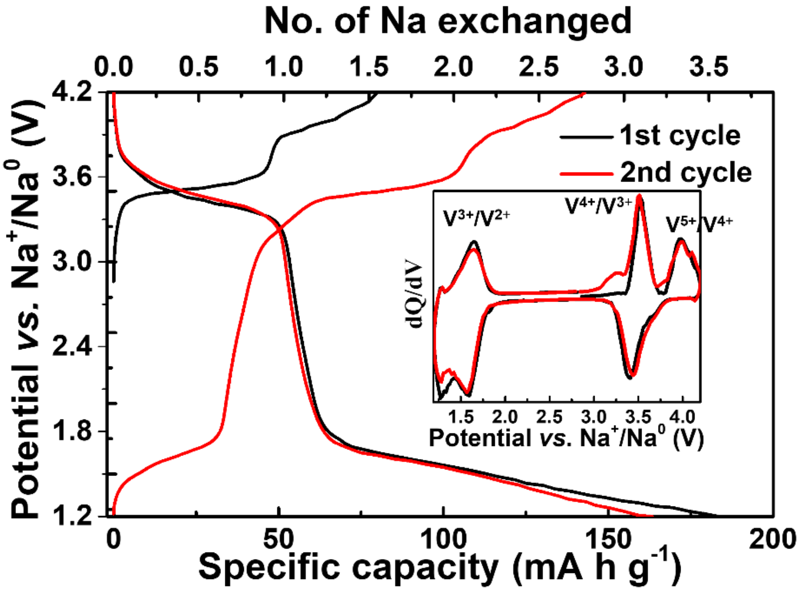

5.1. Introduction

Despite the dominance of lithium-ion batteries in portable electronics and electric vehicle markets, its expansion to grid storage application is impeded by high cost and depleting resources of lithium. From this viewpoint, sodium-ion batteries (SIBs) are appealing as the low-cost and sustainable solution for grid storage since its precursor is inexpensive and earth abundant.[1,2] Various classes of Na-ion cathode, anode and electrolyte materials have been explored during the last decade, thanks to the design knowledge garnered from analogous Li-ion chemistry. The present SIBs are built by pairing carbonaceous anode with either layered oxide or polyanionic cathodes. Whilst the layered oxide cathodes offer high intercalation capacities, they suffer from low insertion voltages, cycling degradation and air instability.[3] On the other hand, polyanionic cathodes are attractive due to high insertion voltages and enhanced structural stability.[4]

Among the polyanionic cathode materials, NASICON- $Na_3V_2(PO_4)_3$ (NVP) have received a great amount of interest due to its high intercalation voltage and sodium ion diffusivity.[5] It reversibly exchanges two moles of sodium ions per formula unit (*pfu*) (or one Na per vanadium) at 3.45 V *vs.* Na^+/Na^0 *via* oxidation of V^{3+} to V^{4+}, accounting for a theoretical capacity and an energy density of 117 mA h g^{-1} and 396 Wh kg^{-1}, respectively.[6,7] It also reversibly (de)intercalate another one mole of sodium ions *pfu* at 1.65 V *vs.* Na^+/Na^0 through the redox activity of V^{3+}/V^{2+} couple. It is worth noting that sodium (de)intercalation reactions

(i.e., $\mathrm{Na_3V_2(PO_4)_3 \leftrightarrow NaV_2(PO_4)_3 + 2Na^+ + 2}e^-$ & $\mathrm{Na_3V_2(PO_4)_3 + Na^+ +} e^- \leftrightarrow \mathrm{Na_4V_2(PO_4)_3}$)

proceed *via* two-phase mechanism.[8] Further, to improve the energy density of the NVP cathode, it is paramount to remove the remaining sodium ions from the $NaV_2(PO_4)_3$

endmember through the activation of high voltage V^{5+}/V^{4+} redox couple, which can lead to an exchange of 1.5 Na per vanadium and high theoretical capacity of 176 mA h g^{-1}. However, the high voltage charging of NVP cathode was unsuccessful to extract additional sodium ions beyond two moles *pfu*.[9] The following theoretical calculations have ascribed high voltage operation of V^{5+}/V^{4+} couple and high energy barrier to remove sodium ions from Na(1) site as the limiting factors to realize three mole of sodium ion exchange from the NVP cathode.[10]

Interestingly, the recent chemical tuning strategies to partially substitute vanadium in the NVP with other *ali*o- and *iso*-valent cations have paved way for multielectron sodium (de)intercalation reactions through the activation of high voltage V^{5+}/V^{4+} couple.[11-23] In particular, *iso*-valent cationic substituted cathodes ($Na_3V_{2-x}M_x(PO_4)_3$; M = Al^{3+}, Cr^{3+}, Fe^{3+} & Ga^{3+}) deliver almost similar charge capacities compared to the NVP, but the extraction of sodium ions involves concomitant oxidation of V^{3+} to V^{4+} and V^{5+}; in other words, more than one sodium ions per vanadium has been realized. Besides, the high voltage operation of V^{5+}/V^{4+} in the $Na_3V_{2-x}M_x(PO_4)_3$ cathodes renders high energy densities compared to the unsubstituted NVP. For instance, Al^{3+} substituted $Na_3V_{1.5}Al_{0.5}(PO_4)_3$ cathode shows 1.5 and 0.5 moles of sodium (de)intercalation at 3.37 (V^{4+}/V^{3+}) and 3.95 V (V^{5+}/V^{4+}) *vs*. Na^+/Na^0, respectively, thus delivering slightly higher energy density (424 Wh kg^{-1}) compared to the NVP.[24] However, such high voltage charging process triggers irreversible structural transformation to another Na-poor NASICON phase upon removal of sodium ions from Na(1) sites in addition to Na(2) sites, which results in rapid capacity decay.[25] To alleviate this issue, strategies involving cationic substitution, low temperature and low voltage window cycling have been reported.[26,27]

In this work, we have investigated the structural and electrochemical sodium (de)intercalation properties of $Na_3VIn(PO_4)_3$ (NVIP) cathode. Similar to the other IIIA group-cationic substituted NVP cathodes (Al^{3+} and Ga^{3+})[23,24], the substitution of electrochemically inactive In^{3+} in the NASCION framework is expected to trigger high voltage V^{5+}/V^{4+} redox couple, thereby increasing the overall energy density of the cathode. Moreover, the substitution of heavy In^{3+} is expected to hinder (local) structural changes and stabilize the framework during electrochemical cycling. Unfortunately, the abovementioned high voltage structural irreversibility still persists in the NVIP cathode. Moving forward, we explore multi-redox $V^{5+}/V^{4+}/V^{3+}/V^{2+}$ driven highly reversible asymmetric sodium (de)intercalation process in the NVIP cathode using combined electrochemical, *in-operando* XRD and *ex-situ* XAS studies.

5.2. Experimental

The synthesis of the NVIP cathode was carried out through sol-gel method. V_2O_5 (99.6%, Sigma), citric acid (99.5%, Sigma), NaH_2PO_4 (99%, Sigma) and In-acetate (99.99%, Sigma) were used as-received. To synthesize the cathode material, V_2O_5 (0.5 mmol) and citric acid (1.1 mmol) were dissolved in 50 mL distilled water for overnight to reduce vanadium followed by addition of NaH_2PO_4 (3 mmol) and In-acetate (1 mmol). The precursors were mixed by stirring and dried at 100 °C. The recovered powder was ground and annealed in N_2 atmosphere at 350 and 700 °C for 10 and 12 h, respectively, with an intermittent grinding. Similar procedure was followed to prepare $Na_3V_2(PO_4)_3$ (NVP) using stoichiometric amount of V_2O_5, citric acid and NaH_2PO_4.

For the details on the material and electrochemical characterizations, see Chapter 2.

5.3. Results and Discussion

The XRD pattern of the as-prepared $Na_3VIn(PO_4)_3$ (NVIP) cathode is displayed in Figure 5.1a. It can be fully indexed with $R\bar{3}c$ space group with lattice parameters of a = 8.8462(14) and c = 22.080(3) Å (refer Table 5.1). The increase in lattice parameters compared to the NVP cathode[28] is due to the partial substitution of larger ionic radius In^{3+} (0.8 Å) in the place of V^{3+}(0.64 Å).[29] Further, the DSC data (Figure 5.1b) collected on the NVIP from -50 to 200 ˚C does not show any signature of phase transitions as observed for the NVP and aluminum substituted NVP cathodes.[24,30] It could be due to the suppression of (local) structural distortion and Na^+-ion/vacancy ordering upon heavy In^{3+} substitution in the NASICON framework. Scanning electron microscopy image displays the presence of nanosized particles that are embedded in carbon matrix (Figure 5.1c). Energy dispersive X-ray spectroscopy analysis (Figure 5.1c) has quantified the atomic ratio of Na:V:In as 2.99:0.98:1.02 and confirmed their homogenous distribution in the sample. The amount of carbon present in the NVIP cathode is estimated as ~3.16 wt. % by CHN analysis.

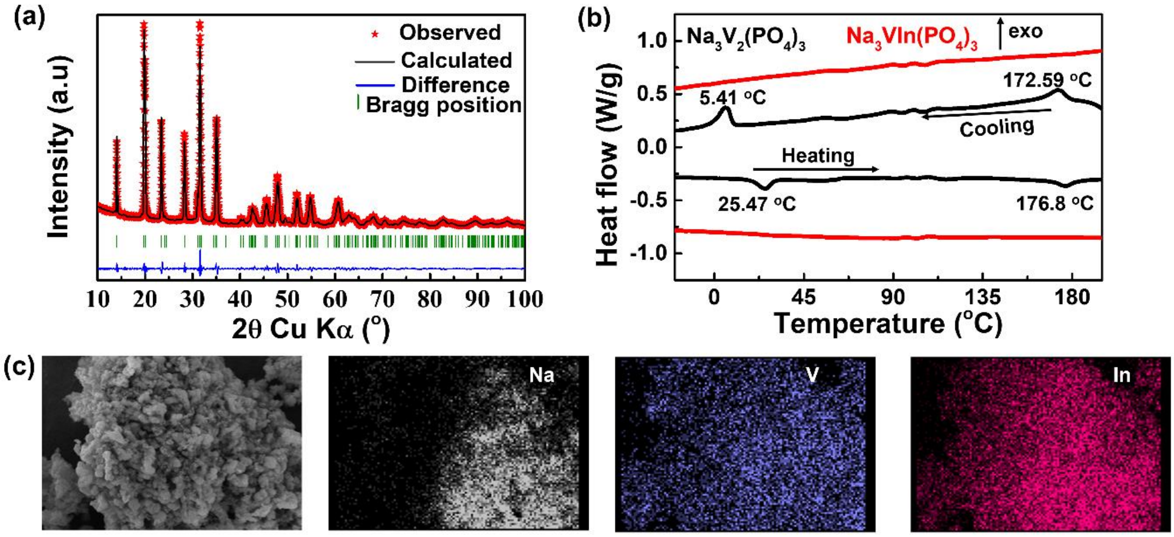

Figure 5.1. (a) Rietveld refined X-ray diffraction (XRD) pattern, (inset) Scanning electron microscopy (SEM) image and (b) Differential scanning calorimetry (DSC) plot of the sol-gel synthesized NVIP cathode in comparison with DSC plot of NVP. (c) FESEM and EDS mapping images of NVIP.

Table 5.1. Crystallographic parameters of the NVIP cathode

Compositions	**$Na_3VIn(PO_4)_3$**
Space group	$R\bar{3}c$

Lattice parameters (Å)	$a = b = 8.8462(14)$, $c = 22.080(3)$	
Reliability factors	$\mathrm{Chi}^2 = 4.96$ & $R_{wp} = 12.3\%$	
Bond Lengths (Å)	**(V/In)–O**	2.061 (6) × 3 2.155 (4) × 3
	P–O	1.509 (4) × 2, 1.529(6) × 2
	Na (1)– O	2.499 (4) × 6
	Na(2) – O	2.367 (6) × 2, 2.908 (8) × 2, 2.545 (8) × 2, 2.563 (5) × 2

Initially, we have carried out galvanostatic cycling tests of NVIP cathode at C/10 rate in different voltage regions (3.8-2.75, 4.2-2.75 and 2.75-1.2 V *vs*. Na^+/Na^0) to understand its electrochemical sodium (de)intercalation properties that are centered around selected vanadium redox couples (i.e., V^{4+}/V^{3+}, $V^{5+}/V^{4+}/V^{3+}$ and V^{3+}/V^{2+}, respectively) (Figure 5.2). Note that the theoretical capacity of the $Na_3V^{3+}In^{3+}(PO_4)_3$ cathode is estimated as 50 mA h g^{-1} for one mole of sodium ion (de)intercalation *pfu*. When it is cycled in the window of 3.8-2.75 V *vs*. Na^+/Na^0, it delivers a reversible capacity of 43 mA h g^{-1}, which is equivalent to an exchange of 0.8 moles of sodium ions *pfu* (Figure 5.2a). Interestingly, it displays slightly sloped voltage-capacity profiles in contrast to the NVP cathode with an average voltage of 3.45 V, corresponding to the redox activity of V^{4+}/V^{3+} couple. These changes are also reflected in its dQ/dV plots (Figure 5.2b), which show broader voltage features unlike the sharper ones noticed in the case of NVP cathode, implying possible changes in its sodium (de)intercalation mechanism. To better understand about it, we have conducted an *in-operando* XRD experiment (Figure 5.3a) at C/10 rate. The lattice parameters calculated for the selected *in-operando* XRD patterns (that are collected on different state-of-charge as denoted by "numbers" in the corresponding voltage-time plots) are displayed in Table 5.2. The NVIP cathode exhibits narrower solid-solution regions at the beginning and end of charge/discharge processes (Δx≈0.2-0.3) that are separated by a two-phase transformation region. At the end of charge ("2"), the XRD pattern belonging to a single NASICON-"$Na_{2.2}V^{3.8+}In^{3+}(PO_4)_3$" phase (estimated based on the electrochemical extraction) is observed. Moreover, the original structure of the NVIP cathode is restored at the end of discharge ("3").

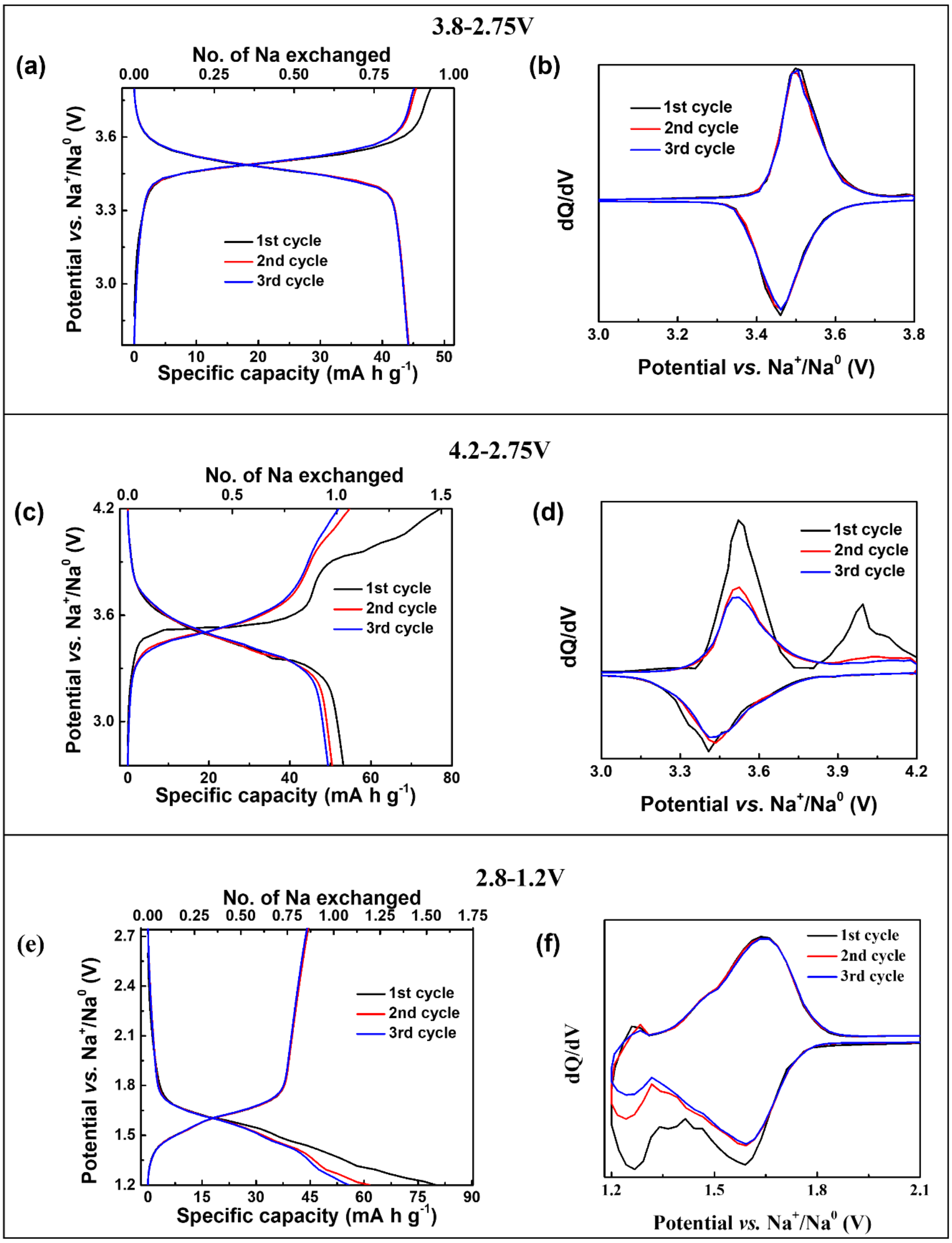

Figure 5.2. (a,c,e) Voltage-capacity and (b,d,f) differential capacity (dQ/dV) profiles of the NVIP cathode collected in different voltage windows at C/10 rate.

Upon extending the upper cutoff voltage to 4.2 V *vs*. Na^+/Na^0, the NVIP cathode shows an additional sloping voltage curve above 3.8 V during the first charge due to the redox activity of V^{5+}/V^{4+} couple (Figure 5.2c). The total charge capacity of the NVIP cathode is estimated as 77 mA h g^{-1}, which is equivalent to a removal of 1.5 moles of sodium ions *pfu*. However, on subsequent discharge, the voltage-capacity profile has changed into a S-shaped curve with a discharge capacity of 53 mA h g^{-1}, corresponding to the formation of mixed-valent "$Na_{2.5}V^{3.5+}In^{3+}(PO_4)_3$" phase at the end of discharge (2.75 V *vs*. Na^+/Na^0). The first cycle irreversible capacity (24 mA h g^{-1}, which is equivalent to 0.47 moles of sodium ions *pfu*) could be tentatively ascribed to the loss of sodium ions from Na(1) sites during the high voltage charging.[25] From the second cycle onwards, the voltage-capacity profiles are highly reversible with capacities of ~50 mA h g^{-1}. The changes in the voltage-capacity plots can be better viewed from their corresponding dQ/dV voltage profiles (Figure 5.2d). Whilst the two oxidation peaks noticed at 3.5 and 4.0 V *vs*. Na^+/Na^0 could be ascribed to the redox activity of V^{4+}/V^{3+} and V^{5+}/V^{4+} couples, respectively, the reduction peak centered around ~3.4 V *vs*. Na^+/Na^0 involves mixed "$V^{5+}/V^{4+}/V^{3+}$" activity. To comprehend the structural changes of the NVIP cathode during its cycling in the window of 4.2-2.75 V *vs*. Na^+/Na^0, the *in-operando* XRD measurement was performed (Figure 5.3b). As the voltage raises to 3.8 V, the sodium deintercalation of the NVIP cathode proceeds similarly as in the case of previous experiment. Beyond this point, the sodium deintercalation proceeds *via* solid-solution reaction until the formation of sodium-poor "$Na_{1.5}V^{4.5+}In^{3+}(PO_4)_3$" phase at the end of charge (4.2 V, "6"), which shows anisotropic cell parameter changes (i.e., increase and decrease of *c*- and *a*- axis, respectively; refer Table 5.2), in accordance with earlier reports.[18,19,20,25] On the following discharge, the XRD peaks continuously shift towards lower 2θ values, suggesting the solid-solution reaction mechanism. More importantly, the diffraction peaks collected on the discharged cathode

"$Na_{2.5}V^{3.5+}In^{3+}(PO_4)_3$" at 2.75 V ("7") does not match with pristine electrode, thus confirming about the irreversible phase transformation happened at high voltage. Further, the *in-operando* patterns collected during the second cycle of NVIP cathode show reversible sodium (de)intercalation phenomena proceeding *via* complete solid-solution process in contrast to its first cycle (Figure 5.4).

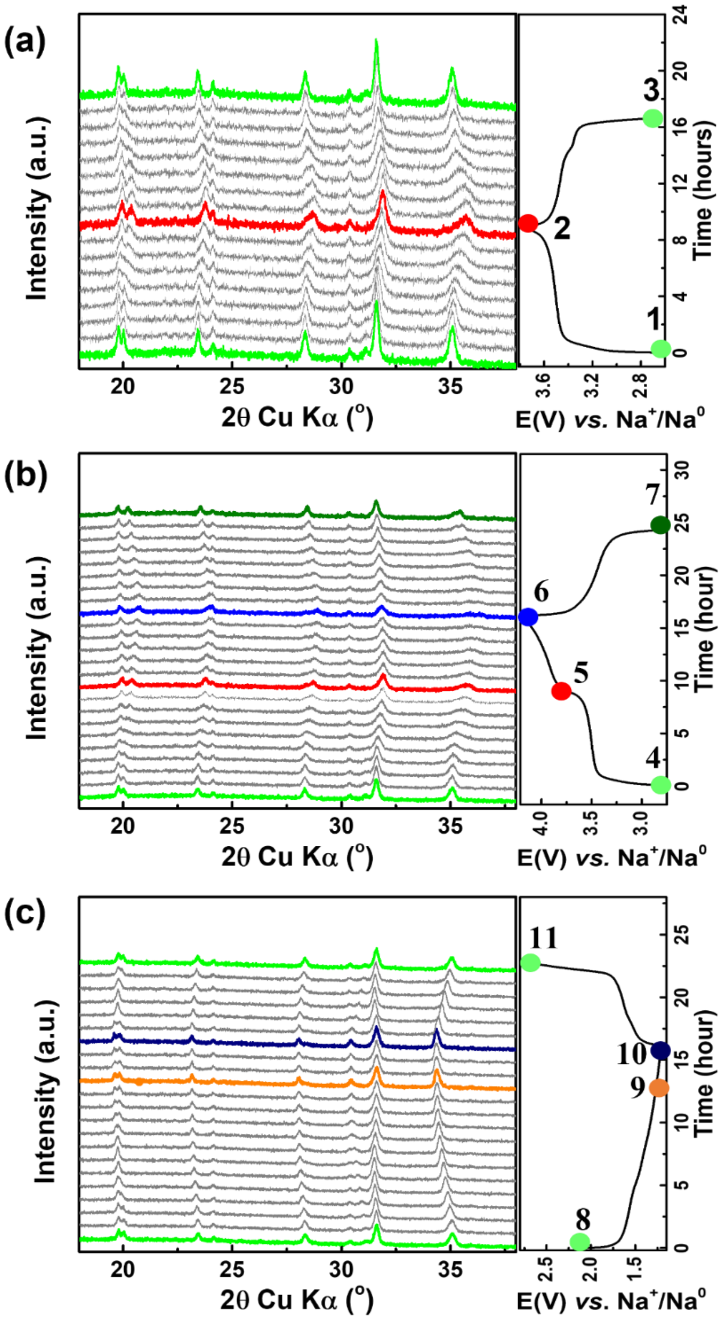

Figure 5.3. *In-operando* XRD patterns of the NVIP cathode collected in the voltage windows of (a) 3.8-2.75, (b) 4.2-2.75 and (c) 2.75-1.2 V *vs*. Na^+/Na^0.

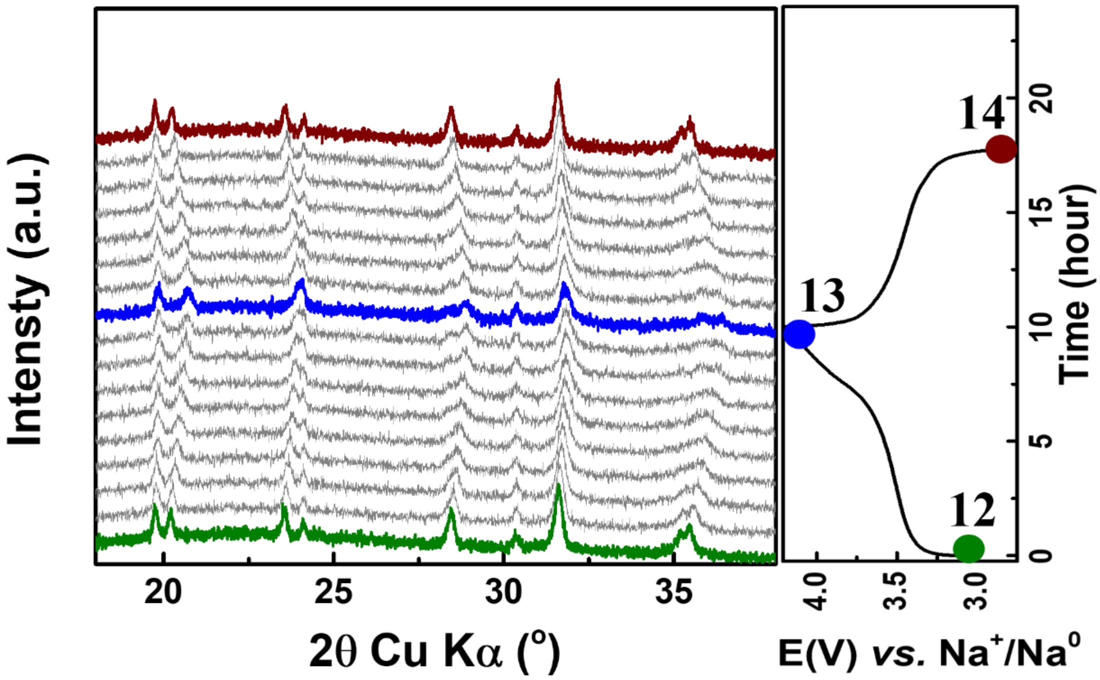

Figure 5.4. *In-operando* XRD patterns of the NVIP cathode collected during 2nd cycle in the voltage window of 4.2-2.75 V *vs.* Na^+/Na^0.

Table 5.2. Lattice parameters calculated for selected *in-operando* XRD patterns of the NVIP cathode.

Pattern No.	***a* (Å)**	***c* (Å)**	**V ($Å^3$)**
3.8-2.75 V			
1	8.817	22.012(2)	1481.979(8)
2	8.671(3)	21.948	1429.233(8)
3	8.814(5)	22.007(2)	1480.802(5)
4.2-2.75 V (1st cycle)			
4	8.812(5)	22.001(5)	1479.728(5)
5	8.652	21.955(6)	1423.344(9)
6	8.584(2)	22.264(3)	1420.855(1)
7	8.748(6)	22.144	1467.79(6)
2.75-1.2 V			

8	8.810(8)	22.004(7)	1479.393(5)
9	9.009(9)	21.710(8)	1526.340(5)
10	9.007(8)	21.682(3)	1523.623(6)
11	8.816(5)	21.992(4)	1480.480(7)
4.2V-2.75 V (2nd cycle)			
12	8.736(8)	22.123(8)	1462.501(6)
13	8.589(3)	22.277(7)	1423.372(1)
14	8.728(4)	22.160(5)	1462.123(6)
3.8-1.2 V			
15	8.817	22.012(2)	1481.979(4)
16	8.671(3)	21.948	1429.233(8)
17	8.814(5)	22.007(1)	1480.802(5)
18	8.900(3)	21.709(4)	1524.152(4)
19	9.009(8)	21.715(1)	1526.584(4)
20	8.812(2)	22.001	1479.586(4)
4.2-1.2 V			
21	8.812(5)	22.001(5)	1479.728(5)
22	8.652	21.955(6)	1423.344(9)
23	8.584(2)	22.264(3)	1420.855(1)
24	8.748(6)	22.144	1467.79(6)
25	8.826(1)	22.097(2)	1490.772(6)
26	8.988(5)	21.757(2)	1522.349(6)
27	9.984(8)	21.744(8)	1520.216(6)

28	8.813(3)	22.012(1)	1480.713(6)
29	8.638(2)	21.976(8)	1420.189(1)
30	8.589(2)	22.242(1)	1421.086(1)
31	8.749(7)	22.158(3)	1469.123(6)

Turning our attention towards the low voltage window cycling (2.75-1.2 V *vs*. Na^+/Na^0) of the NVIP cathode (Figure 5.2e), it is expected to uptake one mole of sodium ions *pfu* to form $Na_4V^{2+}In^{3+}(PO_4)_3$ endmember through the activity of V^{3+}/V^{2+} couple. However, its voltage-capacity profile shows higher first discharge capacity (~80 mA h g^{-1}, which is equivalent to an insertion of 1.5 moles of sodium ions *pfu*), but nearly half of it is reversible on the subsequent charge. The corresponding dQ/dV plots (Figure 5.2f) show reversible voltage feature at ~1.6 V, which is due to the redox activity of V^{3+}/V^{2+} couple. The low voltage reduction peak located at 1.28 V can be ascribed to the electrolyte decomposition/solid electrolyte interface (SEI) formation. This observation is also further confirmed by our *in-operando* XRD measurement (Figure 5.3c), as the patterns collected between "9" and "10" do not show any significant changes. Indeed, this electrolyte decomposition/SEI formation processes are continuous on the subsequent cycling, which results poor Coulombic efficiencies (58-82 % during the first five cycles) (Figure 5.5). It is also worth mentioning here that we could not accurately determine the number of sodium ions inserted as well as trapped in the NVIP structure due to the electrolyte degradation/SEI formation. Further, the *in-operando* XRD measurement reveals that NVIP cathode undergoes two-phase transformation mechanism between its "$Na_3V^{3+}In^{3+}(PO_4)_3$" and "$Na_{3.75}V^{2.25+}In^{3+}(PO_4)_3$" endmembers. Overall, structurally speaking, we observe fully reversible sodium (de)intercalation reactions involving V^{4+}/V^{3+} and V^{3+}/V^{2+}

couples, whilst the high voltage V^{5+}/V^{4+} redox triggers structural irreversibility and changes in sodium (de)intercalation pathways of the NVIP cathode.

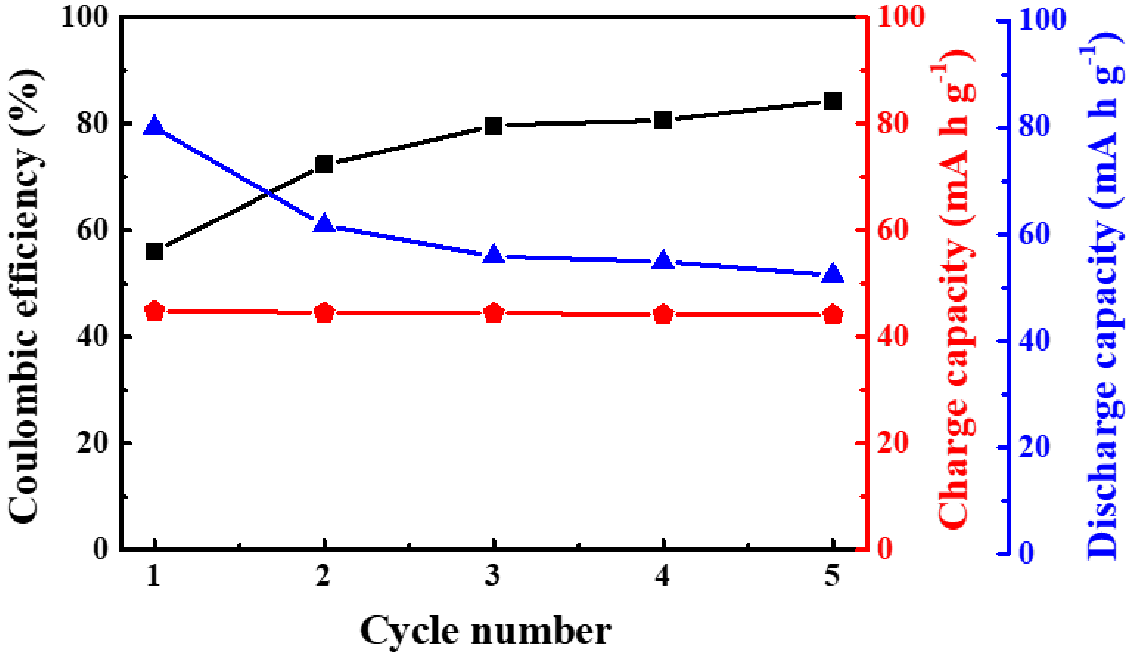

Figure 5.5. Coulombic efficiencies for the NVIP cathode cycled at C/10 rate in the window of 2.75-1.2 V *vs*. Na^+/Na^0.

Further, we have expanded our galvanostatic studies to two different voltage regions of 3.8-1.2 and 4.2-1.2 V *vs*. Na^+/Na^0 in order to understand the sodium (de)intercalation properties of the NVIP cathode associated with multi-redox $V^{4+}/V^{3+}/V^{2+}$ and $V^{5+}/V^{4+}/V^{3+}/V^{2+}$ couples, respectively (Figure 5.6). As expected, the NVIP cathode exhibits reversible two-step voltage-capacity profiles at average voltages of 3.45 and 1.5 V in the window of 3.8-1.2 V *vs*. Na^+/Na^0 (Figure 5.6a), corresponding to the redox activity of V^{4+}/V^{3+} and V^{3+}/V^{2+} couples, respectively. The reversible nature of these redox features is also clearly visible from the dQ/dV plots (Figure 5.6b). Its first charge and discharge capacities are estimated as ~49 and 130 mA h g^{-1}, which is nearly matching with the total capacities obtained from the individual cycling windows (3.8-2.75 and 2.75-1.2 V *vs*. Na^+/Na^0). On the following charge, almost two moles of sodium ion are removed (which is equivalent ~100 mA h g^{-1}), proving that the extra capacity observed during the first discharge is due to the electrolyte decomposition and SEI formation as explained above. Moreover, our *in-operando* XRD experiment (Figure 5.7) in this voltage window shows a combination of structural evolution events that are observed during cycling in the 3.8-2.75 and 2.75-1.2 V *vs.* Na^+/Na^0 voltage windows. Specifically, the XRD patterns of pristine and cycled electrodes ("15" and "20") neatly superimpose on each other which confirms high reversibility of the sodium (de)intercalation processes involving $V^{4+}/V^{3+}/V^{2+}$ multi-redox couples.

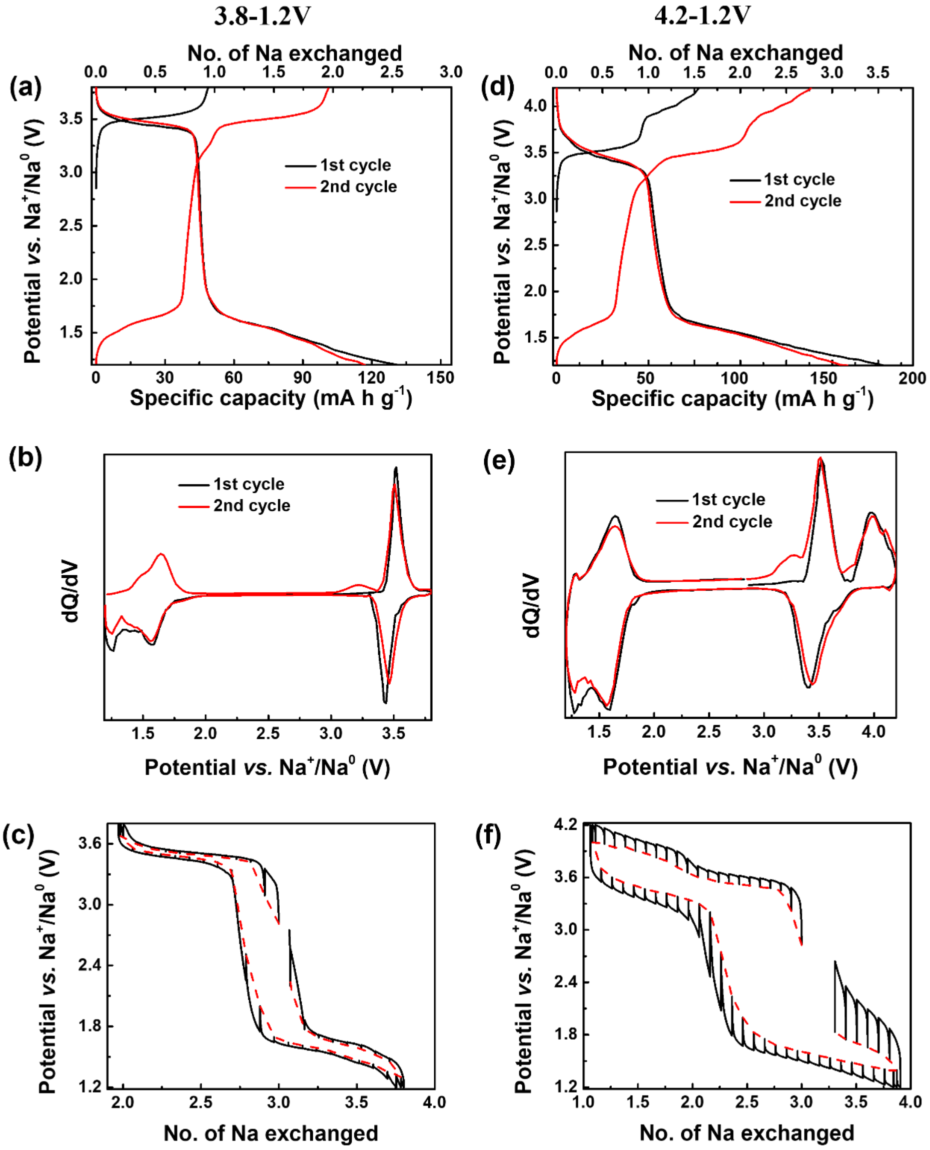

Figure 5.6. (a,d) Voltage-capacity, (b,e) differential capacity (dQ/dV) and (c,f) galvanostatic intermittent titration technique (GITT) profiles of the NVIP cathode collected in different voltage windows.

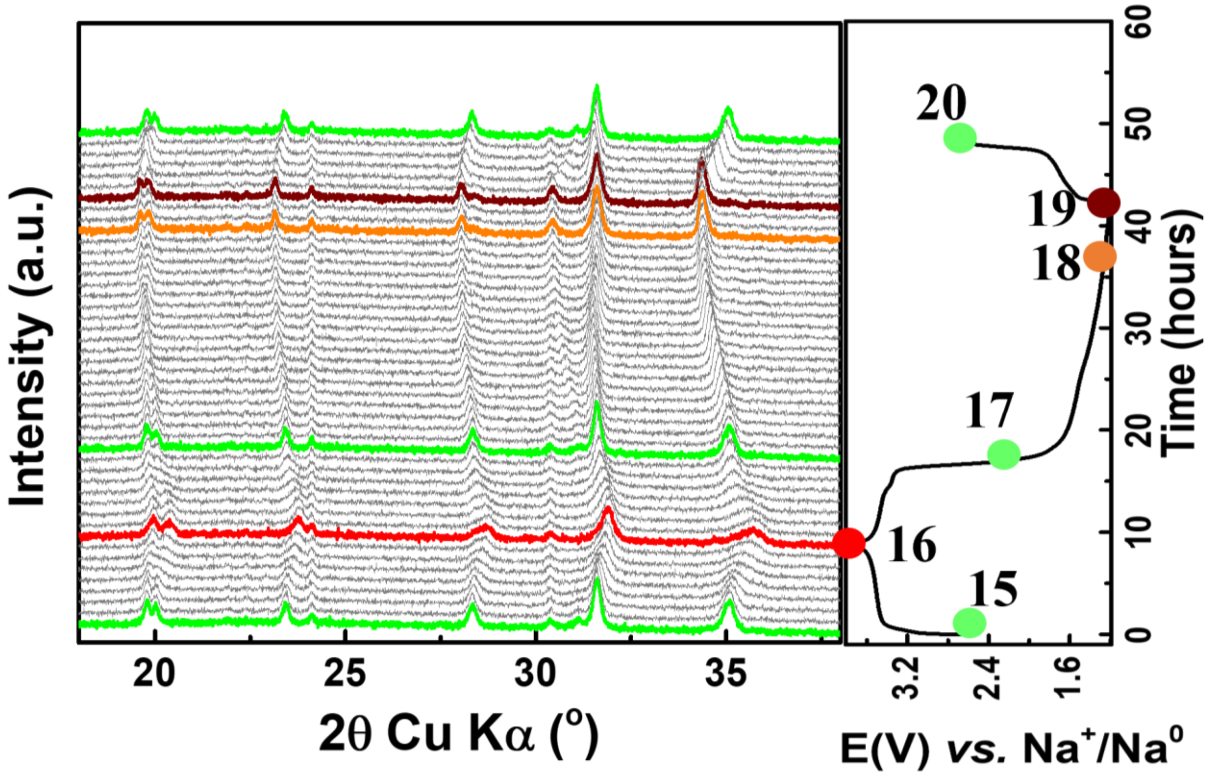

Figure 5.7. *In-operando* XRD patterns of the NVIP cathode collected at C/10 in the voltage of 3.8-1.2-2.75 V.

On the other hand, the voltage-capacity profiles of the NVIP cathode collected in the window of 4.2-1.2 V *vs*. Na^+/Na^0 (Figure 5.6d) are strikingly different compared to those obtained from the previous high voltage experiment (4.2-2.75 V *vs*. Na^+/Na^0). It reversibly delivers capacities of ~145 mA h g^{-1} from the second cycle onwards (i.e., equivalent to an exchange of ~2.82 moles of sodium ions per vanadium), involving multi-redox $V^{5+}/V^{4+}/V^{3+}/V^{2+}$ couples. On the subsequent cycles, its charge/discharge voltage profiles neatly overlap on each other, confirming high reversibility of sodium (de)intercalation reactions. However, the signatures of voltage-capacity profiles collected between charge and discharge processes differ, i.e., the discharge profiles entail a S-shaped voltage curve from 4.2 to 2.8 V followed by a voltage plateau at ~1.5 V whilst the charge profiles exhibit a two-step voltage profile (at ~1.55 and 3.45 V) followed by a sloping curve above 3.8 V *vs*. Na^+/Na^0. These changes can be better viewed from the corresponding dQ/dV plots (Figure 5.6e). Three oxidation peaks are located at 1.6, 3.5 and 4.0 V whilst only two reduction peaks are noticed at 3.45 and 1.55 V. More importantly, the length of each voltage step (or the number of sodium ions (de)inserted) in the charge/discharge voltage-capacity profiles differs, implying about various extent of vanadium redox reactions associated with them. To better understand about the abovementioned changes, galvanostatic intermittent titration technique (GITT) experiments during the fourth cycle of the NVIP cathode in the windows of 3.8-1.2 and 4.2-1.2 V *vs*. Na^+/Na^0 (Figure 5.6c and f). The equilibrium voltage trace obtained from the latter experiment show remarkable hysteresis (particularly beyond $\Delta x = 1.0$) in comparison with the former, proving asymmetric vanadium redox reactions and changes in sodium (de)intercalation pathways in the NVIP cathode. Recently, similar observations have been made on the disordered $Na_3V_2(PO_4)_2F_3$ cathode, wherein the changes in its electrochemical signature are ascribed to the electrochemically triggered structural disorder.[31]

Therefore, to understand the changes in the crystal structure of the NVIP cathode, we have conducted an *in-operando* XRD measurement in this voltage region (Figure 5.8a). It shows similar structural evolution between “21” to “24” compared to previous high voltage experiment (Figure 5.3b), i.e., a two-phase transformation followed by a solid-solution formation during the first charge and a complete solid-solution process on the subsequent discharge. The electrode collected at this point (“24”) have a composition of “$Na_{2.5}V^{3.5+}In^{3+}(PO_4)_3$” with mixed V^{4+}/V^{3+} oxidation states. Upon continuous discharge to 1.2 V, we observe a narrow solid-solution region until the electrode reaches a composition of “$Na_{3.0}V^{3+}In^{3+}(PO_4)_3$” (“25”) followed by a two-phase transformation mechanism. The calculated lattice parameter for the “$Na_{3.0}V^{3+}In^{3+}(PO_4)_3$” phase (“25” in Table 5.2) is found be very closer to those of pristine electrode (“21”), thus confirming the rejuvenation of the NVIP crystal structure. Note that the XRD patterns collected between “26” to “27” do not show any noticeable changes which is due to electrolyte degradation/SEI formation process. On the following charge to 2.75 V, a two-phase sodium deintercalation reaction is observed as in the case of 2.75-1.2 V *vs*. Na^+/Na^0 experiment. Further, the *in-operando* XRD patterns collected during 2.75-4.2-2.75 V *vs*. Na^+/Na^0 region (Figure 5.9) shows similar structural evolution as in the case of previous high voltage experiment (Figure 5.3b).

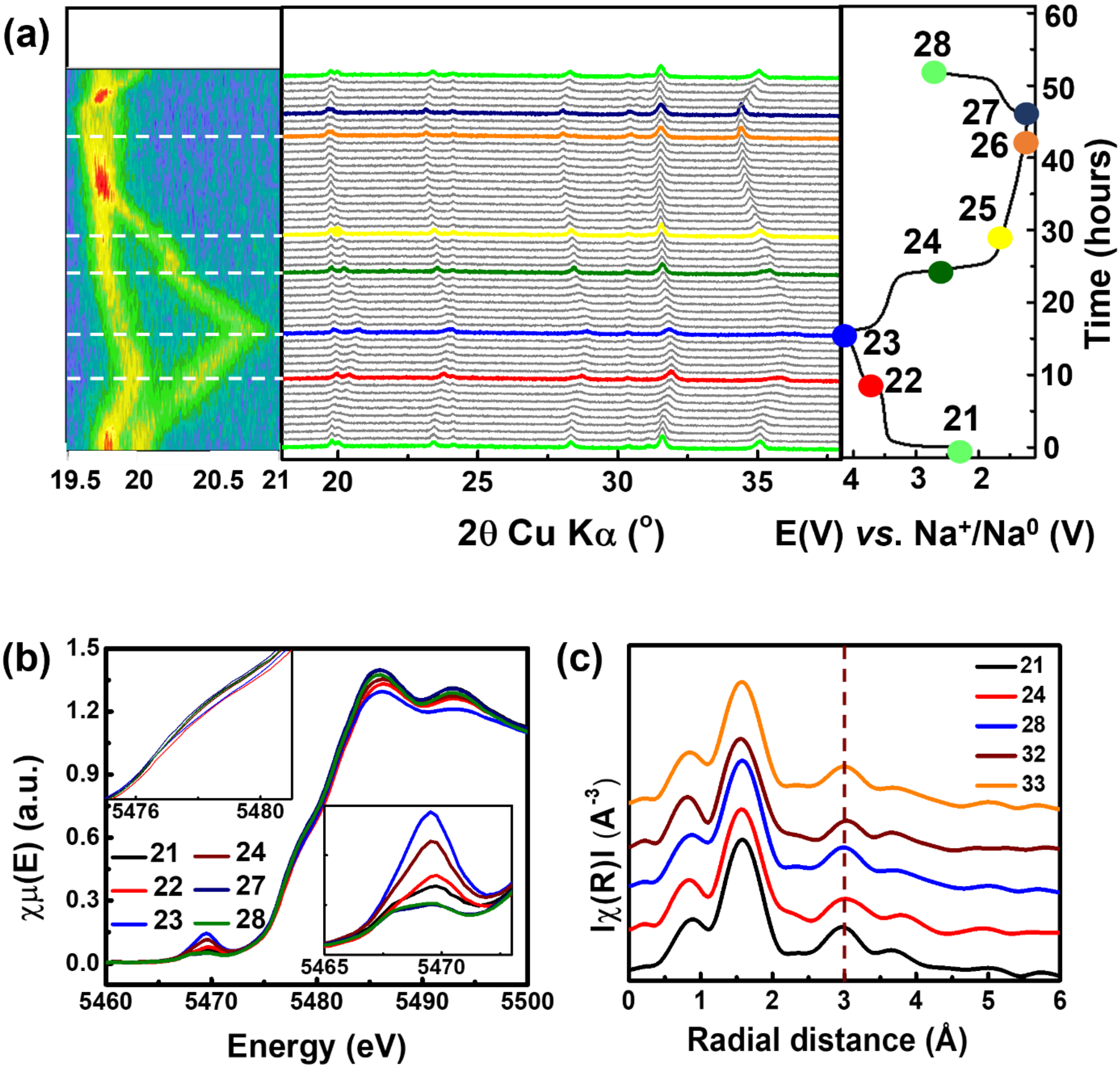

Figure 5.8. (a) *In-operando* XRD patterns of the NVIP cathode collected in the voltage of 4.2-2.75 V *vs*. Na^+/Na^0. (b) X-ray absorption near edge structure (XANES) and (c) Fourier-transformed extended X-ray absorption fine structure (FT-EXAFS) spectra at the V K-edge of the NVIP cathode with different state of charge.

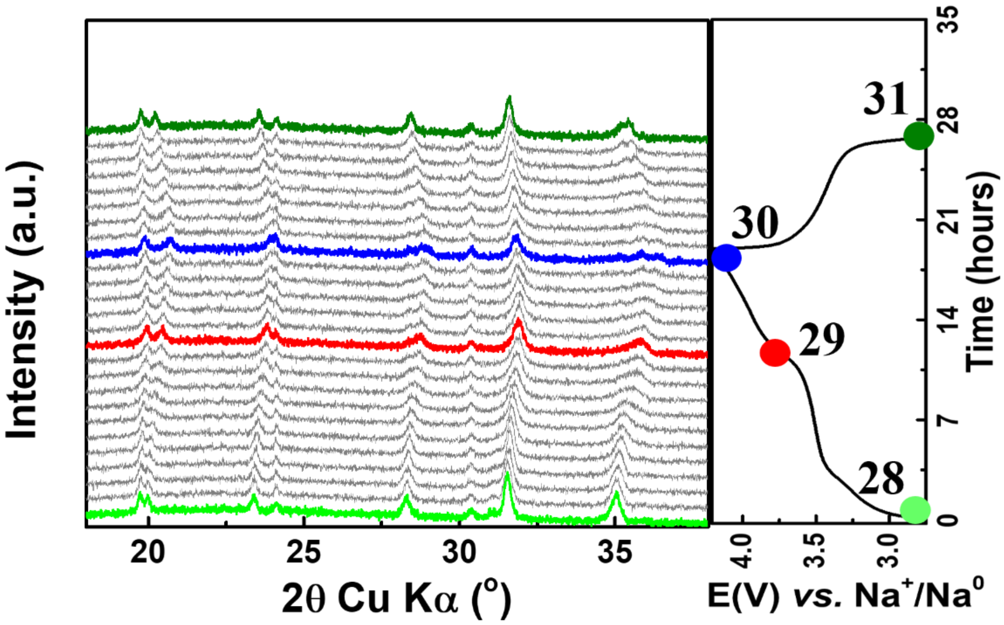

Figure 5.9. *In-operando* XRD patterns of the NVIP cathode collected in the voltage of 4.2-2.75 V *vs*. Na^+/Na^0 (in continuation to Figure 5.8a).

To investigate the redox and local structural changes of the NVIP cathode, *ex-situ* X-ray absorption spectroscopy measurements were performed. The normalized XANES spectra of the NVIP cathode with different state of charge is displayed in Figure 5.8b. As the cathode is charged to 4.2 V *vs*. Na^+/Na^0, its absorption edge shifts towards higher energy, indicating the oxidation of V^{3+} to V^{4+} and V^{5+}. More prominent changes are observed at the pre-edge of the XANES spectra; its intensity increases as the charge process proceeds (from “21” to “23”), which is characteristic of V^{4+} and V^{5+}.[25,26] However, the XANES spectra collected at 2.75 V *vs*. Na^+/Na^0 (“24”) during the subsequent discharge does not match with the pristine electrode. Once this cathode is discharged 1.2 V and charged back to 2.75 V *vs*. Na^+/Na^0 (“28”), its XANES spectra is almost recovered to its original structure, validating our electrochemical and *in-operando* XRD results. The recovery of the NVIP structure is further confirmed from the magnitude plots of the Fourier-transformed extended X-ray absorption fine structure (FT-EXAFS) at the V K-edge (Figure 5.8c). Whilst the peak located at ~1.5 Å represent (V/In)-O scattering pairs, the peaks observed in the range of 2.8-3.2 Å is due to scattering of (V/In)-Na and (V/In)-P outer shells. The spectra collect at “24” show noticeable changes in the outer shells compared to the pristine electrode due to loss of sodium ions from the structure. Upon rejuvenation (“28”), the spectrum is almost recovered back its original state.

Overall, our combined electrochemical, *in-operando* XRD and *ex-situ* XANES experiments reveal multi-redox $V^{5+}/V^{4+}/V^{3+}/V^{2+}$ driven asymmetric sodium (de)intercalation reactions in the NVIP cathode when it is cycled in the broader voltage window. As mentioned earlier, this asymmetric redox process is trigged by the irreversible structural transformation of the cathode at high voltage upon removal of sodium ion from Na(1) sites, which is then rejuvenated through a low voltage deep-sodiation process. More importantly, we found that this rejuvenation process does not depends on cycling history of cathode, i.e., the NVIP cathodes, which are initially cycled ten or fifteen times in the window 4.2-2.75 V, show similar voltage-capacity profiles compared to its pristine state upon opening their cycling window to 4.2-1.2 V (Figure 5.10). Moreover, the *in-operando* XRD patterns collected on the cycled NVIP cathode (collected after ten cycles at C/10 rate in the window of 4.2-2.75 V) (Figure 5.11) exhibit similar structural evolution as like in Figure 5.8a, whilst its corresponding EXAFS spectra exhibit complete recovery of cathode structure (Figure 5.8c).

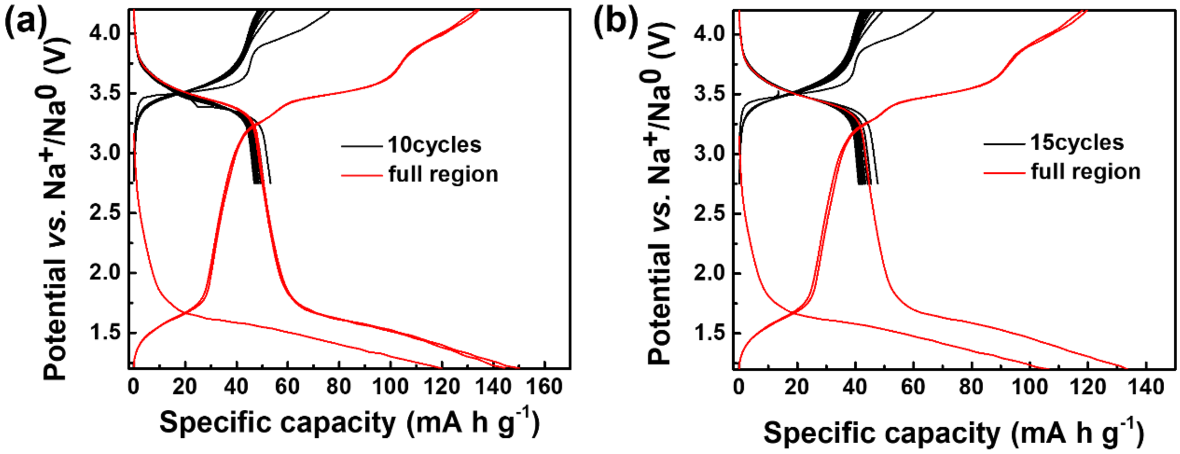

Figure 5.10. Voltage-capacity profiles of the NVIP cathode cycled at C/10 rate. (a) First cycled in the window of 4.2-2.75 V *vs*. Na^+/Na^0 for ten times followed by cycling in the window of 4.2-1.2 V *vs*. Na^+/Na^0. (b) First cycled in the window of 4.2-2.75 V *vs*. Na^+/Na^0 for 15 times followed by cycling in the window of 4.2-1.2 V *vs*. Na^+/Na^0.

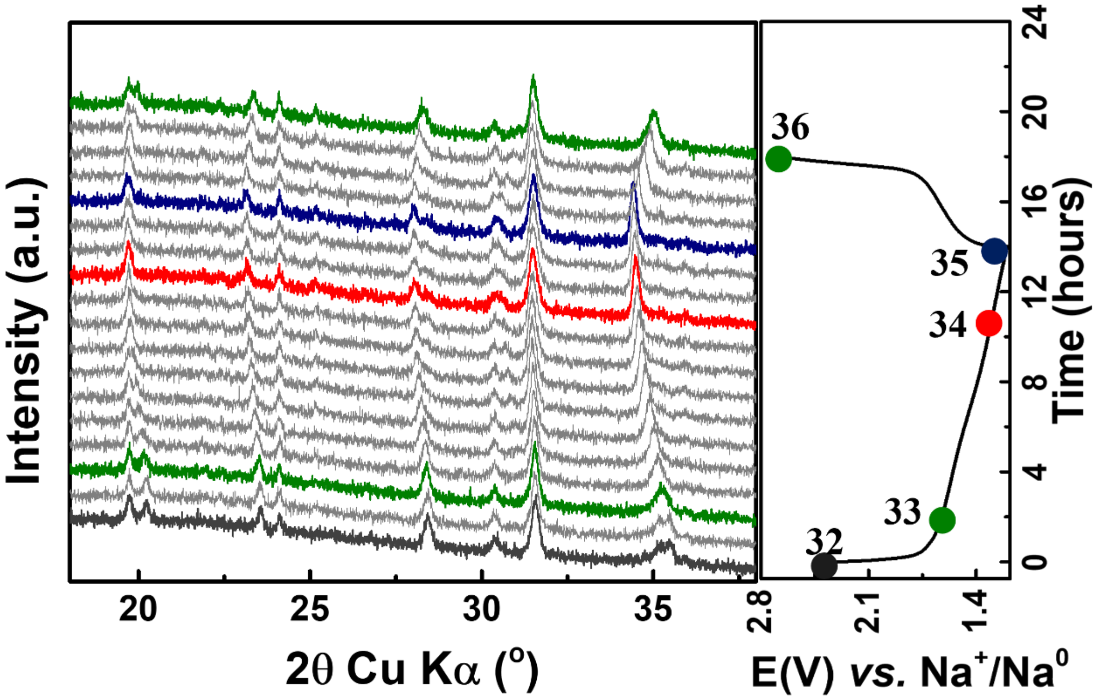

Figure 5.11. *In-operando* XRD patterns of the cycled NVIP cathode (collected after 10 cycles at C/10 in the window of 4.2-2.75 V).

5.4. Conclusions

In summary, we have attempted to substitute *iso*-valent In^{3+} in the NASICON framework to trigger the high voltage V^{5+}/V^{4+} redox in the NVIP cathode, thereby enhancing its capacity. However, such high voltage redox process results in capacity loss due to its structural degradation as in the case of other cationic substituted NVP cathodes, which highlights the major limitation of cationic substitution strategy. Upon extending its cycling voltage window to 4.2-1.2 V, the degraded NVIP cathode structure was rejuvenated *via* deep-sodiation process at lower voltages, resulting in highly reversible asymmetric sodium (de)intercalation reactions that are driven by multi-redox ($V^{5+}/V^{4+}/V^{3+}/V^{2+}$) couples.

References

[1] Z. Yang, J. Zhang, M. C. W. Kintner-Meyer, X. Lu, D. Choi, J. P. Lemmon, J. Liu, *Chem. Rev*. **2011**, *111*, 3577.

[2] J-Y. Hwang, S-T. Myung, Y-K. Sun, *Chem. Soc. Rev*. **2017**, *46*, 3529.

[3] P-F. Wang, Y. You, Y-X. Yin, Y-G. Guo, *Adv. Energy Mater*. **2018**, *8*, 1701912.

[4] C. Masquelier, L. Croguennec, *Chem. Rev*. **2013**, *113*, 6552.

[5] S. Chen, C. Wu, L. Shen, C. Zhu, Y. Huang, K. Xi, J. Maier, Y. Yu, *Adv. Mater*. **2017**, *29*, 1700431.

[6] Y. Uebou, T. Kiyabu, S. Okada, J.-I. Yamaki, *Rep. Inst. Adv.Mater. Study*, **2002**, *16.*

[7] S. Y. Lim, H. Kim, R. A. Shakoor, Y. Jung, J. W. Choi, *J. Electrochem. Soc.* **2012**, *159*, A1393.

[8] Z. Jian, W. Han, X. Lu, H. Yang, Y-S. Hu, J. Zhou, Z. Zhou, J. Li, W. Chen, D. Chen, L. Chen, *Adv. Energy Mater*. **2013**, *3*, 156.

[9] W. Song, X. Ji, Z. Wu, Y. Zhu, Y. Yang, J. Chen, M. Jing, F. Li, C. E. Banks, *J. Mater. Chem. A*, **2014**, *2*, 5358.

[10] Y. Ishado, A. Inoishi, S. Okada, *Electrochemistry*, **2020**, *88*, 457.

[11] M. J. Aragón, P. Lavela, G. F. Ortiz, J. L Tirado, *ChemElectroChem*. **2015**, *2*, 995.

[12] A. Inoishi, Y. Yoshioka, L. Zhao, A. Kitajou, S. Okada, *ChemElectroChem*. **2017**, *4*, 2755.

[13] W. Shen, H. Li, Z. Guo, Z. Li, Q. Xu, H. Liu, Y. Wang, *RSC Adv*. **2016**, *6*, 71581.

[14] Y. Zhao, X. Gao, H. Gao, H. Jin, J. B. Goodenough, *Adv. Funct. Mater*. **2020**, *30*, 1908680.

[15] W. Zhou, L. Xue, X. Lü, H. Gao, Y. Li, S. Xin, G. Fu, Z. Cui, Y. Zhu, J. B. Goodenough, *Nano Lett*. **2016**, *16*, 7836.

[16] F. Chen, V. M. Kovrugin, R. David, O. Mentré, F. Fauth, J. N. Chotard, C. Masquelier, *Small Methods*, **2019**, *3*, 1800218.

[17] M. V Zakharkin, O. A. Drozhzhin, I. V. Tereshchenko, D. Chernyshov, A. M. Abakumov, E. V.Antipov, K. J. Stevenson, *ACS Appl. Energy Mater.* **2018**, *1,* 5842.

[18] S. Ghosh, N. Barman, M. Mazumder, S. K. Pati, G. Rousse, P. Senguttuvan, *Adv. Energy Mater*. **2020**, *10*, 1902918.

[19] D. V. Anishchenko, M. V. Zakharkin, V. A. Nikitina, J. Keith, K. J. Stevenson, E. V. Antipov, *Electrochim. Acta*, **2020**, *354*, 136761.

[20] M. J. Aragón, P. Lavela, G. F. Ortiz, J. L. Tirado, *J. Electrochem. Soc*. **2015**, 162, A3077.

[21] D. Zhang, P. Feng, B. Xu, Z. Li, J. Qiao, J. Zhou, C. Chang, *J. Electrochem. Soc.* **2017**, *164*, A3563.

[22] H. Ma, B. Zhao, J. Bai, K. Li, Z. Fang, P. Wang, W. Li, X. Zhu, Y. Sun, *J. Electrochem. Soc.* **2020**, *167*, 070548.

[23] Q. Hu, J-Y. Liao, X-D. He, S. Wang, L-N. Xiao, X. Ding, C-H. Chen, *J. Mater. Chem. A*, **2019**, *7*, 4660.

[24] F. Lalère, V. Seznec, M. Courty, R. David, J. N. Chotard, C. Masquelier, *J. Mater. Chem. A*, **2015**, *3*, 16198.

[25] R. Liu, G. Xu, Q. Li, S. Zheng, G. Zheng, Z. Gong, Y. Li, E. Kruskop, R. Fu, Z. Chen, K. Amine, Y. Yang, *ACS Appl. Mater. Interfaces*, **2017**, *9*, 43632.

[26] S. Ghosh, N. Barman, P. Senguttuvan, *Small*, **2020**, *16*, 2003973.

[27] R. Liu, S. Zheng, Y. Yuan, P. Yu, Z. Liang, W. Zhao, R. Shahbazian-Yassar, J. Ding, J. Lu, Y. Yang, *Adv. Energy Mater*. **2021**, *11*, 2003256.

[28] I. V. Zatovsky, *Acta Crystallogr. Sect. E*, **2010**, *66*, i12.

[29] R. D. Shannon, *Acta Crystallogr. A*, **1976**, *32*, 751.

[30] J-N. Chotard, G. Rousse, R. David, O. Mentré, M. Courty, C. Masquelier, *Chem. Mater*. **2015**, *27*, 5982.

[31] G. Yan, S. Mariyappan, G. Rousse, Q. Jacquet, M. Deschamps, R. David, B. Mirvaux, J. W. Freeland, J -M. Tarascon, *Nat. Commun.* **2019**, *10*, 585.

Chapter - 6

Impact of Mg^{2+} and Al^{3+} Substitutions on the Structural and Electrochemical Properties of NASICON-$Na_xVMn_{0.75}M_{0.25}(PO_4)_3$ (M=Mg and Al) Cathodes for Sodium-ion Batteries

Sodium superionic conductor (NASICON)-$Na_4VMn(PO_4)_3$ (NVMP) cathode is attractive for sodium-ion battery (NIB) application due to its reduced cost, toxicity and high energy density (~425 Wh kg^{-1}). However, it exhibits significant polarization, limited rate and cycling performances due to its lower electronic conductivity and formation of Jahn-Teller active Mn^{3+} during cycling. In this report, a chemical approach is presented to partially replace Mn^{2+} of the NVMP framework by Mg^{2+} and Al^{3+} substitutions. The Mg- and Al-substituted NVMP cathodes present smoother voltage profiles, facile sodium (de)intercalation, enhanced rate performances (80 mA h g^{-1} at 5C rate) and capacity retention (~96% after 100 cycles) in comparison with the unsubstituted sample. Their enhanced performances are attributed to suppressed Jahn-Teller effect, increased covalent character and sodium ion vacancies of the NASICON framework. These results highlight the significance of fine tuning the chemical compositions to attain high performance NASICON cathodes.

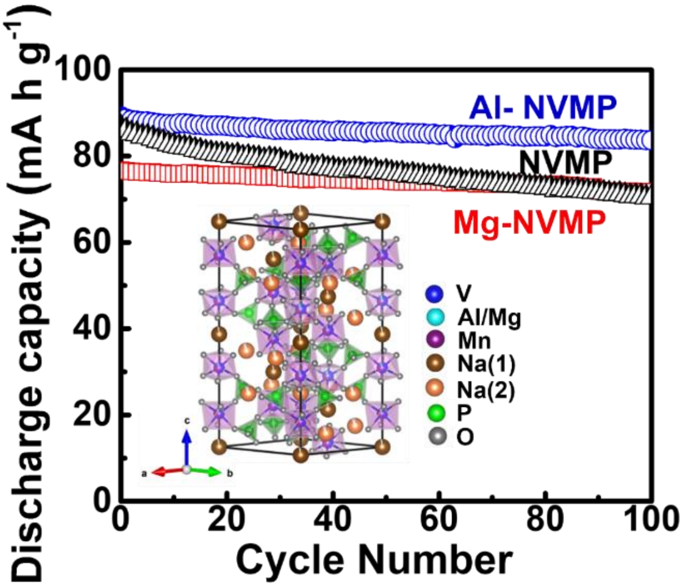

6.1. Introduction

Sodium-ion batteries (NIBs) have been recognized as one of the most promising candidates for the grid storage application due to inexpensive and earth abundant sodium precursors.[1,2] To date, different class of cathode materials such as layered oxides, polyanionic compounds and Prussian blue analogues have been explored. Whilst the layered oxides offer higher intercalation capacities, they suffer from low intercalation voltages, air instability and poor cycle life that impedes their application in NIBs.[3,4] On the other hand, polyanionic cathodes offer rich crystal chemistry, high intercalation voltages and high structural stability.[5]

Among the polyanionic cathodes, sodium superionic conductor (NASICON)-$Na_3V_2(PO_4)_3$ (NVP) has received significant attention due to its high intercalation voltage, sodium ion conductivity, structural and thermal stabilities.[6,7] It crystal structure is made of so-called “lantern units” which consist of two VO_6 octahedra and three PO_4 tetrahedra. These lantern units are stacked along *c*-axis to make three dimensional framework, wherein sodium ions occupy two independent crystal sites (Na(1) and Na(2)).[8] It delivers reversible capacities closer to 110 mA h g^{-1} at an average intercalation voltage of 3.4 V *vs*. Na^+/Na^0, resulting an energy density of ~400 Wh kg^{-1}. The corresponding electrochemical sodium (de)intercalation reaction proceeds through a two-phase transformation (i.e., $Na_3V_2(PO_4)_3$ to $NaV_2(PO_4)_3$ *via* oxidation of V^{3+} to V^{4+}). It is also worth mentioning that $NaV_2(PO_4)_3$ phase contains the remaining sodium ions in the Na(1) sites, whilst the Na(2) sites are completely empty.[9] Various strategies were reported to fabricate carbon coated nano-NVP cathodes which exhibited enhanced rate performances with better cycling stability.[10-14]

Thanks to richness of NASCION crystal chemistry, the composition of the NVP cathode could be tuned by partially replacing vanadium ions with different *alio*- and *iso*-valent cations.[15-22] In particular, $Na_4VMn(PO_4)_3$ (NVMP) composition is very attractive because of its reduced cost and toxicity as well as its improved energy density (425 Wh kg^{-1}) with respect to the NVP cathode.[22] Its sodium (de)intercalation reaction proceeds though two voltage steps (V^{4+}/V^{3+} at 3.4 V & Mn^{3+}/Mn^{2+} at 3.6 V *vs*. Na^+/Na^0) with reversible capacities of ~110 mA h g^{-1}. Further, when the charging window is extended to 4.3 V *vs*. Na^+/Na^0, higher first charge capacity has been obtained (~150 mA h g^{-1}, which is equivalent to removal of three moles of sodium per formula unit), thanks to the activity of $V^{5+}/V^{4+}/V^{3+}$ and Mn^{3+}/Mn^{2+} redox couples.[23-26]

Nevertheless, the NVMP cathode still suffers from two major issues which limits its potential application in NIBs. First, the NVMP cathode prepared by solid state reaction exhibited limited reversible capacity, significant polarization and poor capacity retention. Such inferior performance could be attributed to its limited electronic conductivity and formation Jahn-Teller active Mn^{3+} during cycling. To address this issue, recently a carbon coated (~8.6 wt %) nano-NVMP cathode was developed, which had shown enhanced rate performances and cycle life.[27] However, such approach is time consuming, laborious and the resulting cathode has lower energy density for practical application (because of its higher carbon content and lower packing density). Second, although its high voltage charging process delivers increased capacity, the subsequent discharge is not fully reversible.[24,25] It is attributed to irreversible structural transformation associated with the removal of sodium ions from Na(1) sites. Further, the NVMP cathode undergoes rapid capacity degradation upon cycling at high voltage window (4.2-2.75 V *vs*. Na^+/Na^0).

To tackle the aforementioned problems, herein we present a chemical approach to partially substitute Mn^{2+} of the NVMP cathode by electrochemically inactive cations (Mg^{2+} and Al^{3+}). Our approach is aimed to reduce the concentration of manganese cations in the

NVMP cathode thereby suppressing the Jahn-Teller distortion and to increase covalency of the framework by inducing shorter (V/Mn/Mg/Al)-O bond lengths, which can enhance its structural stability and cycle life. Moreover, the substitution of aliovalent Al^{3+} cation in the NVMP framework creates sodium ion vacancies, which is expected to reduce the activation energy and enhance the sodium ion mobility.[26,28] As a result, the Mg- and Al-substituted NVMP cathodes have shown higher rate performances and cycling stabilities in comparison with unsubstituted sample.

6.2. Experimental

V_2O_5 (99.6%, Sigma), citric acid (99.5%, Sigma,), NaH_2PO_4 (99%, Sigma), Na_2CO_3 (99.5%, Sigma), Mn-acetate (99%, Sigma), Mg-acetate (98%, Finar), and $Al(NO_3)_3$ (Alfa, 98%) were used as-received in the synthesis of NASICON cathodes. To prepare the NVMP cathode, V_2O_5 (0.5 mmol) was reduced in 50 mL distilled water using citric acid (1.1 mmol) for overnight followed by addition of NaH_2PO_4 (3 mmol), Na_2CO_3 (0.5 mmol), and Mn-acetate (1 mmol). For the Mg-substituted NMVP synthesis, the stoichiometries of all the precursors were kept similar to that of NVMP synthesis, except Mn-acetate (0.75 mmol) and Mg-acetate (0.25 mmol) were added in the reaction mixture. Similarly, Na_2CO_3 (0.375 mmol), Mn-acetate (0.75 mmol) were added along with $Al(NO_3)_3$ (0.25 mmol) in the V_2O_5/citric acid/water reaction mixture to prepare Al-substituted NVMP sample. The precursors in water solution were thoroughly mixed, evaporated, and dried at 100 °C for overnight. The recovered powders were annealed at 350 and 700 °C in N_2 atmosphere for 10 and 12 h, respectively, with an intermittent grinding.

For the details on the material and electrochemical characterizations, see Chapter 2

6.3. Results and Discussion

The NASCION-$Na_4VMn(PO_4)_3$, $Na_4VMn_{0.75}Mg_{0.25}(PO_4)_3$ and $Na_{3.75}VMn_{0.75}Al_{0.25}(PO_4)_3$ samples (hereafter denoted as NVMP, Mg-NVMP and Al-NVMP, respectively) were synthesized by sol-gel route. Scanning electron microscopy (SEM) analyses of these samples reveal the presence of agglomerated nanoscale particles (Figure 6.1a). The homogenous distribution of Na/V/Mn/(Mg/Al) elements in all the samples are confirmed through energy dispersive spectroscopic analyses (Figure 6.1a). Flame atomic absorption spectroscopy analyses reveal the compositions of NVMP, Mg-NVMP and Al-NVMP samples as $Na_4V_{1.03}Mn_{0.95}(PO_4)_3$, $Na_{4.01}V_{1.03}Mn_{0.71}Mg_{0.28}(PO_4)_3$, $Na_{3.75}V_{1.01}Mn_{0.68}Al_{0.24}(PO_4)_3$, respectively. Thermogravimetric analyses (TGA) show the presence of 4.85, 4.89 and 1.12 wt % of carbon in the NVMP, Mg-NVMP and Al-NVMP samples, respectively (Figure 6.1b). The TGA curves show weight gain signatures beyond 450 °C, which is due to oxidation of V^{3+} and Mn^{2+} in air.[10] Further, CHN elemental analyses also confirm the carbon content in the NVMP, Mg-NVMP and Al-NVMP samples as 4.8, 5.01 and 1.04 wt%, respectively.

The effect of chemical substitution of Mg^{2+} and Al^{3+} in the NVMP framework was studied by X-ray diffraction technique. The XRD patterns of the as-synthesized NASICON samples can be fully indexed with $R\bar{3}c$ space group, thus confirming the complete solubility of Mg^{2+} and Al^{3+} in the NVMP lattice (Figure 6.2a). The corresponding refinement results obtained from Rietveld analysis of the XRD patterns are presented in Table 6.1. The calculated lattice parameters of the NVMP sample are in agreement with the literature.[22,24] Upon the substitution of Mg^{2+} in the NVMP framework, the lattice parameters as well as unit cell volume are decreased. This could be due to the smaller ionic radii of Mg^{2+} (0.72 Å) in comparison with Mn^{2+} (0.83 Å).[29] The occupancies of Na(1) and Na(2) sites in the NVMP and Mg-NVMP samples are found to be nearly full. On the other hand, the substitution of Al^{3+} in the NVMP lattice has resulted in anisotropic lattice parameter changes (i.e. decrease and increase of *a*- and *c*-parameters, respectively). The refinement have indicated the occupancies of Na(1) and Na(2) sites in the Al-NVMP sample as 0.9557(2) and 0.9160(5), respectively, which are closer to the targeted composition. The anisotropic changes in the lattice parameters could be ascribed to the smaller ionic radius of Al^{3+} (0.54 Å) as well as to the decreased sodium ion population in Na(1) sites, which in turn enhances the electrostatic repulsion between $(V/Mn/Al)O_6$ octahedra along *c*-direction.[26] Further, the average (V/Mn/Mg)-O and (V/Mn/Al)-O bond lengths in the Mg- and Al-NVMP cathodes are also shortened as expected (Table 6.1).

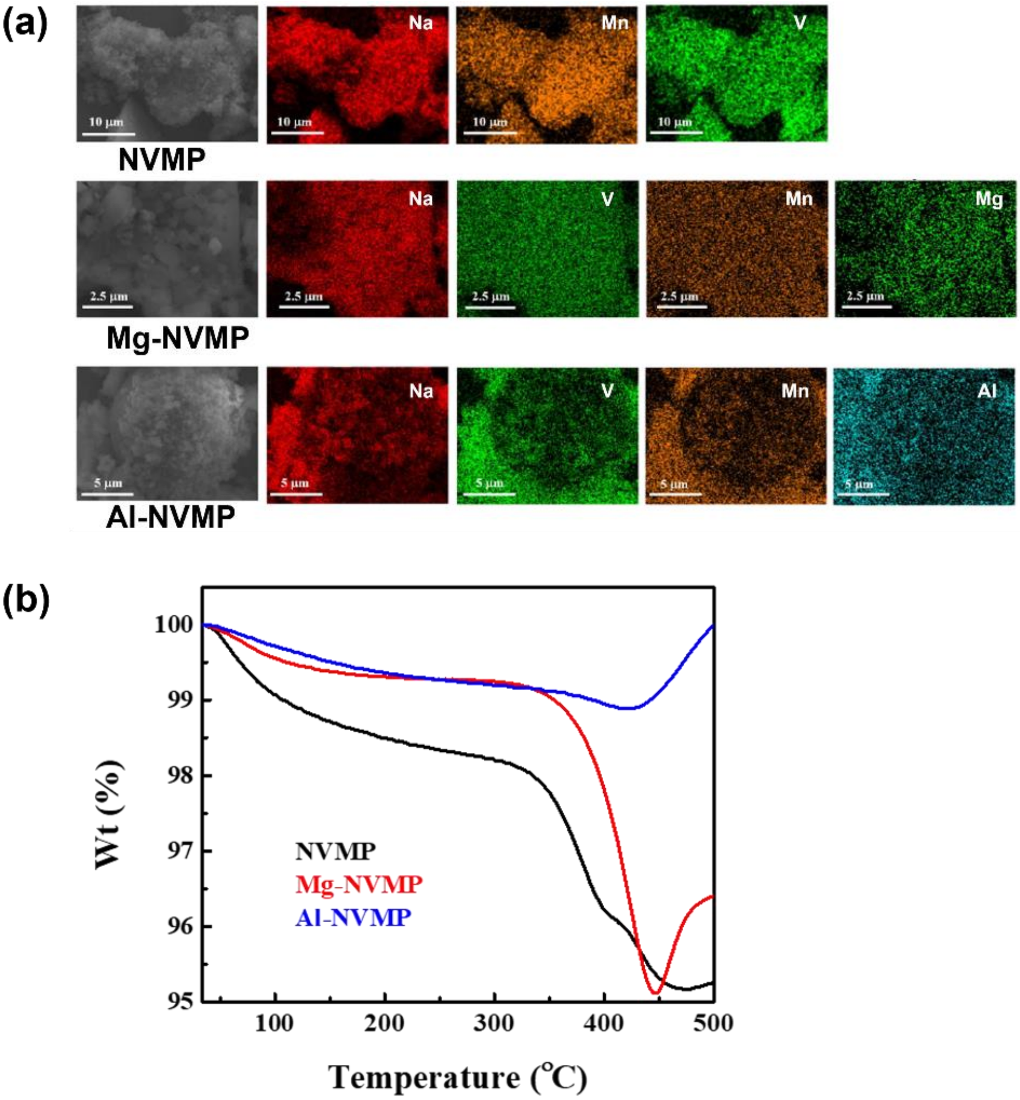

Figure 6.1. (a) SEM and EDS images of the NVMP, Mg-NVMP and Al-NVMP samples and (b) TGA plots.

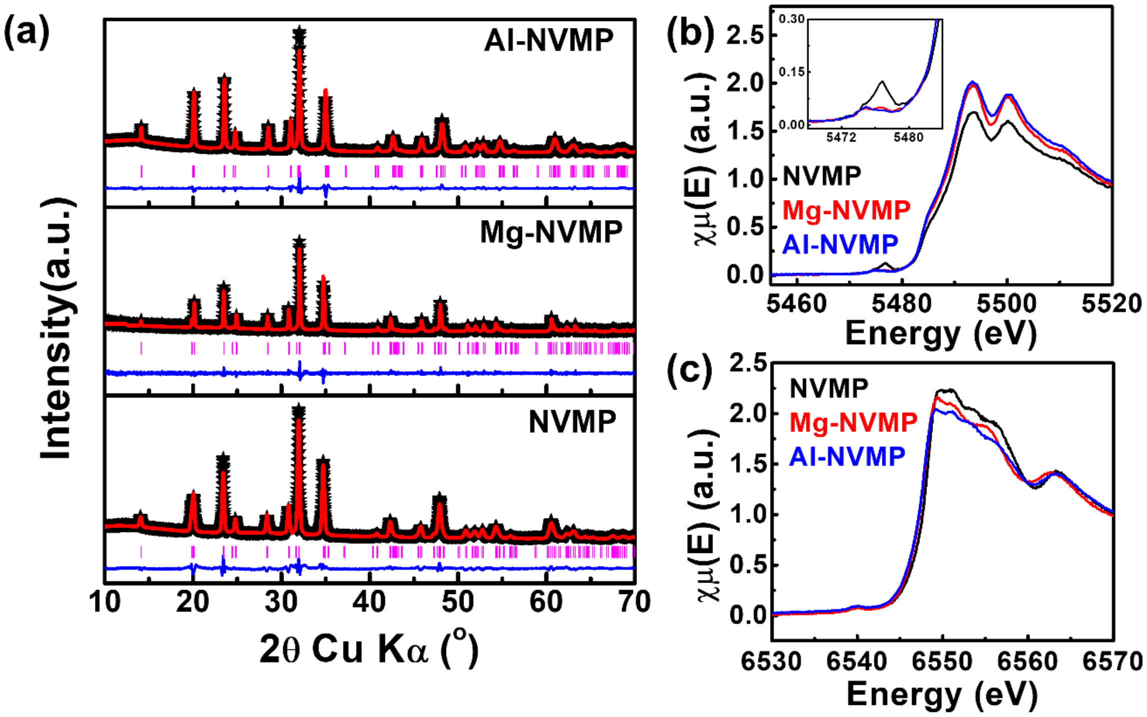

Figure 6.2. (a) Rietveld refinements of the XRD patterns and the normalized X-ray near edge spectra (XANES) at (b) V and (c) Mn-K edges of the NVMP, Mg-NVMP and Al-NVMP samples. A zoomed view of the vanadium pre-edges is shown in the inset of figure 1b.

Table 6.1. Crystallographic data obtained from Rietveld refinements of the XRD patterns of the NVMP, Mg-NVMP and Al-NVMP samples.

	NVMP	**Mg-NVMP**	**Al-NVMP**
Lattice Parameters (Å)	*a* = 8.9453(13) *c* =21.4965(5)	*a* = 8.9395(3) *c* =21.4520(9)	*a* = 8.8807(3) *c* =21.5648(10)
Volume (Å^3)	1492.44(4)	1484.65(9)	1472.89(10)
Chi^2	2.32	3.02	2.86
R$_{wp}$(%)	2.98	3.19	3.25
Na(1)	1	1	0.9557(2)
Na(2)	0.9847(2)	1	0.9160(5)
(V/Mn/M)-O (Å) (M= Mg or Al)	2.0903(11)×6	2.0778(5)×6	2.0594(13)×6
Na(1)-O (Å)	2.4574(7)×6	2.4529(3)×6	2.4534(5)×6

Na(2)-O (Å)	2.5794(11)×2 2.5398(9)×2 2.4714(13)×2 2.9154(8)×2	2.5831(7)×2 2.5616(4)×2 2.4583(9)×2 2.8822(6)×2	2.5838(12)×2 2.5146(8)×2 2.4469(16)×2 2.8952(9)×2

X-ray absorption spectroscopy (XAS) experiments were carried out on the NASICON samples to probe the oxidation states and local structural changes. The X-ray near edge spectra (XANES) of the NASICON cathodes at V and Mn K-edges are shown in figure 6.2b and c, respectively. The pre-edge feature at V K-edge (inset for Figure 6.2b) is due to electronic transitions from 1*s* to hybridized 3*d*-4*p* states and can be used to probe the changes in local symmetry.[30,31] The intensities of vanadium pre-edge peaks have decreased upon Mg- and Al-substitution, which indicate no contributions from vacant 3d states of Mg and Al as well as less distortion of VO_6 octahedra in the substituted cathodes. The absorption edge energies are found to be very closer for all the samples, thus confirming the oxidation states of V and Mn as +3 and +2 respectively.

Initially, we have assessed the electrochemical properties of the NVMP, Mg-NVMP and Al-NVMP cathodes in Na cells at C/10 rate in the voltage window of 4.2-2.75 V *vs.* Na^+/Na^0 (Figure 6.3). The theoretical capacities of these NASCION compounds are estimated as 55.5, 56 and 57 mA h g^{-1}, respectively (for one mole of sodium ion intercalation per formula unit of cathodes). During the first charge, the NVMP cathode presents two voltage steps (Figure 6.3a) at ~ ca. 3.5/3.45 (V^{4+}/V^{3+}) and 3.6/3.55 V (Mn^{3+}/Mn^{2+}) followed by a monotonously raising voltage curve above 3.8 V (V^{5+}/V^{4+}). The first charge capacity is estimated as ~130 mA h g^{-1}, which is equivalent to the removal of 2.3 moles of sodium ions per formula unit of the cathode. On the subsequent discharge, the voltage profile has changed into a S-shaped curve with a capacity of 90 mA h g^{-1}. Overall, a capacity of ~30 mA h g^{-1} is lost during the first cycle. These observations are in agreement with the earlier reports.[24,25,26] Interestingly, the Mg- and Al-NVMP cathodes also present similar trends in their voltage-capacity profiles and first cycle capacity losses. Their first cycle reversible capacities are estimated as 78 and 89 mA h g^{-1}, respectively. The changes in the charge/discharge voltage profiles of these NASICON cathodes can also be inferred from their corresponding differential capacity plots (Figure 6.3b); three clearly distinguishable oxidation peaks (at 3.4, 3.6 and 3.85 V) are observed during the first charge, whilst the subsequent discharge shows a single reduction feature (at 3.45 V). Upon the subsequent cycles, the capacities of the NVMP, Mg-NVMP and Al-NVMP cathodes are quickly faded and at the end of 50th cycle they reach values of 51, 40 and 57 mA h g^{-1}, respectively (Figure 6.3c).

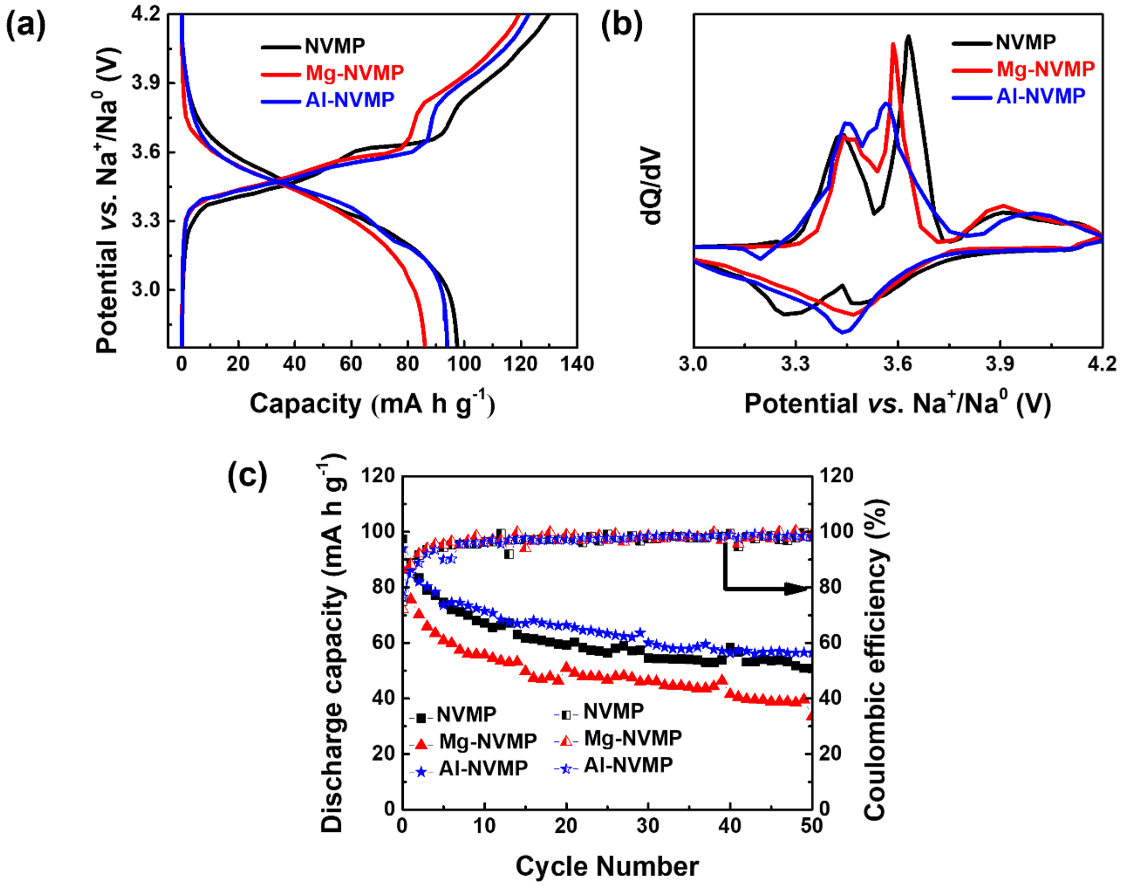

Figure 6.3. (a) Potential *vs*. capacity profiles, (b) differential capacity profiles and (c) cycling performances of the NVMP and Mg- and Al-NVMP cathodes at C/10 in the voltage window of 4.2-2.75 V *vs*. Na$^+$/Na^0.

Further, the cycling voltage window of the NVMP, Mg-NVMP and Al-NVMP cathodes are restricted to 3.8-2.75 V *vs*. Na^+/Na^0 (Figure 6.4). The voltage-capacity profiles of the NVMP cathode present two intercalation steps as mentioned earlier with a reversible capacity of ~ 87 mA h g^{-1} (i.e., equivalent to an exchange of 1.56 moles of sodium ions per formula unit of the cathode) during the first cycle (Figure 6.4a). The corresponding differential capacity plot enlists two sharp peaks at ~ ca. 3.5/3.45 (V^{4+}/V^{3+}) and 3.6/3.55 V (Mn^{3+}/Mn^{2+}), which is due to the occurrence of single-phase and two-phase sodium (de)intercalation reactions, respectively (Figure 6.4b).[22,24] On the other hand, the Mg- and Al-substituted cathodes exhibit smoother voltage-capacity profiles with the reversible capacities of 79 and 89 mA h g^{-1}, respectively. Their average intercalation voltages have also slightly diminished in comparison with the unsubstituted sample, which could be due to the increased covalent character of the NASICON framework. More importantly, the redox features of the Al-NVMP cathode in the derivative plots have become broader and the voltage differences between its charge and discharge processes as well as between the vanadium and manganese redox centers are reduced in comparison with the other two cathodes. Further, to better understand the kinetics of sodium (de)intercalation phenomena into these NASICON cathodes, galvanostatic intermittent titration technique (GITT) measurements were performed (Figure 6.5). When compared to its galvanostatic cycling, the NVMP cathode shows slightly higher amount of sodium exchanges (i.e., 1.9 and 1.8 moles of sodium ions per formula unit during the charge and discharge, respectively) (Figure 6.5a). It reflects the sluggish kinetics of sodium (de)intercalation into the NVMP cathode. In contrast, GITT profiles of the Al-NVMP and Mg-NVMP cathodes show similar reversible capacities compared to their galvanostatic cycling profiles. It is observed that D/R^2 values[32] (which corresponds to the reciprocal time constant associated with sodium ion diffusion, refer Figure 6.5 b-d) for the Mg- and Al-NVMP cathodes are slightly higher ($\sim 10^{-4}$

s^{-1}) than the unsubstituted sample (~10^{-4}-10^{-5} s^{-1}). Besides, the Al-NVMP cathode also exhibits the lowest polarization value between charge and discharge processes in comparison with other samples. Thus, it is clear that the kinetics of sodium (de)intercalation into the Al-NVMP is much better compared to the other cathodes, which could be ascribed to its electronic and local crystal structural changes as well as creation of sodium ion vacancies in the framework, as mentioned earlier.

Figure 6.4c depicts their cycling performances of the NASCION cathodes at 1C rate in the voltage window of 3.8-2.75 V. It is immediately clear that the substitution of inactive Mg^{2+} and Al^{3+} cations in the NVMP framework have remarkably improved its cycling performances. Despite the NVMP and Al-NVMP cathodes exhibit similar initial discharge capacities (92 mA h g^{-1}), the former delivers only 80 % of its initial capacity, whilst the latter maintains 96 % of it at the end of 100th cycle. The substitution of Mg^{2+} in the NVMP also enhances the cycling stability, however, it delivers slightly lower capacities (~78 mA h g^{-1}). It is also worth mentioning that Coulombic efficiencies of ~100 % are maintained for all the cathodes during the long-term cycling process. The rate capabilities of the NVMP, Mg- and Al-NVMP cathodes are evaluated at different C-rates (Figure 6.4d). Although, the NVMP cathode deliver discharge capacities greater than 82 mA h g^{-1} below 1C rates, the capacities are severely diminished at higher discharge rates (~ 60 mA h g^{-1} at 5C rate), in agreement with the earlier report.[27] On other hand, the Mg- and Al-NVMP cathodes deliver discharge capacities higher than 80 mA h g^{-1} even at 5C rate.

Further, to grasp understanding about the influence of inactive cationic substitutions on the sodium (de)intercalation mechanism and structural stability of the NVMP framework, we have performed *in-operando* XRD and *ex-situ* XANES studies on the Al-NVMP cathode (Figure 6.6). The lattice parameters and unit cell volumes obtained from the refinements of selected XRD patterns are displayed in Table 6.2. Upon charging the cell to 3.5 V *vs*. Na^+/Na^0, ~0.9 moles of sodium ions are removed from the Al-NVMP structure. Accordingly, the XRD peaks of the Al-NVMP cathode are progressively shifted towards higher 2θ values, thus indicating the formation of solid-solution. Further, when the cell voltage is increased to 3.8 V *vs*. Na^+/Na^0, another 0.85 moles of sodium is removed from the Al-NVMP structure. During this period, a new set of reflections appears at the expense of the intermediate phase (“$Na_{2.85}VMn_{0.75}Al_{0.25}(PO_4)_3$”) through the two-phase mechanism. At the end of the charge at 3.8 V *vs*. Na^+/Na^0, only the reflections corresponding to the new phase are noticed whose composition is estimated as “$Na_{2.0}VMn_{0.75}Al_{0.25}(PO_4)_3$”. Overall, the removal of 1.75 moles of sodium ions from the Al-NVMP structure decreases the unit cell volume by 8.2 %, which is comparable with values reported for other NASICON cathodes.[22,23,24] On the subsequent discharge to 2.75 V, the abovementioned processes are reversed and the structure of Al-NVMP cathode is fully restored. The normalized XANES of the Al-NMVP cathodes with different state of charges are shown in Figure 6.7b and c. As the cathode is charged to 3.8 V *vs*. Na^+/Na^0, the V and Mn K-edges of the normalized absorption spectra shift towards higher energies and match with that of VO_2 and Mn_2O_3 samples, manifesting the oxidation of V^{3+} to V^{4+} and Mn^{2+} to Mn^{3+}, respectively (Figure 6.6b and c, 6.7a and b). Upon the subsequent discharge to 2.75 V, the Mn K-edge nicely recovers to its original position whereas subtle changes are noticed in the V K-edge.

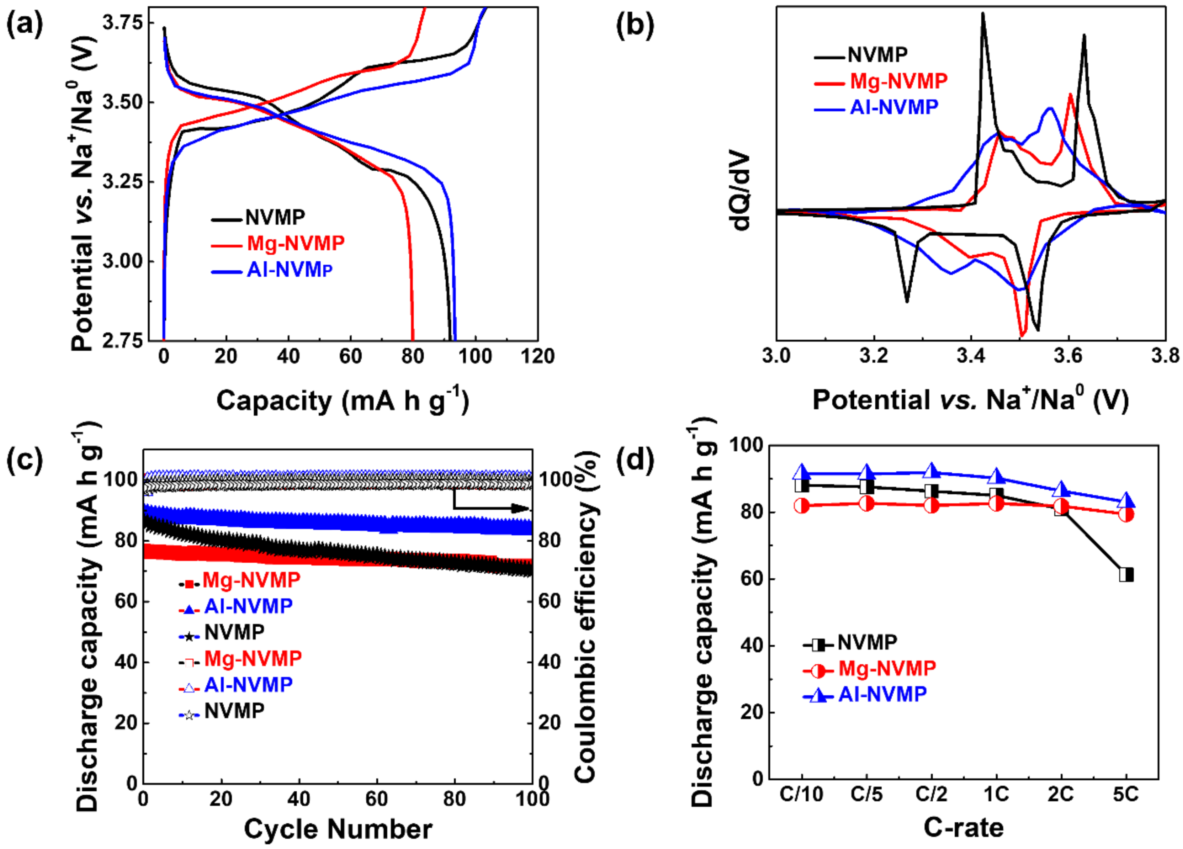

Figure 6.4. (a) Potential *vs*. capacity profiles at C/10 rate, (b) differential capacity plots, (c) cycling performances at 1C rate and (d) rate capabilities of the NVMP, Mg- and Al-NVMP cathodes in the voltage window of 3.8-2.75 V *vs*. Na^+/Na^0.

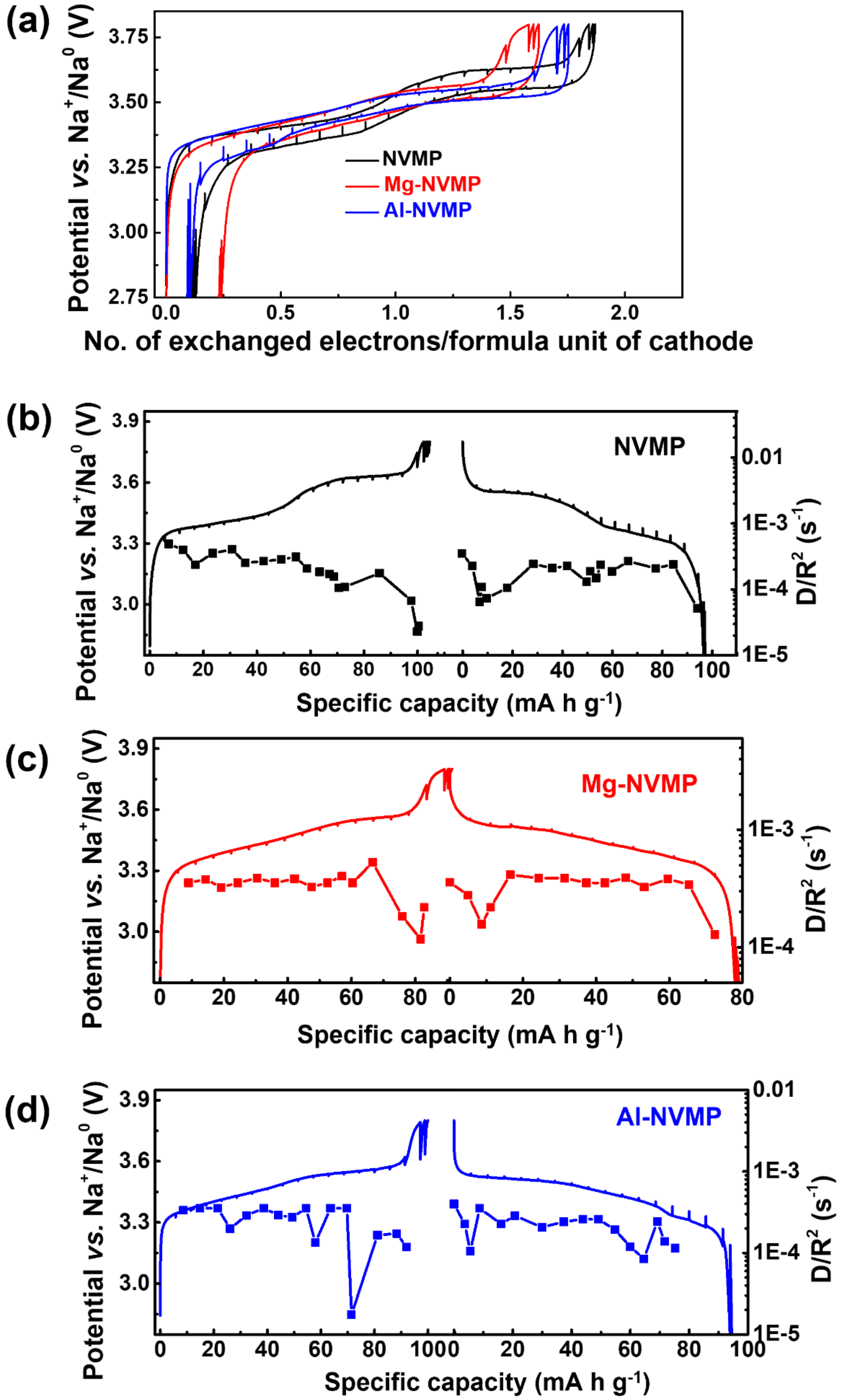

Figure 6.5. GITT profiles and over all trends of D/R^2 values for the NVMP, Mg-NVMP and Al-NVMP cathodes.

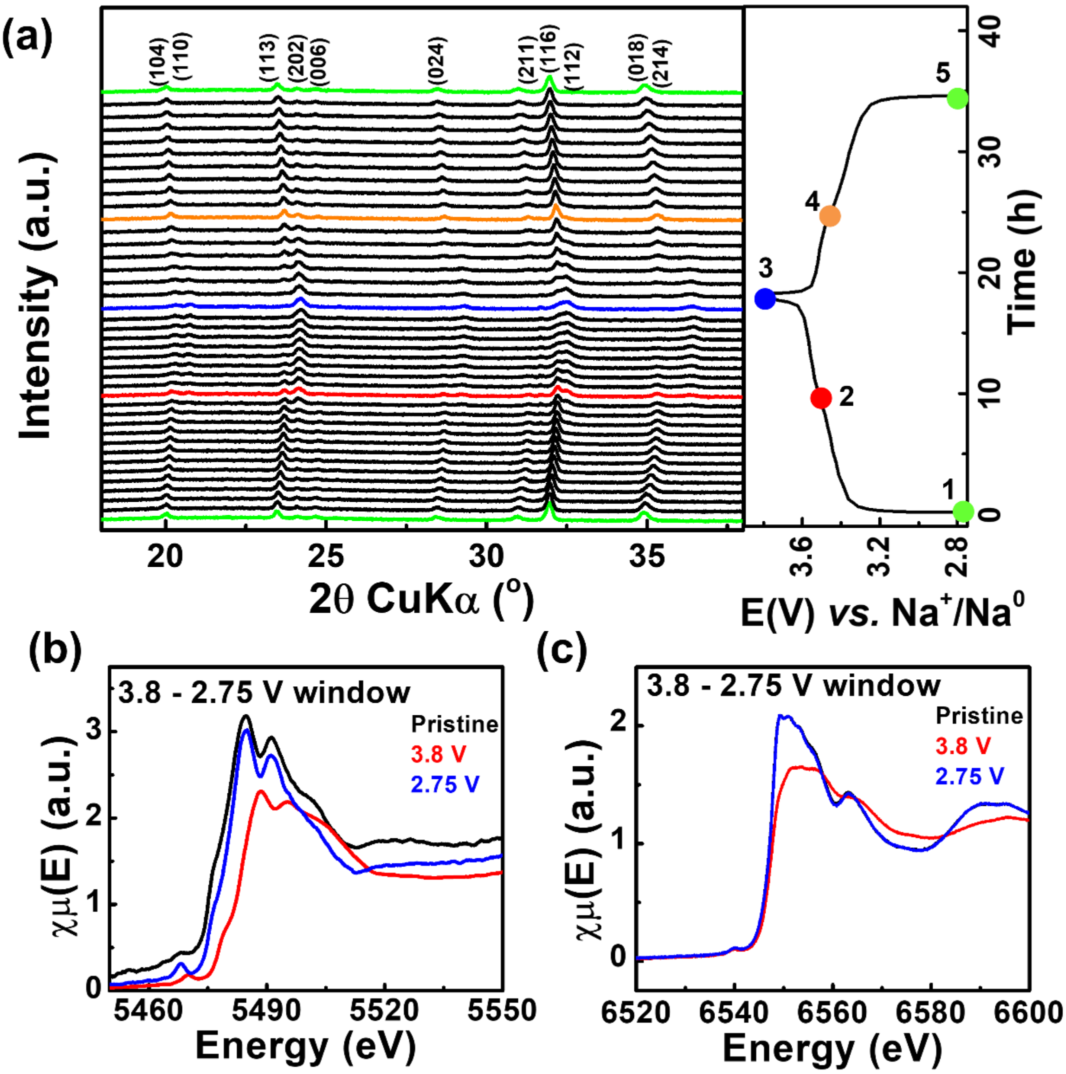

Figure 6.6. (a) *In-operando* XRD patterns and the normalized XAS spectra at (b) V and (c) Mn-K edges of the Al-NVMP cathode cycled in the window of 3.8-2.75 V vs. Na^+/Na^0 at C/10 rate.

Table 6.2: Cell parameters obtained from the refinement of selected *in-operando* XRD patterns of the Al-NVMP cathode.

3.8-2.75 V window			
Pattern No.	***a* (Å)**	***c* (Å)**	**Volume ($Å^3$)**
1	8.8806(8)	21.5648(11)	1472.89(16)
2	8.77389(7)	21.38158(12)	1425.46(9)
3	8.50875(8)	21.53461(4)	1350.20(12)

4	8.77150(9)	21.41435(2)	1426.87(9)
5	8.85486(5)	21.5546(6)	1463.64(7)
4.2-2.75 V window			
6	8.8767(17)	21.564(4)	1471.55(5)
7	8.763(3)	21.467(5)	1427.89(9)
8	8.508(4)	21.4937(1)	1347.42(11)
9	8.465(4)	21.7513(14)	1349.86(13)
10	8.539(5)	21.7783(13)	1375.26(15)
11	8.861(3)	21.534(8)	1464.51(9)

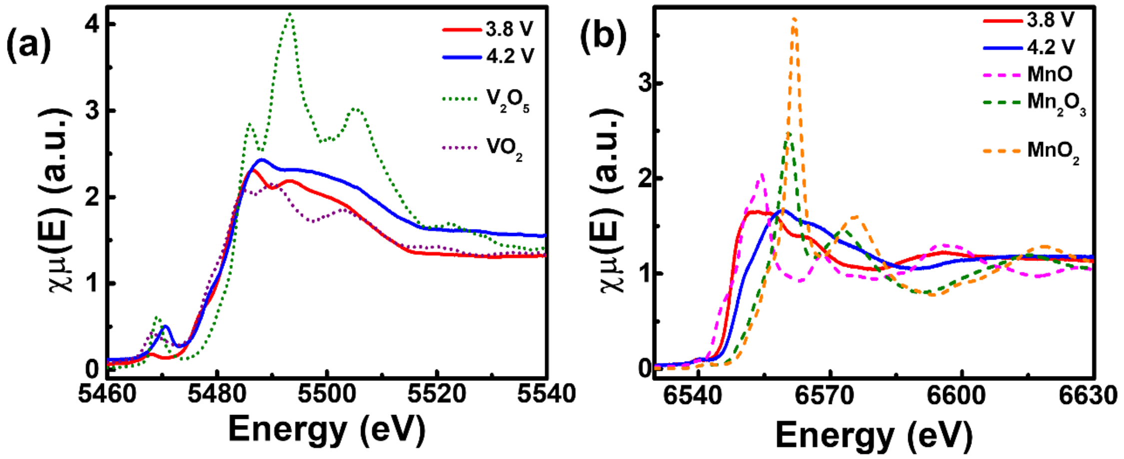

Figure 6.7. Normalized XANES of Al-NVMP cathodes with different state of charges at (a) V and (b) Mn K-edges along with reference samples.

Furthermore, *ex-situ* XRD patterns were collected on the NVMP and Al-NVMP cathodes after 100 cycles to understand their structural stability during long-term cycling. (Figure 6.8). The XRD peaks of the cycled NVMP cathode have become broaden and less intense after 100 cycles. It may be due to the repeated formation of Jahn-Teller distorted Mn^{3+}

during cycling that causes structural degradation. On the other hand, the cycled Mg- and Al-NVMP cathodes present reminiscent XRD peaks compared to that of their pristine electrodes, thus confirming their structural robustness over long-term cycling. These observations have confirmed the benefit of Mg- and Al-substitutions into the NVMP, which has suppressed the Jahn-Teller distortion effect and increased the covalency of the framework.

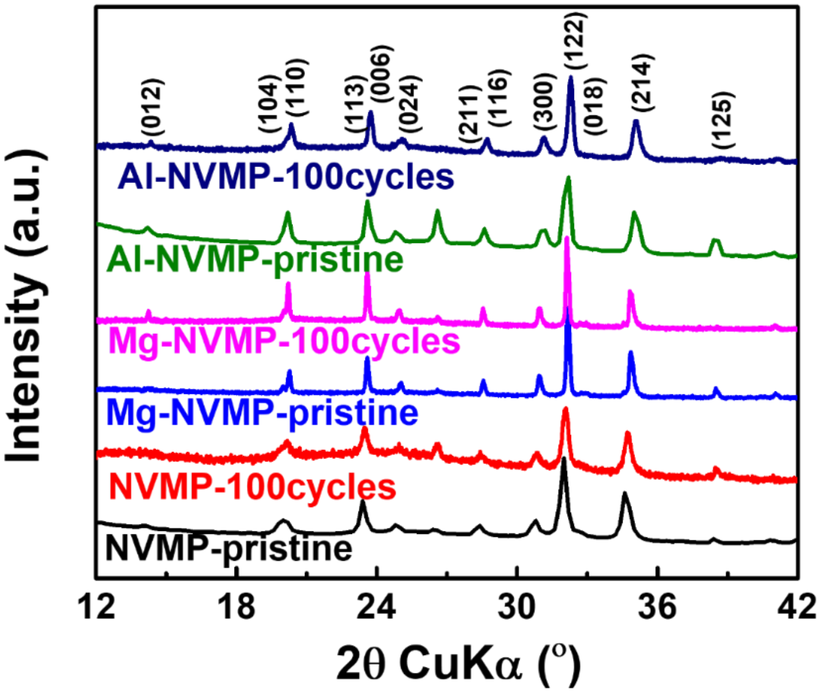

Figure 6.8. *Ex-situ* XRD patterns of pristine and cycled NVMP and Al-NVMP cathodes.

To track down the structural changes that are happening at high voltage, the *in-operando* XRD patterns are collected on the Al-NVMP cathode at 4.2 and 2.75 V *vs*. Na^+/Na^0 (Figure 6.9a). Upon charging to 3.8 V *vs*. Na^+/Na^0, the structural evolution of Al-NVMP cathode is similar to those observed in the previous experiment in the range of 3.8-2.75 V *vs*. Na^+/Na^0. As the charging proceeds to 4.2 V *vs*. Na^+/Na^0, the XRD peaks of the cathode shifts towards higher 2θ values, thus indicating formation of solid solution during (de)intercalation. The XRD pattern collected at 4.2 V *vs*. Na^+/Na^0 reveals anisotropic lattice parameter changes (i.e., increase and decrease of *c* and *a*-parameters, respectively, Table 6.2). The elongation of *c*-parameter could be ascribed to the removal of sodium ions from Na(1) sites which in turn causes strong electrostatic repulsion between adjacent (V/Mn/Al)O_6 octahedra. During the subsequent discharge to 2.75 V, sodium insertion proceeds *via* solid-solution formation followed by a two-phase transformation mechanism. It is worth noting that the $Na_4VMn(PO_4)_3$ cathode have shown a complete solid solution behavior during the entire discharge.[24,25] The change in sodium insertion mechanism upon Al^{3+} substitution in the NVMP cathode could be due to local structural changes and sodium ion/vacancy ordering. The XRD pattern collected at 2.75 V does not superimpose with the XRD pattern of the pristine electrode, which implies the structural changes due to sodium loss during electrochemical cycling. Thus, it is clear that the substitution of Al^{3+} ions in the NVMP framework is unsuccessful to alleviate the structural degradation occurring at high voltages. The vanadium XANES collected on the Al-NVMP cathode charged to 4.2 V present prominent pre-edge with minimal shift in absorption energy (at 5470.7 eV) compared to that of the same cathode charge to 3.8 V (Figure 6.9b). It could be attributed to the partial oxidation of V^{4+} to V^{5+} (Figure 6.7a). More importantly, the Mn-K edge shows shift towards higher energies, thus confirming the participation of Mn^{4+}/Mn^{3+} redox couple during the high voltage charging (Figure 6.9c and 6.7b).[26]

Further, *in-operando* XRD studies were also performed on the Mg-NMVP cathode to follow its structural changes during charge and discharge processes in both voltage windows (3.8-2.75 and 4.2-2.75 V *vs*. Na^+/Na^0) (Figure 6.10 and 6.11). The cell parameters obtained from the refinements of the selected XRD patterns are shown in Table 6.3. The Mg-NMVP cathode undergoes similar structural evolution during the charge and discharge processes as like the Al-NVMP cathodes in both voltage windows.

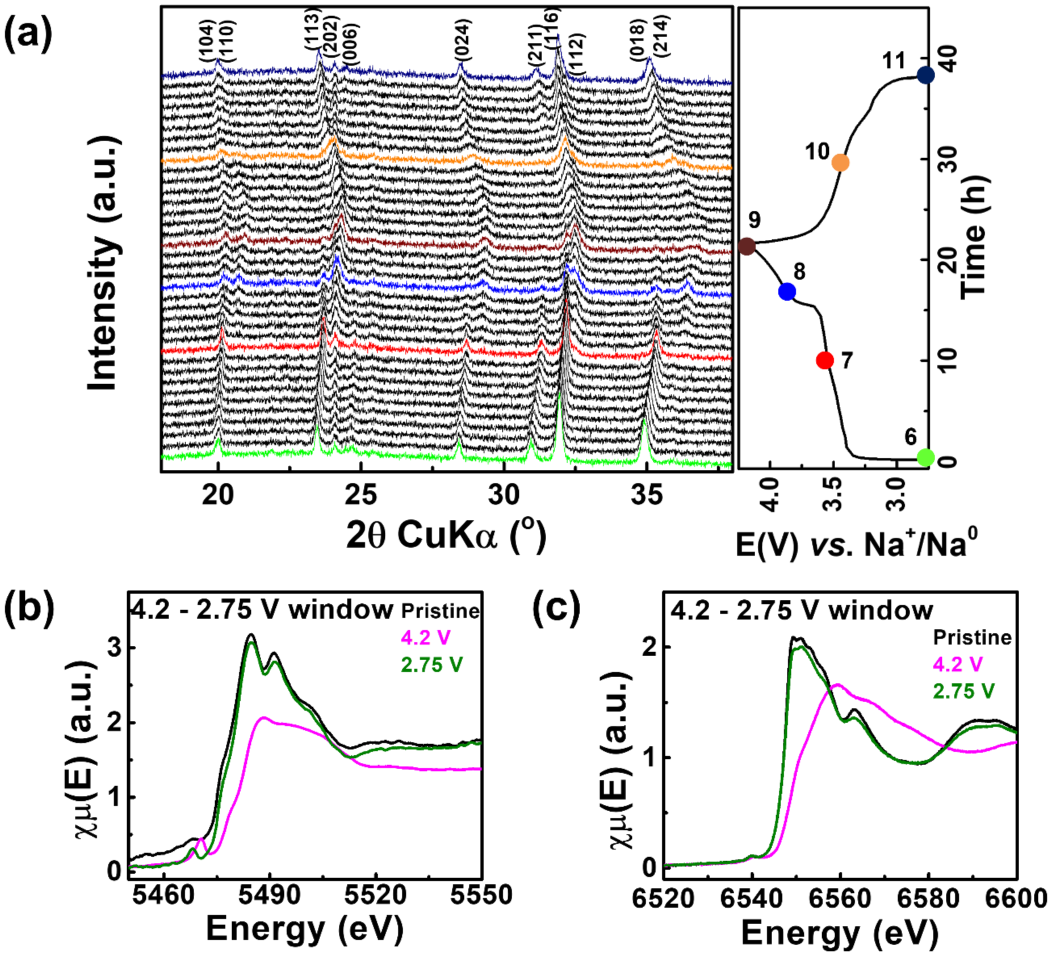

Figure 6.9. (a) *In-operando* XRD patterns and the normalized XAS spectra at (b) V and (c) Mn-K edges of the Al-NVMP cathode cycled in the window of 4.2-2.75 V *vs*. Na^+/Na^0 at C/10 rate.

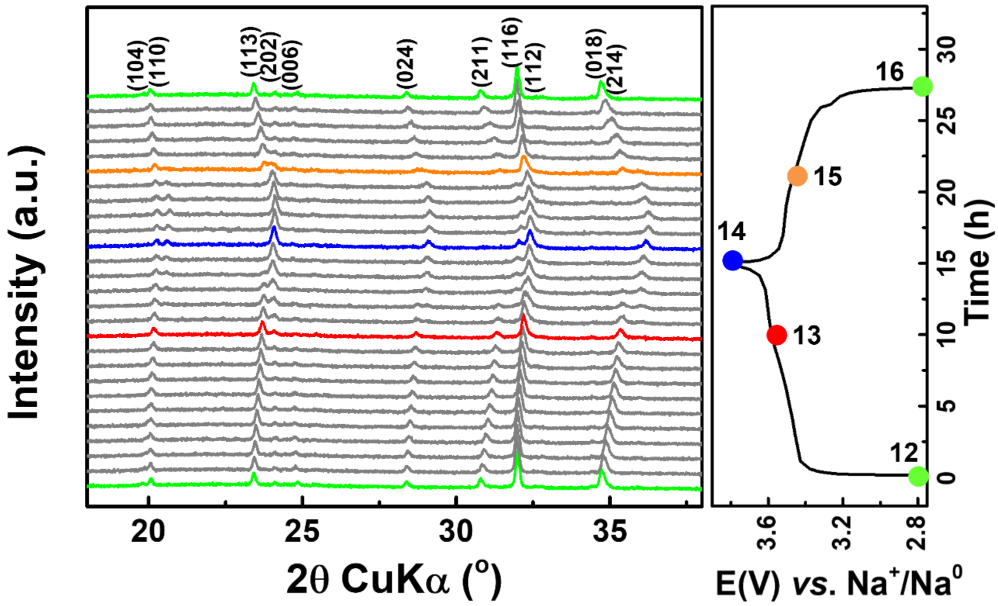

Figure 6.10. *In-operando* XRD patterns of the Mg-NVMP cathode cycled in the window of 3.8- 2.75 V *vs*. Na^+/Na^0 at C/10 rate.

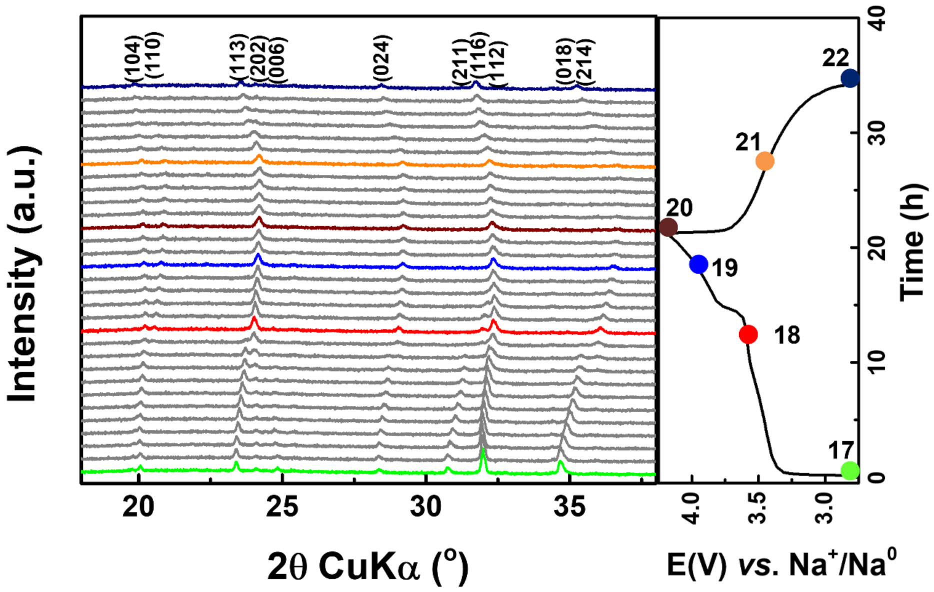

Figure 6.11. *In-operando* XRD patterns of the Mg-NVMP cathode cycled in the window of 4.2-2.75 V *vs*. Na^{+}/Na^{0} at C/10 rate.

Table 6.3: Cell parameters obtained from the refinement of selected *in-operando* XRD patterns of the Mg-NVMP cathode.

3.8-2.75 V window			
Pattern No.	***a*** **(Å)**	***c*** **(Å)**	**Volume (Å^{3})**
12	8.9223(2)	21.4462(5)	1478.54(6)
13	8.7269(9)	21.366(6)	1409.20(4)
14	8.5736(8)	21.5500(11)	1371.84(2)
15	8.7215(8)	21.5999(11)	1422.89(2)
16	8.9193(3)	21.4513(6)	1477.89(9)
4.2-2.75 V window			
17	8.9287(3)	21.4311(6)	1479.62(9)
18	8.8390(3)	21.4728(6)	1452.87(10)
19	8.5150(4)	21.6633(6)	1360.27(11)
20	8.5287(4)	21.766(18)	1371.16(15)
21	8.5614(5)	21.848(13)	1386.92(2)
22	8.9565(7)	21.407(3)	1487.21(8)

6.4. Conclusions

In summary, we have demonstrated a chemical strategy to improve the electrochemical performance of the NVMP cathode through the substitution of inactive Mg^{2+} and Al^{3+} cations. Unfortunately, the Mg- and Al-substitution into the NVMP framework is unsuccessful to prevent the irreversible structural transformation and capacity degradation upon cycling at high voltage window (4.2-2.75 V *vs*. Na^+/Na^0). On other hand, the low voltage window cycling of the Mg- and Al-NVMP cathodes have exhibited higher rate performances (80 mA h g^{-1} at 5C) and better capacity retention (~ 96% after 100 cycles) in comparison with the unsubstituted cathode. Further, i*n-operando* XRD and *ex-situ* XAS studies have confirmed full reversibility of sodium (de)intercalation into the Al-NMVP and Mg-NVMP cathodes. The *ex-situ* XRD measurements have shown high structural integrity of the Mg- and Al-NMVP cathodes during the long-term cycling. The enhanced cycling stabilities of the Mg- and Al-substituted NVMP cathodes are attributed to the suppressed Jahn-Teller distortion and increased covalency of the NASICON framework. The created sodium ion vacancies in the Al-NVMP cathode have improved its sodium intercalation kinetics, which results in slightly higher reversible capacities compared to its Mg-counterpart. Thus, this present study calls for careful tuning of chemical compositions to achieve high performance NASICON cathodes.

References

[1] N.Yabuuchi, K. Kubota, M. Dahbi, S. Komaba, *Chem. Rev.* **2014**, *114*, 11636.

[2] J. Y. Hwang, S. T. Myung, Y. K. Sun, *Chem. Soc. Rev.* **2017**, *46*, 3529.

[3] P. F. Wang, Y. You, Y. X. Yin, Y. G. Guo, *Adv. Energy Mater.* **2017**, *8,* 1701912.

[4] M. H. Han, E. Gonzalo, G. Singha, T. Rojo, *Energy Environ. Sci*. **2015**, *8,* 81.

[5] C. Masquelier, L. Croguennec, *Chem. Rev.* **2013**, *113,* 6552.

[6] S. Y. Lim, H. Kim, R. A. Shakoor, Y. Jung, J. W. Choi, *J. Electrochem. Soc.* **2012**, *159,*

A1393.

[7] X. Zhang, X. Rui, D. Chen, H. Tan, D. Yang, S. Huang, Y. Yu, *Nanoscale*, **2019**, *11*, 2556.

[8] I. V. Zatovsky, *Acta Crystallogr., Sect. A: Found. Crystallogr*. **2010**, *66*, s12..

[9] Z. Jian, C. Yuan, W. Han, X. Lu, L. Gu, X. Xi, Y. S. Hu, H. Li, W. Chen, D. Chen, Y. Ikuhara, L. Chen, *Adv. Funct. Mater.* **2014**, *24*, 4265.

[10] Z. Jian, W. Han, X. Lu, H. Yang, Y. S. Hu, J. Zhou, Z. Zhou, J. Li, W. Chen, D. Chen, L. Chen, *Adv. Energy Mater.* **2013**, *3*, 156.

[11] C. Zhu, K. Song, P. A. Van Aken, J. Maier, Y. Yu, *Nano Lett.* **2014**, *14*, 2175.

[12] L. Zhao, H. Zhao, X. Long, Z. Li, Z. Du, *ACS Appl. Mater. Interfaces*, **2018**, *10*, 35963.

[13] Y. H. Jung, C. H. Lim, D. K. Kim, *J. Mater. Chem. A* **2013**, *1*, 11350.

[14] J. Hwang, K. Matsumoto, R. Hagiwara, *ACS Appl. Energy Mater.* **2019**, *2*, 2818.

[15] M. J. Aragón, P. Lavela, G. F. Ortiz, J. L. Tirado, *ChemElectroChem.* **2015**, *2*, 995.

[16] A. Inoishi, Y. Yoshioka, L. Zhao, A. Kitajou, S. Okada, *ChemElectroChem.* **2017**, *4*, 2755.

[17] W. Shen, H. Li, Z. Guo, Z. Li, Q. Xu, H. Liu, Y. Wang, *RSC Adv.* **2016**, *6*, 71581.

[18] F. Lalère, V. Seznec, M. Courty, R. David, J. N. Chotard, C. Masquelier, *J. Mater. Chem. A* **2015**, *3*, 16198.

[19] H. Li, H. Tang, C. Ma, Y. Bai, J. Alvarado, B. Radhakrishnan, S. P. Ong, F. Wua, Y. S. Meng, C. Wu, *Chem. Mater.* **2018**, *30*, 2498.

[20] X. Liu, G. Feng, E. Wang, H. Chen, Z. Wu, W. Xiang, Y. Zhong, Y. Chen, X. Guo, B. Zhong, *ACS Appl. Mater. Interfaces* **2019**, *11*, 12421.

[21] R. Liu, G. Xu, Q. Li, S. Zheng, G. Zheng, Z. Gong, Y. Li, E. Kruskop, R. Fu, Z. Chen, K. Amine, Y. Yang, *ACS Appl. Mater. Interfaces* **2017**, *9*, 43632.

[22] W. Zhou, L. Xue, X. Lü, H. Gao, Y. Li, S. Xin, G. Fu, Z. Cui, Y. Zhu, J. B. Goodenough, *Nano Lett.* **2016**, *16*, 7836.

[23] J. Zhang, X. Zhao, Y. Song, Q. Li, Y. Liu, J. Chen, X. Xing, *Energy storage materials* **2019**, *23*, 25.

[24] F. Chen, V. M. Kovrugin, R. David, O. Mentré, F. Fauth, J. N. Chotard, C. Masquelier, *Small Methods* **2019**, *3*, 1800218.

[25] M. V. Zakharkin, O. A. Drozhzhin, I. V. Tereshchenko, D. Chernyshov, A. M. Abakumov, E. V. Antipov, K. J. Stevenson, *ACS Appl. Energy Mater.* **2018**, *1*, 5842.

[26] S. Ghosh, N. Barman, M. Mazumder, S. K. Pati, G. Rousse, P. Senguttuvan, *Adv. Energy Mater*. **2019**, 1902918.

[27] H. Li, T. Jin, X. Chen, Y. Lai, Z. Zhang, W. Bao, L. Jiao, *Adv. Energy Mater.* **2018**, *8*, 1801418.

[28] M. Guin, F. Tietz, *J. Power Sources* **2015**, *273*, 1056.

[29] R. D. Shannon, *Acta Crystallogr.* **1976**, *A32*, 751.

[30] J. Wong, F. W. Lytle, R. P. Messmer, D. H. Maylotte, Phys. Rev. B, **1984**, *30*, 5596.

[31] P. Chaurand, P. Rose, V. Briois, M. Salome, O. Proux, V. Nassif, L. Olivi, J. Susini, J. L. Hazemann, J. Y. Bottero, *J. Phys. Chem. B* **2007**, *111*, 5101.

[32] G. Assat, C. Delacourt, D. A. D. Corte, J.-M. Tarascon, J. Electrochem. Soc. **2016**, *163*, A2965.

Summary & Outlook

In the past decade, the battery field has witnessed vast exploration of Na-ion materials, including layered oxide and polyanionic frameworks. Thanks to the intense research efforts on layered oxide materials, they have been successfully applied in commercial Na-ion battery prototypes.[1] However, they still suffer from lower energy density (< 150 Wh kg^{-1}), limited cycle life and air/moisture instability.[2]

The research on Na-ion polyanionic compounds has produced numerous cathode materials with higher intercalation voltages and structural and chemical stabilities. However, their practical application is majorly challenged by their moderate storage capacities (80- 120 mAh g^{-1}) due to electrochemically inactive polyanionic units. $Na_3V_2(PO_4)_2F_3$||hard carbon battery prototypes are successfully demonstrated but with lower energy density (90 Wh kg^{-1}).[3] This thesis has developed a series of high voltage NASICON cathodes, starting from the $Na_3V_2(PO_4)_3$ structure. NASICON cathodes can exchange four moles of sodium ions *pfu* in theory (which is equivalent to capacities of 200-220 mA h g^{-1}), however, only half of it has been realized so far. One plausible pathway to increase their capacities is introducing multi-redox centers, thereby increasing the number of sodium ions exchanged.

Previously, NASICON-$Na_3V_2(PO_4)_3$ cathode was reported for high voltage sodium (de)intercalation (3.45 V *vs*. Na^+/Na^0) and stellar electrochemical performances. In our first attempt, we partially replaced expensive and toxic vanadium with manganese in the NASICON skeleton to produce a series of $Na_{3+y}V_{2-y}Mn_y(PO_4)_3$ cathodes, which also possess $V^{5+}/V^{4+}/V^{3+}$ and $Mn^{4+}/Mn^{3+}/Mn^{2+}$ multi-redox centers. This substitution had produced a series of Na-poor and Na-rich cathodes with phase segregation at $y = 0.5$. The Na/Mn-rich cathodes showed highly reversible redox activities of V^{4+}/V^{3+} and Mn^{3+}/Mn^{2+} in the low voltage window cycling (3.8-2.75 V *vs*. Na^+/Na^0). However, upon activating $V^{5+}/V^{4+}/V^{3+}$ and $Mn^{4+}/Mn^{3+}/Mn^{2+}$ multi-redox centers at higher voltages, severe structural degradation and capacity fade of the cathodes were observed. This process involves a complex interplay between the extraction of sodium ions from Na(1) and Na(2) sites, overlapping V- and Mn-redox operations and their associated local structural changes. Therefore, to better understand it, we have tailored a series of $Na_{3+y}V_{2-y}Mg_y(PO_4)_3$ in which vanadium is the sole redox center. We expected that this strategy could enable us to follow the sodium (de)intercalation phenomena without the interference of manganese redox centers. The Mg-substitution helped tunning the functionalities of NASICON-$Na_{3+y}V_{2-y}Mg_y(PO_4)_3$ cathodes in terms of intercalation voltages, sodium ion diffusion kinetics and (de)intercalation mechanism (two-phase *vs*. solid-solution). However, the high voltage structural degradation due to the removal of sodium ions from Na(1) site and local structural changes was still persistent in these NASICON cathodes.

In the subsequent work, we synthesized NASICON-$Na_3VIn(PO_4)_{3,}$ in which the heavy In^{3+} was expected to stabilize the framework. However, it also suffered from irreversible structural transformation and capacity degradation like the previous NASICON cathodes. Interestingly, when it was cycled in the wider voltage window (4.2-1.2 V *vs*. Na^+/Na^0), the degraded electrode structure rejuvenated at the lower voltages. However, this approach may have a lesser implication on practical application. In the last work chapter, we synthesized NASICON-$Na_{3.75}VMn_{0.75}Al_{0.25}(PO_4)_3$ and -$Na_4VMn_{0.75}Mg_{0.25}(PO_4)_3$ cathodes, which showed improved cycling stabilities and rate performances compared to the unsubstituted $Na_4VMn(PO_4)_3$. Overall, this thesis highlights the importance of tunning the NASICON framework *via* chemical substitutions to achieve high-performance cathodes.

In literature, two major approaches are utilized to improve the electrochemical performances of NASICON cathodes, namely, (i) synthesizing carbon-coated nanomaterials and (ii) tunning chemical composition through doping/substitution. The former approach results in high rate performances and cycling stabilities; however, electrochemically inactive carbon and lower tap densities reduce cathodes' overall energy density. The second approach has produced various NASICON cathodes in recent years, with reversible capacities in the range of 80-150 mA h g^{-1}(Figure 7.1).[4-20] The results of high capacity $Na_4VMn(PO_4)_3$ and $Na_4CrMn(PO_4)_3$ type cathodes are particularly encouraging,[11,16] but their practical applications are still hindered by their limited cycling performances, expensive and toxic vanadium and chromium.

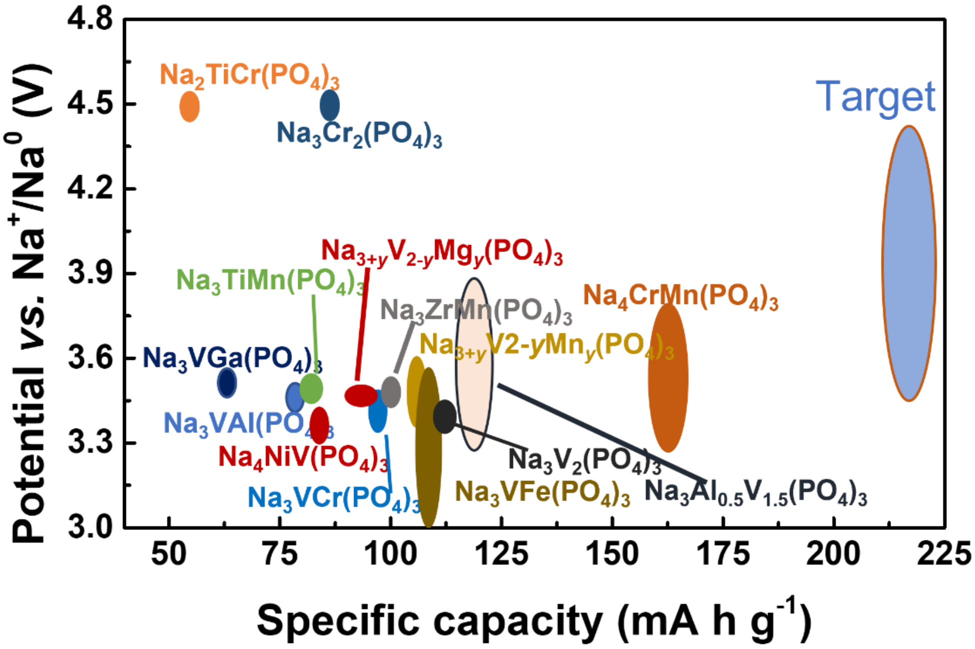

Figure 7.1. Voltage *vs*. capacity plot of NASICON cathodes for Na-ion batteries.[4-20]

Moving forward, the chemical richness of the NASICON framework opens numerous possibilities of cationic substitutions to tailor high voltage and high capacity cathodes. However, their development requires a deeper understanding of the structure-electrochemical sodium (de)intercalation property relationship. For instance, the vanadium-based NASICON cathodes exhibit local structural changes upon high voltage window cycling compared to Mn-based materials even though both render two-electron exchange per transition metal.[20-23] Besides, it is not yet clear how these changes impact bottleneck sizes and Na-ion mobility of the framework. Comprehensive structural and electrochemical studies including local and bulk structural probes as well as theoretical calculations are expected to play vital role on the development of next-generation NASICON cathodes.

References

[1] A. Rudola, A. J. R. Rennie, R. Heap, S. S. Meysami, A. Lowbridge, F. Mazzali, R. Sayers, C. J. Wright, Jerry Barker, ***J. Mater. Chem. A***, **2021**, ***9***, 8279.

[2] P-F. Wang, Y. You, Y-X. Yin, Y-G. Guo, *Adv. Energy Mater*. **2018**, *8*, 1701912.

[3] N. Tapia-Ruiz, A R. Armstrong, H. Alptekin, M. A Amores, H. Au, J. Barker, R. Boston, W. R Brant, J. M Brittain, Y. Chen, M. Chhowalla, Y-S. Choi, S. I R Costa, M. C. Ribadeneyra, S. A Cussen, E. J Cussen, W. I F David, A. V Desai, S. A M Dickson, E. I Eweka, J. D Forero-Saboya, C. P Grey, J. M Griffin, P. Gross, X. Hua, J. T S Irvine, P. Johansson, M. O Jones, M. Karlsmo, E. Kendrick, E. Kim, O. V Kolosov, Z. Li, S. F L Mertens, R. Mogensen, L. Monconduit, R. E Morris, A. J Naylor, S. Nikman, C. A O’Keefe, D. M C Ould, R G P. P. Poizot, A. Ponrouch, S. Renault, E. M Reynolds, A. Rudola, R. Sayers, D. O Scanlon, S. Sen, V. R Seymour, B. Silv´an, M. T. Sougrati, L. Stievano, G. S Stone, C. I Thomas, M-M. Titirici, J. Tong, T. J Wood, D. S Wright, R. Younesi, *J. Phys. Energy*, **2021**, *3*, 031503.

[4] J. B. Goodenough, H. Y-P. Hong, J. A. Kafala, *Mat. Res. Bull*. **1976**, *11*, 203.

[5] K. Saravanan, C. W. Mason, A. Rudola, K. H. Wong, P. Balaya, *Adv. Energy Mater*. **2013**, *3*, 444.

[6] J. Kang, S. Baek, V. Mathew, J. Gim, J. Song, H. Park, E. Chae, A. K. Rai, J Kim, *J. Mater. Chem*. **2012**, *22*, 20852.

[7] K. Kawai, W. Zhao, S-i Nishimura, A. Yamada, *ACS Appl. Energy Mat*. **2018**, *1*, 928.

[8] H. Gao, Y. Li, K. Park, J. B. Goodenough, *Chem. Mater*. **2016**, *28*, 6553.

[9] H. Gao, I. D. Seymour, S. Xin, L. Xue, G. Henkelman, J. B. Goodenough, *J. Am. Chem. Soc*. **2018**, *140*, 18192.

[10] W. Zhou, L. Xue, X. Lü, H. Gao, Y. Li, S. Xin, G. Fu, Z. Cui, Y. Zhu, J. B. Goodenough, *Nano lett*. **2016**, *16*, 7836.

[11] F. Chen, V. M. Kovrugin, R. David, O. Mentré, F. Fauth, J. N. Chotard, C. Masquelier, *Small Methods*, **2019**, *3*, 1800218.

[12] M. V. Zakharkin, O. A. Drozhzhin, I. V. Tereshchenko, D. Chernyshov, A. M. Abakumov, E. V. Antipov, K. J. Stevenson, *ACS Appl. Energy Mater*. **2018**, *1*, 5842.

[13] F. Lalere, V. Seznec, M. Courty, R. David, J. N. Chotard, C. Masquilier, *J. Mater. Chem. A*, **2015**, *3*, 16198.

[14] H. Li, H. Tang, C. Ma, Y. Bai, J. Alvarado, B. Radhakrishnan, S. P. Ong, F. Wua, Y. S. Meng, C. Wu, *Chem. Mater*. **2018**, *30*, 2498.

[15] J. Wang, Y. Wang, D-H. Seo, T. Shi, S. Chen, Y. Tian, H. Kim, G. Ceder, *Adv. Energy Mater*. **2020**, *10*, 1903968.

[16] J. Zhang, Y. Liu, X. Zhao, L. He, H. Liu, Y. Song, S. Sun, Q. Li, X. Xing, J. Chen, *Adv. Mater*. **2020**, *32*, 1906348.

[17] J. Zhang, G. Liang, C. Wang, C. Lin, J. Chen, Z. Zhang, X. S. Zhao, *ACS Appl. Mat. Interface*, **2020**, *12*, 28313.

[18] R. Liu, G. Xu, Q. Li, S. Zheng, G. Zheng, Z. Gong, Y. Li, E. Kruskop, R. Fu, Z. Chen, K. Amine, Y. Yong, *ACS Appl. Mater. Interface*, **2017**, *9*, 43632.

[19] Q. Wang, H. Gao, J. Li, G-B. Liu, H. Jin, *ACS Appl. Mater. Interface*, **2021**, *13*, 14312.

[20] S. Ghosh, N. Barman, M. Mazumder, S. K. Pati, G. Rousse, P. Senguttuvan, *Adv. Energy Mater*. **2020**, *10*, 1902918.

[21] S. Ghosh, N. Barman, E. Gonzalez-Correa, M. Mazumder, A. Zaveri, R. Giovine, A. Manche, S. K. Pati, R. J. Clément, P. Senguttuvan, *Adv. Funct. Mater*. **2021**, 2105463.

[22] H. Gao, Y. Li, K. Park, J. B. Goodenough, *Chem. Mater*. **2016**, *28*, 6553.

[23] H. Gao, I. D. Seymour, S. Xin, L. Xue, G. Henkelman, J. B. Goodenough, *J. Am. Chem. Soc*. **2018**, *140*, 18192.

List of Publications

Included in thesis

[1] S. Ghosh, N. Barman, M. Mazumder, S. K. Pati, G. Rousse, P. Senguttuvan, High Capacity and High-Rate NASICON-$Na_{3.75}V_{1.25}Mn_{0.75}(PO_4)_3$ Cathode for Na-Ion Batteries via Modulating Electronic and Crystal Structures**,** *Adv. Energy Mater.* **2020**, *10*, 1902918.

[2] S. Ghosh, N. Barman, P. Senguttuvan, Impact of Mg^{2+} and Al^{3+} Substitutions on the Structural and Electrochemical Properties of NASICON-$Na_xVMn_{0.75}M_{0.25}(PO_4)_3$ (M = Mg and Al) Cathodes, *Small*, **2020**, *16*, 2003973.

[3] S. Ghosh, N. Jose, B. Senthilkumar, P. Amonpattaratkit, P. Senguttuvan, Multi-Redox ($V^{5+}/V^{4+}/V^{3+}/V^{2+}$) Driven Asymmetric Sodium (De)intercalation Reactions in NASICON-$Na_3VIn(PO_4)_3$ Cathode, *J. Electrochem. Soc.* **2021**, *168*, 050534.

[4] S. Ghosh, N. Barman, E. Gonzalez-Correa, M. Mazumder, A. Zaveri, R. Giovine, A. Manche, S. K. Pati, R. J. Clément, P. Senguttuvan, Elucidating the Impact of Mg Substitution on the Properties of NASICON-$Na_{3+y}V_{2-y}Mg_y(PO_4)_3$ Cathodes, *Adv. Funct. Mater.* **2021**, 2105463.

Not included in thesis

[1] U. K. Dey, N. Barman, S. Ghosh, S. Sarkar, S. C. Peter, P. Senguttuvan, Topochemical Bottom-Up Synthesis of 2D-and 3D-Sodium Iron Fluoride Frameworks, *Chem. Mater.* **2019**, *31*, 295.

Biography

Subham Ghosh received his B.Sc. degree (2013) in chemistry from University of Burdwan, India and M.Sc. degree (2015) in Chemical Sciences from Indian Institute of Technology Bombay, India. He was persuing his Ph.D. degree in New Chemistry Unit, JNCASR under the supervision of Dr. Premkumar Senguttuvan. His objective of work was to develop polyanionic cathode materials for Na-ion batteries.